UNIVERSITY OF OKLAHOMA

GRADUATE COLLEGE

PHYSICAL KNOWLEDGE BASED SCALABLE PHASED ARRAY ANTENNA MODELING FOR RADAR SYSTEMS

A DISSERTATION

SUBMITTED TO THE GRADUATE FACULTY

in partial fulfillment of the requirements for the

Degree of

DOCTOR OF PHILOSOPHY

By

SUDANTHA JAYALAL PERERA

Norman, Oklahoma

2016

PHYSICAL KNOWLEDGE BASED SCALABLE PHASED ARRAY ANTENNA MODELING FOR RADAR SYSTEMS

A DISSERTATION APPROVED FOR THE
SCHOOL OF ELECTRICAL AND COMPUTER ENGINEERING

BY

Dr. Yan Zhang, Chair

Dr. Kimball Martin

Dr. Patrick McCann

Dr. Hjalti Sigmarsson

Dr. Richard Doviak

To my family...

Acknowledgements

First, I would like to express my sincere gratitude to my advisor Professor Yan Zhang (Rockee) for the continuous support of my Ph.D. study and related research, for his patience, motivation, and knowledge. His precious advice and opinions in this research helped me to gain experience in computational electromagnetics, phased array antennas, and microwave engineering.

I am particularly thankful to the members of my Ph.D. committee, Professor Kimball Martin, Professor Patrick McCann, Professor Hjalti Sigmarsson, Professor Richard Doviak for their insightful and helpful suggestions. I am also thankful to the two former members of this committee Professor Dusan Zrnic and Dr. Shaya Karimkashi for being on my Ph.D. committee. Moreover, Professor Richard Doviak and Professor Dusan Zrnic were willing to be coauthors of all of my publications and spend their valuble time to review them. Besides their insightful comments and commitment to be great coauthors, a great honor for me to being able to have their names as coauthors on my papers. I thank Professor Salazar for giving me valuble instructions for antenna measurement in Near-Field and Far-Field facility. NOAA-NSSL have been granting funds for this research in last few years. I am indeed grateful for making this research possible by giving all the grants we needed.

I started pursuing my PH.D. in Spring 2011 and I have been in radar innovations laboratory since Summer 2011. During this time, members of the ECE faculty, the staff of ECE, the engineers and staff members at RIL, and my friends at RIL supported me in various ways for my study and research. I am thankful to you each and every one of you and it's a great pleasure to meet with you.

Last, but not least, I would like to thank my family. I am sincerely grateful to my beloved wife (Lochani Perera) for her understanding and love during the past three years. I thank my little son (Jethro Perera) for showing his beautiful smile every day. I would like to extend my gratitude and love to my father (Joseph Perera) and mother (Annie Perera) for their selfless and unconditional support and love. I know that I am forever in your debt. I am so grateful to my brother (Jude Perea) and my sister (Kanthi Perera) for their countless support. I acknowlage my wife's parents (Nicholas Perera and Suba Perera) and brother (Thesara Perera) for their great love.

Table of Contents

List of Figures

List of Tables

Abstract

The development of a large-scale phased array radar system such as the future MPAR will need a cost-effective tool for predicting electromagnetic characteristics of antennas. Simulating and optimizing of large finite phased array antennas using commercially available solvers are time-consuming and memory-extensive even though they are highly capable of solving general electromagnetic problems with acceptable accuracy. In this work, a full-wave electromagnetic solver based on finite-difference time-domain (FDTD) method has been developed for simulating phased array antennas. The planar array or array element can be simulated, optimized, or analyzed using FDTD theory based on an orthogonal, regular Cartesian lattice. The FDTD updating equation for diagonally anisotropic material was obtained for periodic structure based on the cylindrical coordinate system. This FDTD algorithm can be used to simulate active element patterns of conformally cylindrical array antennas. The simulation of active element patterns in an infinite faceted-cylindrical array was accomplished with a nonorthogonal and unstructured grid. The derivation of FDTD theory and periodic boundary condition for a structure based on the nonorthogonal and unstructured grid is presented. In this work, two simulation schemes, which are based on computed near-field current density information and the physical knowledge of finite array antennas, were presented for predicting broadside array radiation characteristics with the consumption of relatively low computational resources. The validation of the simulation program and schemes was fulfilled by comparing simulation results with measurements taken by near-field and far-field techniques.

Chapter 1

Introduction

The phased array antenna is an arrangement of multiple microwave radiators employed to form a directive beam by using the wave behavior of constructive and destructive interference. Besides the capability of forming the directive beam in the desired direction, the phased array antenna enables many features in radar and communication systems.

1.1 Phased Array Antennas and Applications in Radar and Communication Systems

1.1.1 History

In 1905, Karl Ferdinand Braun, a Nobel laureate in physics, experimentally demonstrated that three antennas located at the corners of an equilateral triangle with quarter wavelength altitude could form a directional transmitter, which could steer the direction of the beam by 120°. According to his lecture [1], one antenna, he labeled as (C), has a quarter wavelength phased delay with respect to the other two (A) and (B), which are in phased. By shifting the excitation circularly, (A) → (B) → (C) → (A), he could steer the direction of the beam by 120°. Even though his experiment does not fully demonstrate the basic concept of the phased array

antenna, this is the first agile-beam demonstration, and this experiment reflects our interest in agile-beam forming going back to the beginning of the twentieth century.

After Marconi had published a paper about directional antennas[2] in the proceedings for the Royal Society of London in 1925, a few researchers started investigating how to design antennas with a directional beam. Friis [3] built the first array of loop antennas to create a directional beam in 1925. In the 1920s, 1930s, and 1940s, some early researchers such as Friis, Feldman [3–5], Hansen [6, 7], Bruce [8], Carter [9], Schelkunoff [10], and Southworth [11] did pioneering theoretical and experimental research on phased array antennas. During World War II, early phased array antennas were built for radar systems by the United States and Britain. Dolph[12] and Taylor [13] made important contribution to array pattern synthesis. Until 1950, beam forming systems of Phased Array Antennas were implemented with an electromechanical system to produce the phase sheeting for each element. The invention of the first ferrite phase shifter [14] in 1954 was a milestone in the development of phased array antenna technology. In the early 1960s, a handful of research institutes and companies such as Lincoln Laboratories [15], General Electric (GE), Radio Corporation of America (RCA), and Hughes started conducting dedicated research on phased arrays. During this decade (the 1960s), the technology for diode phase shifters [16–19] started evolving, and that became an excellent alternative to ferrite phase shifters. The digital beam forming [20, 21] was first used in underwater acoustic array for detection systems in the 1950s. Because of the higher flexibility of digital progressing techniques, digital beam forming [22–25] became a very promising branch of phased array technology. In 1991, Ng et al [26] demonstrated the first optical delay system, which could be used in the beam forming of phased array systems. Due to the inefficiencies in modulation, detection, and switching, this area is still under investigation. In addition to the array synthesis method introduced by Dolph and Taylor, many other algorithms were developed in the 1990s. The conjugate gradient-based algorithm

[27], simulated annealing (SA) [28], genetic algorithm (GA) [29], and intersection approach [30] are the significant discoveries among the pattern shaping algorithms that emerged in the 1990's. The particle swarm optimization (PSO) [31] was introduced to minimize sidelobe level in 2005. The GaAs integrated microwave circuits or monolithic microwave integrated circuits (MMIC) made low-cost TR modules a reality [32]. The GaN and SiC technologies made TR module on chip more power handling capable [33].

In this subsection, a very brief history of phased array is presented. More details about the history of this fascinating field can be found in chapter 17 of *History of Wireless* [34] written by Robert Mailloux.

1.1.2 Applications

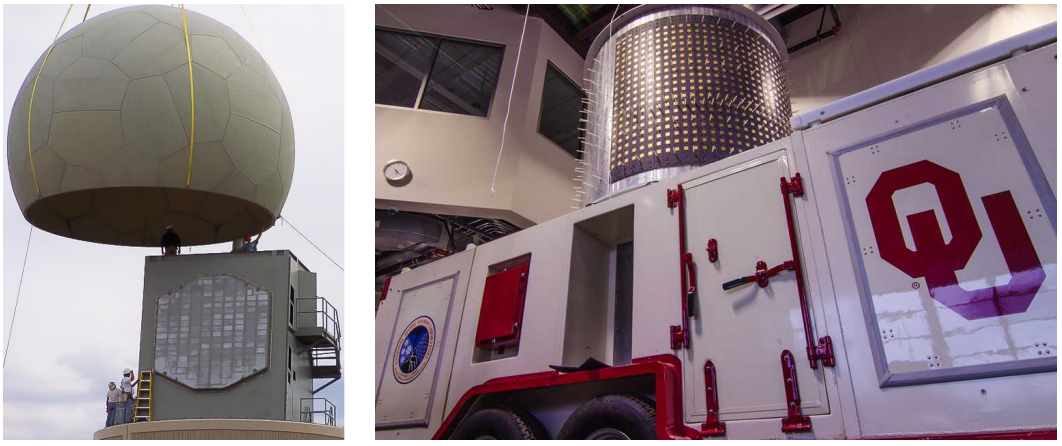

(a) NOAA's National Weather Radar Testbed (NWRT).

(b) Cylindrical Polarimetric Phased Array Radar (CPPAR).

FIGURE 1.1: Example of Phased Array Radar Systems for Weather Measurements

Although phased array technology has been used in many commercial applications, the military applications have been the most significant since its discovery. Sea-Based X-Band (SBX) is the most impressive phased array radar system in the world. It is a massive X-band phased array radar system floating on the sea. This phased array system is a mobile ballistic missile defense system. The whole system

is 85 meters tall and 116 meters long. The phased array antenna has 352 subarrays, which have 128 TR modules [35]. AN/SPY-1 is a passive S-band phased array radar system manufactured by Lockheed Martin. SPY-1A is the system used for NOAA's National Weather Radar Testbed (NWRT) located in Norman Oklahoma (Figure 1.1(a)). The beam width of the broadside pattern is 1.7° by 1.7°. The AN/SPY-3 manufactured by Raytheon is an X-band active phased array radar system used by the Blue-water Navy. Theater High Altitude Area Defense (THAAD), an anti-ballistic missile system, uses an X-band phased-array radar system. The phased arrays are used in MIM-104 Patriot, which is a surface-to-air missile system. The highly agile beam created by phased array antenna in MIM-104 Patriot is capable of detecting a fast target with low radar cross-sectional areas (ballistic missiles, stealth aircraft, and cruise missiles). B-1B aircraft is equipped with navigation and weapon-targeting radar (the AN/APQ-164 radar) system in which a phased array antenna is used. The MP-RTIP manufactured by Northrop Grumman is an X-Band long range active phased array radar system with the capabilities of very high-resolution synthetic aperture radar, ground moving target indicator, and air target tracking. These are a few examples of military applications of phased array antennas. The complete list of military applications is much longer.

While today's vehicles are equipped with many safety precautions, the lack of attention and errors of drivers cause over a million fatalities per year. The low-cost phase array antennas are designed for intelligent collision avoidance and cruise control radar of the automobile [36]. A W-band phased array radar system is built on a single SiGe chip with digital or RF beamforming capabilities. Even though phased array on a chip is under investigation for more improvements and capabilities [37–39], those systems are in production by many manufacturers (Denso, Bosch, and Delphi).

A highly agile beam is a critical aspect of today's weather radar system, because it can bring many required improvements such as high Probability of Detection

(POD), low False Alarm Ratio (FAR), implementing of numerical weather models, and flexibility. Traditional parabolic antennas with mechanical beam steering such as Weather Surveillance Radar-1988 Doppler (WSR-88D) cannot gain the high flexibility and superior observation capability that phased array can [40]. Cylindrical Polarimetric Phased Array Radar (CPPAR) [41–43] was developed to demonstrate the inherent polarimetric advantage [44] of the cylindrical manifold in weather radar applications (Figure 1.1(b)). This is an S-band array with 1824 elements. The elevation beam steering is done by frequency scanning, and the elevation range is from 0° to 20° corresponding to the frequency from 2.7GHz to 3.1GHz. The 3dB-beam width of the broadside pattern is 4.5° in the vertical plane.

In the United States, seven radar system networks are in operation for the defense and surveillance services. The next generation solution is the Multi-function Phased Array Radar (MPAR) network, which can perform severe weather surveillance, long range surveillance, locate non-cooperate targets, terminal area surveillance, chemical dispersion, and many other surveillances simultaneously. The number of MPAR systems in this new network can be approximately 350 [45, 46]. Besides the many applications of phased array antennas in radar systems used in military and commercial products, the applications in the communication systems keep expanding every day. The satellite and deep-space communications are using circularly polarized array antennas. There are many radio broadcasting cooperations which use phased array antennas to avoid interference with other signals. 5G LTE systems are about to appear by 2022. The proposed system is operating in mmWave bandwidths and phased array on a chip technology is essential for proposed millimeter-wave 5G communication systems [47].

The Multiple Input and Multiple Output (MIMO) radar [48, 49] can provide better resolution and accuracy than conventional phased array radar systems. Since the system does not have the maximum energy efficiency and is required to have high signal processing requirements, these radar systems are well suited for searching

rather than tracking.

1.1.3 Ongoing Research in Phased Array Antennas

According to the IEEE International Symposium on Phased Array Systems and Technology in 2014 and 2016, there are many mainstream research areas in phased array antennas. Array designing methodologies, T/R modules, array beamforming, calibration, array signal processing, array measurements, conformal array, and applications (radar and communication) can be listed as those main areas of research. There are large and more specific research areas which can be categorized under one or many of the mainstream areas. As an example, multi-functional phased array radar may be classified under almost all of the mainstream areas since the system will be more versatile.

1.2 Various Types of Phased Array Antennas and Manifolds

In the world of phased array antennas, there are many manifolds in use such as Linear Array Antennas, Planar Array Antennas, and various kinds of Conformal Array Antennas. Linear arrays are the simplest and oldest array manifolds. The linear array can be considered as a special kind of planar array. The planar array is the most commonly used array manifold which has array elements populated on a planar surface in the regular or irregular arrangement. The conformal array antennas have various types since the array is supposed to conform to a prescribed shape. One can categorize conformal arrays into two groups: singly curved surface and doubly curved surface. The most typical example for array antenna with a singly curved surface is circular cylindrical array antennas. This is the most desired array manifold for weather radar applications, because of the polarimetric advantage. Rings, elliptic cylinders, hyperbolic cylinders, and cones are the other

singly curved surfaces. There are many antennas on the skin of a passenger or military aircraft. They need to be directional beam forming antennas. Doubly curved arrays are apparently qualified as the solution for many of them, because doubly curved arrays can have the surfaces of simple geometrical shapes such as spheres, paraboloid, hyperbolic paraboloid, ellipsoid, and hyperboloid or arbitrary shapes. The faceted arrays for any conformal array with singly curved surface and doubly curved surface can exist. In this work, planar arrays, circular cylindrical arrays, and faceted cylindrical arrays are considered exclusively.

1.3 Importance of Antenna Modeling for MPAR

Developing a low-cost Multifunction Phased Array Radar (MPAR) is very challenging as the system is expected to be versatile and operate up to the desired level of performance in different functionalities. As an example, the single linear polarizations are used to do the aircraft surveillance in normal weather conditions. However, under heavy precipitation, a circularly polarized mode is needed to minimize the depolarization loss [50]. System capabilities of current radar networks, which are used for terminal aircraft surveillance, en route aircraft surveillance, terminal area weather surveillance, and national scale weather surveillance have different sensitivity, coverage, angular resolution, waveform, and update rate [51]. According to the cost model presented in [46], an antenna element, T/R module, power, timing, and control, digital transceiver, analog beamformer, digital beamformer, mechanical/packaging, and RF interconnects are the main parts which should be included in the MPAR system. To realize the conceptual MPAR system, the research and development (R&D) needs to be done in four main streams. By bringing improvements to elements of finite array antennas and developing phased array architectures are essential to risk mitigation in the MPAR full-scale system. The cost effective, more flexible, and compact TR module design is a main research interest [52]. The back-end development of radar systems with

field programmable gate arrays (FPGAs) and application-specific integrated circuits (ASICs) are an ongoing developments by numerous researchers. The forth research area of MPAR is post processing of the digital data from the back-end system.

Advanced Technology Demonstrator (ATD), a planar array with advanced dual-polarization capabilities is proposed to demonstrate the risk mitigation of the MPAR concept. NOAA National Severe Storms Laboratory (NSSL) and Federal Aviation Administration (FAA) are jointly participating in this project to replace SPY-1A passive array installed on NWRT with ATD. It has been theoretically shown that cylindrical array [44] manifold has unique advantage in weather measurements. Therefore the correct modeling of phased array antennas is a critical aspect in future MPAR systems.

1.4 The Approach Used in the Work

The designing and optimization of the array antenna are mostly done by the proper quantitative antenna analysis. Since large finite phased array antenna elements can not be easily designed or optimized by simple analytical or intuitive methods, the simulation tools developed based on a numerical method are used to approximate the solution of analytical equations. The phased array antennas (more princely any antenna) will be mainly characterized by the radiation pattern (gain, directivity, E-field, or axial ratio) and input impedance (or S parameters). In addition to these two measurements, mutual coupling matrix or scattering matrix which can be derived from input impedance or radiation pattern of embedded elements will be important in phased array antennas characterization.

In this work, both measurement and simulation are used to validate the proposed methods. Far-field and near-field techniques were utilized in the measurement procedures of antennas presented in this dissertation. The finite array simulation methods are the ultimate objective of this work which is using the Finite

Difference Time Domain (FDTD) method. Periodic Boundary Conditions (PBC) and Convolutional Perfectly Match Layer (CPML) are used whenever required to model the finite array problem.

1.5 Dissertation Outline and Objectives

The objective of this work has the following three aspects: (1) the comparison of various array antennas with both measurements and simulations, (2) development of the FDTD program with PBC in rectangular, cylindrical, and non-structured nonorthogonal grid for simulations of active element in planar, cylindrical and faceted-cylindrical arrays, and (3) scalable electromagnetic characterization of large finite array antenna using two new schemes to do the FDTD simulation. All three aspects focus on the pursuit of one objective. That is to develop an innovative procedure which is based on both physics and theoretical knowledge to analyze large finite phased arrays for weather radar applications.

Chapter 2 start with a general discussion of computational electromagnetic (CEM) in section 2.1. A overview of the Finite Difference Methods (Section 2.1.1), Finite Element Method (Section 2.1.2), Method of Moments (Section 2.1.3), High Frequency Asymptotic Methods (Section 2.1.4), and Hybrid Methods (Section 2.1.5) are presented. The discussion of the Finite Difference Time Domain (FDTD) method is more emphasized since FDTD is the method being used in this work. Section 2.2 evaluates the strengths and weaknesses of each computational electromagnetic technique. The last section of Chapter 2 (Section 2.3) introduces the EM Solver called *PASim* (**P**hased **A**rray **Sim**ulator) build as a part of this work. Section 2.3 presents the motivation to build it, the spacial capabilities of *PASim* in finite phased array antenna simulation.

Chapter 3 presents detailed theory of *PASim* program and simulation results using *PASim*, HFSS, and xFDTD. Section 3.1 discusses the *PASim* implementation (updating equations in [53], numerical dispersion in Section 3.1.1, perfectly match

layer in [53], and periodic boundary condition in Section 3.1.2) in rectangular grid. The *PASim* is capable of modeling the cylindrical phased array antenna. The derivation of updating equations, numerical stablity, and periodic boundary in cylindrical coordinate system are presented in Subsections 3.2.1, 3.2.2, and 3.2.3. All of the cylindrical array antennas measured in this work are faceted cylindrical phased array antennas. Therefore Section 3.3 presents an alternative griding system for modeling the antennas element of faceted cylindrical phased array with periodic boundary. Section 3.5 elaborates the validation of the simulation data from *PASim* program using a simple patch antennas, patch antenna with slots, and multilayer patch antenna from MIT LL.

The discussion of antennas measurement in an anechoic chamber is presented in chapter 4. In Section 4.1, the coordinate systems used in antennas measurements and the definitions of cross polarization is given. The measurement set-up for near-field and far-field measurement are explained in Section 4.2. In this section, the old far-field chamber (was be located at One Partner Place on The University of Oklahoma's Research Campus) is validated with the NEXRAD feed antennas measured in new far-field range. The active element pattern or embedded element pattern measured in near-field chamber needs to be processed to generate array pattern for planar and faceted cylindrical array using a MATLAB program. The theoretical background of this data processing is presented in 4.3.

A brief system description and measurements of Configurable Phased Array Demonstrator (CPAD) is presented in Chapter 5. In section 5.1 the description and illustration of system level designing are given. CPAD-I (Configurable Phased Array Demonstrator version 1) was configured into planar 4×4 array (Section 5.2), planar 2 mirrored array (Section 5.3), and 16-elements ring array (Section 5.4). CPAD-II has 64 elements and measurement of planar and cylindrical arrays are discussed in Section 5.5 and Section 5.6.

The physical knowledge of array elements or the measurement of active element

pattern and the FDTD method with PBC is used to propose two schemes to predict the array broadside pattern in Chapter 6. The chapter starts with a brief literature review of analyzing methods for finite array antennas. The goals and requirements of analyzing tools for future multi-functional phased array antennas are discussed in Section 6.1. The fundamental theories and techniques - far-field region, near-field regions, surface equivalent theory, and near-field to far-field transformation are discussed in Section 6.2. Two proposed methods, which are the central objectives of this dissertation are presented in section 6.3.

The final chapter, Chapter 7 presents a summary of the dissertation and numerous proposed future works to improve *PASim* program

Chapter 2

Overview of EM Simulation

Solving Maxwell's equations [54] in different problems was a long-lasting research interest. In fact, researchers had been investigating in this field over last century. One way to carry out solving Maxwell's equations is by using analytical techniques. Even though analytical methods can solve problems with simple geometrical shapes such as spheres, cylinders, and planes, it gets more tedious mathematically when the problem has complex geometrical details. The numerical techniques for solving electromagnetic problems are the most attractive method, especially in engineering applications. The field of computational electromagnetic started evolving in the early 1960s. Those methods can be categorized as time-domain solvers and frequency domain solvers as illustrated in Figure 2.1. A time-domain method solution and a frequency-domain solution can be related with Fourier transform. The time-domain method can be further divided into two groups : integral equation (IE) solvers and partial differential equation (PDE) solvers. The numerical method and asymptotic method are two major categories, which can be included in the frequency domain method.

During the last five decades, there were three most predominant computational methods developed for full-wave electromagnetic simulations. Those were Finite-Difference Time-Domain (FDTD) Method, Finite Element Method (FEM), and Method of Momentum (MoM). In addition to them, there were many other hybrid

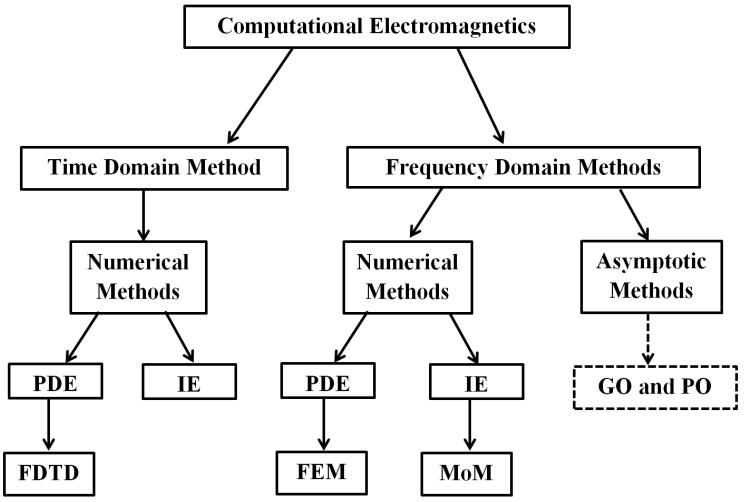

FIGURE 2.1: Computational methods for electromagnetic analysis

techniques and high-frequency methods. The high-frequency techniques, such as physical optics (PO) and uniform theory of diffraction (UTD) are based on ray theory, diffraction theory, and perturbation theory. Most of the electromagnetic solvers emerged with the rapid increase in the computational capability of processing units in 1990's. Present-day solving Maxwell's equation can be done with many commercially available proprietary software and free/open source software with astounding success. Since the primary focus of this work is to solve the electromagnetic problem of large phased array antennas, the discussion will be emphasized upon solving Maxwell's equation more accurately and rapidly on large scales.

2.1 Solving Maxwell's Equations in Time & Frequency Domains

The differential form of Maxwell equation is presented in equations 2.1 (Maxwell-Ampere's Law), 2.2 (Faraday's Law), 2.3 (Gauss's Law for Electric field), and 2.4 (Gauss's Law for Magnetic field). $\vec{E}$, $\vec{H}$, $\vec{D}$, $\vec{B}$, $\vec{J}$, $\vec{M}$, ρ_e, and ρ_m are the electric field strength vector, magnetic field strength vector, electric displacement vector,

magnetic flux density vector, electric current density vector, magnetic current density vector, the electric charge density, and magnetic charge density respectively.

$$\nabla \times \vec{H} = \frac{\partial \vec{D}}{\partial t} + \vec{J} \tag{2.1}$$

$$\nabla \times \vec{E} = -\frac{\partial \vec{B}}{\partial t} - \vec{M} \tag{2.2}$$

$$\nabla \cdot \vec{D} = \rho_e \tag{2.3}$$

$$\nabla \cdot \vec{B} = \rho_m \tag{2.4}$$

2.1.1 The Finite Difference Method

The finite difference method is the oldest among all the other numerical computation methods used in the computational electromagnetics. The main branch of this approach is the finite difference time domain method, which was first proposed by Yee in 1966 [55]. Since it is the simplest method among other electromagnetic solvers, FDTD is the right place to start understanding a problem with rudimentary mathematics. After all, it is a time domain method, with which one can do the transient analysis using the variation of the electric/magnetic field, electric/-magnetic current density, or electric/magnetic flux densities in the time domain.

2.1.1.1 The Basic Idea of The Finite Difference Method

One can find the approximation value of a differential of a function at a given point (or gradient at a given point) by using differencing equation, which can be written as forward differencing formula (equation 2.5), backward differencing formula (equation 2.6), and central differencing formula (equation 2.7) :

$$f'(x) = \frac{df(x)}{dx} \approx \frac{f(x+\Delta_x) - f(x)}{\Delta_x} \tag{2.5}$$

$$f'(x) = \frac{df(x)}{dx} \approx \frac{f(x) - f(x-\Delta_x)}{\Delta_x} \tag{2.6}$$

$$f'(x) = \frac{df(x)}{dx} \approx \frac{f(x+\Delta_x) - f(x-\Delta_x)}{2\Delta_x} \tag{2.7}$$

Using the Taylor series, we can do the error analysis of those differencing equations. The Taylor series of $f(x+\Delta_x)$ and $f(x-\Delta_x)$ can be written as in equation 2.8a and equation 2.8b respectively.

$$f(x+\Delta_x) = f(x) + f'(x)\Delta_x + \frac{1}{2}f''(x){\Delta_x}^2 + \frac{1}{6}f'''(x){\Delta_x}^3 + ... \tag{2.8a}$$

$$f(x-\Delta_x) = f(x) - f'(x)\Delta_x + \frac{1}{2}f''(x){\Delta_x}^2 - \frac{1}{6}f'''(x){\Delta_x}^3 + ... \tag{2.8b}$$

Using equations 2.8a and 2.8b, one can show that the forward differencing formula and the backward differencing formula are first-order accurate ($O(\Delta_x)$). On the other hand central differencing formula is more accurate, which is second-order accurate ($O({\Delta_x}^2)$).

2.1.1.2 The FDTD Algorithm in 1D problem

The one-dimensional Maxwell's equation in source free problem can be written as equation 2.9a (Faraday Law) and 2.9b (Ampere-Maxwell Law). Assume that the electric field only has a non-zero component in z direction and the magnetic field has a non-zero component in y direction only.

$$\mu\frac{\partial H_y}{\partial t} = \frac{\partial E_z}{\partial x} \tag{2.9a}$$

$$\epsilon\frac{\partial E_z}{\partial t} = \frac{\partial H_y}{\partial x} \tag{2.9b}$$

In equations 2.9a and 2.9b, temporal derivative of the electric (or magnetic) field is related to spatial derivative of the magnetic (or electric) field. The Equations 2.5, 2.6, and 2.7 can be used to write differencing equations with first-order accuracy in spatial partial derivatives and second-order accuracy in temporal partial derivatives.

$$\mu\left(\frac{{H_y}^{n+\frac{1}{2}}\left[i+\frac{1}{2}\right]-{H_y}^{n-\frac{1}{2}}\left[i+\frac{1}{2}\right]}{\Delta_t}\right)=\frac{{E_z}^{n}[i+1]-{E_z}^{n}[i]}{\Delta_x}$$

$${H_y}^{n+\frac{1}{2}}\left[i+\frac{1}{2}\right]={H_y}^{n-\frac{1}{2}}\left[i+\frac{1}{2}\right]+\frac{\Delta_t}{\mu\Delta_x}\left({E_z}^{n}[i+1]-{E_z}^{n}[i]\right) \tag{2.10a}$$

$$\epsilon\left(\frac{{E_z}^{n+1}[i]-{E_z}^{n}[i]}{\Delta_t}\right)=\frac{{H_y}^{n+\frac{1}{2}}[i+\frac{1}{2}]-{H_y}^{n+\frac{1}{2}}[i]}{\Delta_x}$$

$${E_z}^{n+1}[i]={E_z}^{n}[i]+\frac{\Delta_t}{\epsilon\Delta_x}\left({H_y}^{n+\frac{1}{2}}\left[i+\frac{1}{2}\right]-{H_y}^{n+\frac{1}{2}}\left[i-\frac{1}{2}\right]\right) \tag{2.10b}$$

After the electric and magnetic components as illustrated in Figure 2.2 are computed using 2.10a and 2.10b, current densities, potentials, radiations, and s parameters can be computed.

2.1.2 The Finite Element Method

In engineering and mathematical physics, boundary value problems have to be solved very often in the fluid dynamic problem, heat transfer, mass transport, structural engineering, and electric/magnetic potential. The finite element method (FEM) is a very popular numerical procedure for getting well-approximated solution for boundary value problems. This method was first introduced in the 1940s for solving a problem in structural engineering. Hrennikoff [56] in 1941 and McHenry [57] in 1943 developed this method to find stresses in continuous solids. Courant [58] used this method to solve equilibrium and vibration problem in 1943.

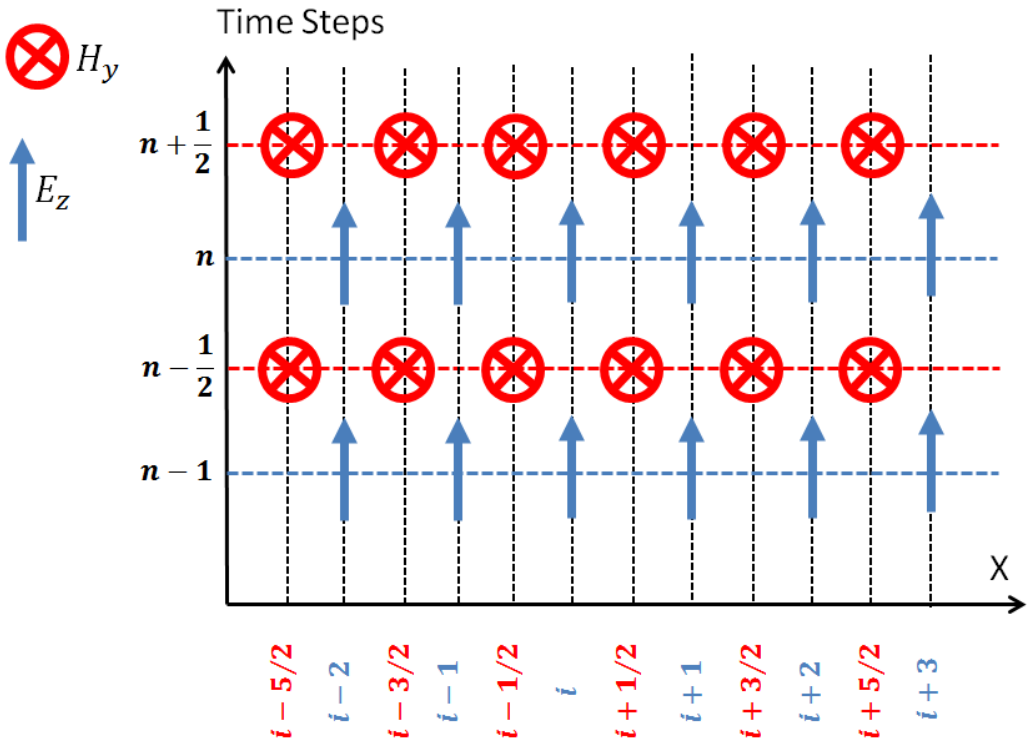

FIGURE 2.2: The arrangement of electric field and magnetic field components of 1D FDTD problem in space and time

Engineers and scientists started applying FEM in structural engineering for aircraft manufacturing industry in the 1950s. But until 1969, the FEM was not used to solve electromagnetic problems. Silvester [59] is the first researcher who used FEM to solve waveguide problem in 1969.

The Finite Element Method can be done in four steps, which are common for any boundary-value problem solving including electromagnetic problem. Each of the steps is briefly discussed in the following subsections. These are very concise descriptions of the process from very lengthy discussion from [60, 61] by Jian-Ming.

2.1.2.1 Discretization of the Domain

In this first step, the entire domain is subdivided into small domains called elements. 1D problem is the most simpler one, which has a large line segment to represent the domain and small line segments to represent elements. Discretization of the 2D problem is done using small triangles (for irregular regions) or rectangles

(for regular regions). In 3D problem, the domain can be subdivided into tetrahedra, triangle prisms, or rectangular bricks. This process is considered as the most significant task because the way the domain is discretized will effect the memory requirement, computation time, and accuracy of the solution.

2.1.2.2 Selection of the Interpolation Functions

After the completion of the first step explained in Section 2.1.2.1, suitable polynomial functions (interpolation functions) are selected to find the approximated solution for the elements. By increasing the order of polynomial functions, the accuracy of solutions can be improved. The linear polynomial is more popular interpolation function to minimize complexities of the process.

2.1.2.3 Formulation of the System of Equations

Using Ritz variational method or Galerkin method, the formulation of the systems of an equation can be done, using the solutions of elements from interpolation process in Section 2.1.2.2. In either method, the formulation is conducted through three intertwined processes.

- Formulate the equations for each element (called elemental equations).
- Build the system of equations by taking the summation of elemental equations (called the process of assembly).
- Apply the Dirichlet or homogeneous Neumann boundary condition to the system of equations.

If the problem considered is having a source or excitation, the final form of the equation is a deterministic system of equations and the problem has no sources that will be eigenvalue type system of equations.

2.1.2.4 Solution of the System of Equations

Depending on the nature of given problem, a computer will have to solve deterministic or eigenvalue matrix equation. The final step is to solve the matrix equation and obtain the solution. Then the post-processing can be run to find the output parameters, such as radiation patterns, current distributions, S-parameters, and lumped element values.

2.1.3 The Method of Moments

The method of moments or moment method had been in existence well before it was first used to solve EM problems in the 1960s. Mei and Van Bladel [62], Andreasen [63], Oshiro [64], Richmond [65], and Harrington [66] did the early research to bring this theoretical method into electromagnetic boundary value problem solver. Today this computational method is used in many commercially available electromagnetic solvers.

Let's consider integral equation which is a linear operator acting upon an unknown function (f), however, the result is a known function. This is the kind of equation we may encounter when we solve the charge distribution of the integral solution to Poisson's equation in electromagnetic. One can write the unknown function f exactly in a linear combination of expansion functions or basis functions $f_1, f_2, f_3, ...$ The number of functions can be infinity to get the exact unknown function. Since the computational need to be realistic, a finite number of basis functions are considered. By plugging in this linear combination in an integral equation, a new equation can be deduced using the linear property of integral operator. Then a set of weighting functions or testing functions is defined to take the inner product of both sides of the equation. Finally, a matrix equation will be created in the format of $[l_{mn}][\alpha_n] = [g_m]$. $[l_{mn}]$ is the inner product of the integrally operated basis function with a m number of testing functions. $[\alpha_n]$ is the n number of

constant which needs to be determined. $[g_m]$ is a known matrix. Using the appropriate procedure, the inverse of $[l_{mn}]$ can be computed and the vector $[\alpha_n]$ can be obtained. Then the unknown function may be computed using $f = \sum \alpha_n f_n$.

2.1.4 High-Frequency Asymptotic Techniques

The high-frequency asymptotic techniques are used when the geometry of the object is much larger than the smallest wave of the problem. In addition to that, the geometrical features of the object of the problem should not be small to get the accurate simulation results. Asymptotic theory can be categorized into two major classes of solvers based on geometrical optics (GO) [67] and physical optics (PO). The computational method based on geometrical optics are using the Snell's law as the underlying principle. Geometrical theory of diffraction (GTD) [68–70], uniform theory of diffraction (UTD) [71, 72], uniform asymptotic theory (UAT) [73, 74], and spectral theory of diffraction (STD) [75, 76] are the derivatives of the geometrical optics. In physical optics, the lit region and shadow region will be detected and compute the induced current densities ($\vec{J_s} = \hat{n} \times \vec{H}$) in those regions. The assumption of neglecting the effect of geometrical discontinuities is made intrinsically in this method. The induced current in the lit region will be calculated with the equation 2.11a and the induced current in the shadow region will be calculated with the equation 2.11b.

$$\vec{J_s} \approx 2\hat{n} \times \vec{H}^{inc} \tag{2.11a}$$

$$\vec{J_s} \approx \vec{0} \tag{2.11b}$$

Then there will be a discontinuity on the boundary between the lit region and the shadow region, even though the geometrical discontinuity will not necessarily exist. By taking the radiation integral or the PO integral of those currents, far-field radiation can be calculated. The physical theory of diffraction (PTD) is

a derivation of physical optics. The physical theory of diffraction improves the accuracy by introducing non-uniform fringe currents to create the geometrical discontinuity.

2.1.5 Hybrid Techniques

In Section 2.2, there is a discussion about strengths and weaknesses of FDTD, FEM, and MoM methods. None of these methods can be considered as the best method for general EM Solver development. In addition to those predominant methods, the finite element time domain (FETD) method, the finite-volume time-domain (FVTD) method, the plane-wave time-domain (PWTD) algorithm, discontinuous Galerkin time domain (DGTD) method, the conjugate gradient fast Fourier transform (CGFFT) method, and asymptotic method as discussed in Section 2.1.4 can have their own strength and weakness in electromagnetic simulation. Hybridization of those methods can compensate one method's weakness with another method's strength. Either numerical algebra or physical principles can be used to do these hybridizations of different methods.

Hybridization of the Finite Element and Finite Difference (hybrid FE-FD) Methods is the combination of finite element time domain (FETD) method with the FDTD method. Indisputably, in this hybridization, the weakness of the FDTD method which is the incapability to model complex geometrical details should be compensated. A strength of the FDTD method is the ability to simulate large structure, which can be inherited in this method. The hybridization of the Finite Element and the Boundary Integral (FE-BI) methods is another well-known combination. Another weakness of FEM is the requirement of an ABC or a PML to truncate the domain of a given problem, even though it may need to deal without any truncation in the radiation analysis. But the Method of Moments models the problem with an appropriate Green function. The hybridization of FEM and

MoM is capable of simulating highly complicated electromagnetic problems with complex geometries and materials.

2.2 General Comparison of EM Solvers

Since there is no need for solving matrix equations, in general, the FDTD method is computationally efficient. The method is directly derived from Maxwell's equation and it can be used to solve virtually any electromagnetic problem. The simplicity of the method is an enormous advantage as this is the only method which can be implemented with less amount of work. The material anisotropy and inhomogeneity can be modeled more accurately and easily. Many EM solvers using FDTD computation use the rectangular grid to represent the geometrical details of the problem, which can be fairly accurate to represent the geometrical information. But this method with the regular grid is incapable of accurately modeling the tiny geometrical details of the problem. One can use conformal grids, irregular unstructured grids, or sub-grids to overcome this disadvantage at the cost of simplicity and efficiency of the solver. The method is well suited for modeling and simulation of electrodynamic problems since the intertwinement of electric and magnetic fields are modeled correctly. The homogeneous and inhomogeneous penetrabilities in FDTD are in optimum level in both open region problems and guided wave problems [77]. The guided wave problem space can be simulated in a much wider frequency band by selecting the proper exciting waveform. Since FDTD is in the time domain, the program can provide the data, while the time-marching-loop is in progress. The FDTD can model problems with dispersive and nonlinear materials accurately which is one of the alluring features of the method.

Modeling complex geometrical details of the problem using EM solver, which employs FEM, is much more accurate and versatile. But the exponential growth of the matrix dimension can limit the size of a problem domain, due to the limit of computer capacity. Since it is in the frequency domain, the transient solution

can not be achieved. The guided wave problem space can be simulated in a satisfactory range of frequency band and better frequency scaling than it in MoM. The homogeneous and inhomogeneous penetrabilities of FEM in both open region problems and guided wave problems are comparable with the FDTD solver [77]. The EM problem with dispersive materials can be modeled very easily using FEM. The ability to use higher-order basis functions in a conformal element can model the electromagnetic interaction with material more accurately. FEM EM solvers can easily simulate the other physical phenomena such as mechanical or thermal solutions since the thermal and mechanical problems can be formulated as boundary value problems. Unlike the FDTD method, Time domain FEM can be made unconditionally stable.

The Method of Moments is particularly more efficient in simulating one denominational and two denominational objects since one or two denominational objects are exclusively subjected to mesh, and not the air region around the object. MoM is inherently capable of handling an electromagnetic problem with radiation at the far-field range. Then EM simulators with MoM are more suitable for solving electromagnetic radiation and scattering problems. The current densities from near zone and far zone sources are very common in studying, designing, and synthesizing antennas. Because MoM directly finds the current densities, MoM is more capable of simulating antennas fabricated with microstrip technology. MoM is computationally expensive when the material is inhomogeneous. It is more efficient and accurate for perfectly or highly conducting surfaces. When the MoM formulation is based on the magnetic field integral equation, the solver can be used in a particular set of problems. MoM is not a very efficient method for simulation in a large frequency range. When the number of frequency points is increased, computation time increase very rapidly. As an example, if a problem with the homogeneous material is simulated with ten frequency points and 20 frequency points, simulation with 20 frequency points will take 64 times more CPU usage than the simulation with ten frequency points.

Software Name	Developer	Method	License
HFSS	Ansys	FEM, FE-BI	Proprietary
FEM Element	Keysight	FEM	Proprietary
FDTD Element	Keysight	FDTD	Proprietary
Momentum	Keysight	MoM	Proprietary
xFDTD	Remcom	FDTD	Proprietary
FEKO	Altair	MoM, MoM-PO	Proprietary
CST MWS	CST	FDTD	Proprietary
NEC	Burke	MoM	GPL
openEMS	Liebig	FDTD	GPL
Meep	MIT	FDTD	GPL
FDTD++	Biosketch	FDTD	GPL

TABLE 2.1: Commercial and Free electromagnetic solvers.

From the above comparison, one can recognize FDTD as the most attractive method for an academic project because it is simple to implement, can be used in a large range of applications, and is able to simulate in broad frequency bandwidth without needing extensive computational time. But FDTD, FEM, and MoM are used in many EM solvers as listed in Table 2.1, which are available as free or proprietary solvers. MoM is the most common method in many cases for last few decades, but FDTD is being adapted in many solvers due to the advancement of GPU and parallel computing.

2.3 *P*hased *A*rray *Sim*ulator (*PASim*)

2.3.1 Motivation to Develop another EM Solver

Simulation of a large finite phased array antenna is a challenging task, which has to be confronted. The commercial software listed in 2.1 can provide excellent simulation results. They are not very capable of producing accurate simulation results of a large finite array with limited computational resources. Therefore there is a need for building a new simulator for solving the particular electromagnetic problem. The *PASim* was created as an attempt to build a successful EM solver for the finite phased array simulation.

2.3.2 Capabilities of *PASim*

Since *PASim* is a "home-build" FDTD code, it has all the benefits of being flexible and expandable. Originally, it was based on the FDTD theory and MATLAB code for rectangular grid from [53]. Then it was extended for the cylindrical grid, non-orthogonal unstructured grid, periodic boundary condition, and finite array simulation using an efficient algorithm. Since there is no air gap in the directions of $+\hat{x}$, $-\hat{x}$, $+\hat{y}$, and $-\hat{y}$ the time taken for simulating an active element pattern in infinite-by-infinite array is less than the time, which requires simulating an isolated element[1].

The first version of *PASim* was written in C programming language. Even though C and C++ programming languages are ideal options for this kind of heavy numerical computational task, Java programming language had to be used to minimize the debugging and diagnostic time. The *PASim* written in Java programming language is 2 to 3 times slower than the *PASim* written in C programming language. As the ultimate objective is to implement a fast algorithm for large finite array simulation rather than building a final product ready to ship, this compromise had to be made.

2.3.3 Abstract Functional Illustration of *PASim*

The *PASim* program has three major functionalities: preprocessing, time-marching-loop, and post-processing. In preprocessing the definition of the problem, initialization of the variables, and calculation of the updating coefficients will be carried out. The time-marching-loop is the main functionality of this program, which will calculate all the variable (electric and magnetic field components) values in a time domain. In addition, it will be used to correct the value at output probes and near-field electric and magnetic current information in the frequency domain. Finally, the s-parameter calculation using voltage and current data at defined

[1] 17/25 is the approximated ratio between the elapsed time for simulating an active element pattern in infinite-by-infinite array and the elapsed time for simulating an isolated element

ports and near-field to far-field transformation using electric and magnetic current components will be performed in the post-processing function.

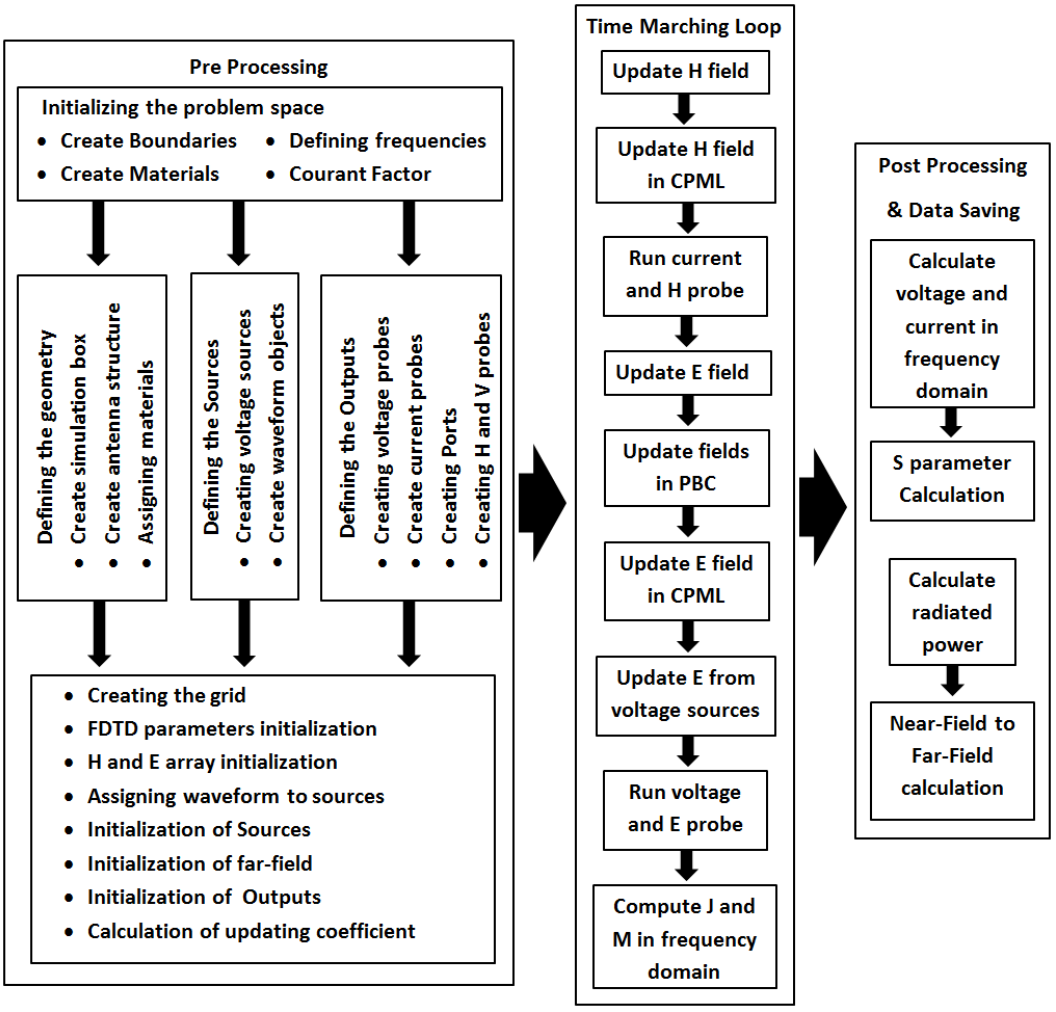

FIGURE 2.3: Abstract Functional Illustration of *PASim*

The number of time steps, Courant factor, default number of Yee cells per wavelength, port frequencies, far-field frequencies and dimensions of Yee cell are the problem space parameters which should be defined as the first task of the program. The number of time steps and the dimensions of Yee cell can be edited by both user and the program. The next task is to define the boundary condition of the problem space. Three kinds of boundaries are used in this program. The convolutional perfectly match layer (CPML), periodic boundary condition (PBC), and X-boundary (new fictitious boundary introduced in this work). The electrical

and magnetic properties of materials (ϵ_r, μ_r, σ^e, and σ^m) used to build the structure or antenna should be entered by the user or read from a data file. The loss tangent ($\tan\delta$) can be used to calculate σ^e for some materials. The user can enter the problem geometry with the dimension, location, and material type of basic brick-shaped objects in Meters. Then the program will assign the materials to those geometrical objects. Using those geometrical details, the electrical and magnetic property arrays are built and computed for both isotropic and anisotropic materials. All the non-homogeneous material components will be approximated using proper approximation strategies. When the material is partially filed in a Yee cell, the sub-cell averaging scheme can be used to find the effective electric and magnetic properties [53]. If the sub-cell averaging scheme is neither acceptable nor necessary, the program can carry out a snapped-to-grid scheme. Defining the material properties of an electric conductor with the zero thickness is accomplished by assigning material properties two-dimensionally. Voltage sources are used as the excitation in this program and they are defined with 50Ω internal resistors [53]. Those voltage sources are initialized with Gaussian or normalized derivative of a Gaussian or cosine-modulated Gaussian waveform. FDTD program with periodic boundary condition is using cosine-modulated Gaussian waveform as it can define a waveform in a narrow band of frequency. Updating coefficients will be calculated before finishing the preprocessing, since the material properties are considered time-invariant (not depending on the temperature or field intensity). Within the time-marching-loop, most of the unknown variables are computed as the loop is incrementing in time steps. Updating magnetic field components will be performed in problem space as the first step and then CPML region electric field as the next step. After updating all the magnetic field components current samples will be computed and collected at designated ports for computing S-parameters. In the next sequence of operations, the electric field components are computed and voltage samples are collected at port's locations. In addition to that, if there is any periodic boundary defined in the problem, updating field components at periodic

boundaries are carried out (this will be discussed exclusively in chapter 3). After updating all the electric and magnetic field components, electric field updates due to the voltage source are applied. Finally electric and magnetic current density components on the imaginary near-field closed surface are computed and collected in the frequency domain. This sequence of operations is recursively performed until reaching the defined number of time steps or reaching the loop terminating criteria.

The final of the three major functionality is used to calculate voltage and current in the frequency domain, the impedance in the frequency domain, S-parameters and to convert current densities on the near-field surface to electric and magnetic field components in far-field. Near-field to far-field transformation is discussed in Chapter 6. If there are any field probes, surface current probes are defined in the first major steps, and those data can be converted to frequency domain at this stage. As an example, if all the electric field components in the $\vec{x}$ and $\vec{y}$ direction on a planar surface at fixed Z location, the transient analysis of electric field on that plane can be carried out. After all the data processing is done the program will save S-parameters, voltages, currents, and far-field data.

PASim program is integrated into the genetic algorithm to do the electromagnetic optimization of radiating element as illustrated in Figure 2.4. This enables the patch antenna optimization in two different ways. The first method is changing the selected variables (dimension of the patch and location of the ports) randomly to create a population. This is the most typical electromagnetic optimization that is available in almost all of the commercially available solvers. The second method is a broader way of doing optimization. In the second optimization process, the microstrip patch of a known good antenna will be fragmented into small microstrip patches. Then the population will be created by switching them on (present) and off (absent) individually. These types of patch antennas are investigated by some researchers [78, 79] and *PASim* can pave the way to optimized known good patch antenna to enhance more desired characteristics.

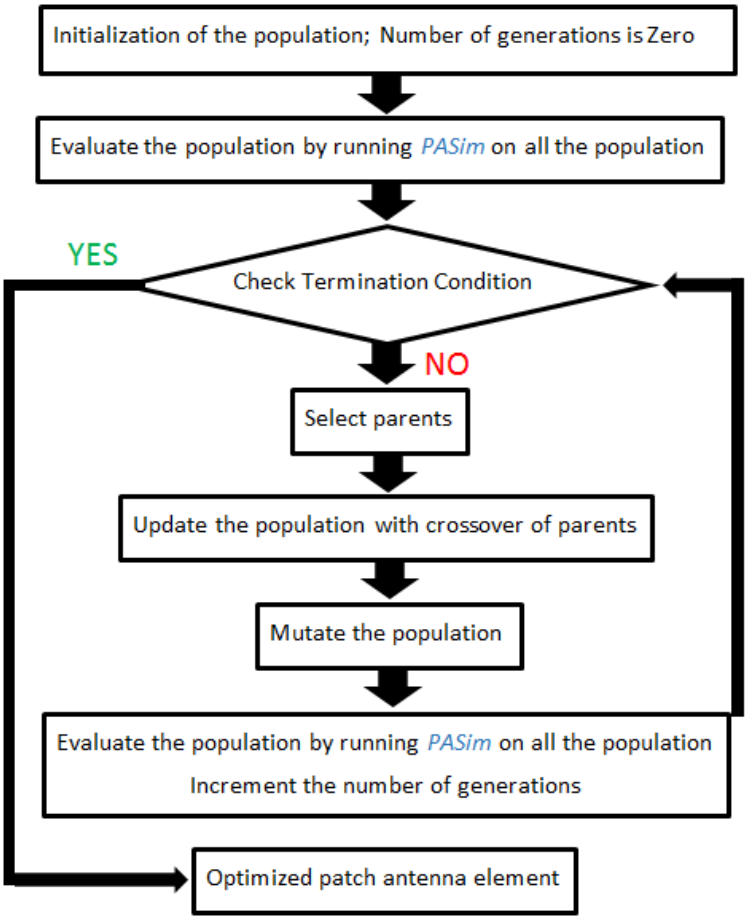

FIGURE 2.4: Genetic algorithm used in *PASim* Program

Chapter 3

FDTD Simulation of Infinite Array Antenna with Different Manifolds

The EM full-wave simulation program can be implemented with the well established FDTD updating equations and PML theory, which can be found in [53, 80]. The basic idea of FDTD simulation is to determine electric and magnetic field components at each point of discretized finite space and time of the given problem space. FDTD theory in the rectangular coordinate system can be extended for other orthogonal grids such as cylindrical coordinate system and spherical coordinate system, nonuniform grids, non-orthogonal grids, curvilinear grids, locally conformal/globally orthogonal grids, and unstructured grids.

The FDTD updating equations in the cylindrical grid for isotropic media can be found in [80]. In this chapter, the FDTD updating equation for anisotropic media will be presented. These equations can be used to simulate a fully conformal cylindrical phased array antenna. But in real world applications, the fabrication of this kind of large array may not be economical. In addition, most of the prototype cylindrical arrays are not fully conformal. As an example, the cylindrical array measured in this work was fabricated with planar linear (or column) arrays, which

are called faceted-cylindrical arrays. The simulation of a faceted-cylindrical array in a nonorthogonal grid can be done using an extended version of the FDTD theory in the rectangular grid for an isotropic material.

To simulate active element patterns, the infinite-by-infinite size of the array is assumed, which is a good approximation for a majority of active elements in a large array. A periodically arranged patch antenna is modeled as the unit cell. The FDTD model for the unit cell of a planar phased array can be depicted as in figure 3.1. The number of Yee cells [55] in the $\hat{x}$ and $\hat{y}$ directions in the mesh will accommodate only the patch antenna, since the model is using PBC in $\hat{x}$ and $\hat{y}$ direction and there should not be any air gap between elements. This EM solver can be used to generate isolated element patterns and AEP for finite-by-infinite array and infinite-by-infinite array as well.

3.1 The FDTD Method with Rectanguler Grid

The original proposal of FDTD method for electromagnetic simulation by Yee [55] was derived for the rectangular coordinate system. More comprehensive presentation of the FDTD updating equations, ABC, PML, CPML, and PBC in the rectangular coordinate system can be found in many publications [53, 80]. The FDTD theory for anisotropic media can be found in [53]. For connivance, the updating equations for the rectangular grid are listed in apendix B.

3.1.1 Numerical Dispersion and Stability

The numerical dispersion is used to analyze the limitation of simulation accuracy for electrically large structures. Numerical dispersion can create phase shifting and that phase shifting can be assimilated through the time-marching-loop. This unnatural phenomena can create completely bogus results. Since the discussion of electrically large finite array structures is the central piece of this research, the

analysis of numerical dispersion is important in different girds. The physical dispersion relation can be presented in equation 3.1 and the numerical dispersion relation can be presented in equation 3.2. The derivation and more detail discussion of those relations can be found in [80]. In these relations, c is the speed of light, k_x, k_y, and k_z are spatial frequencies, and ω is the temporal frequency.

$$\left(\frac{\omega}{c}\right)^2 = k_x^2 + k_y^2 + k_z^2 \tag{3.1}$$

The equation 3.2 will deduce to physical dispersion relation, as $\Delta_x \to 0$, $\Delta_y \to 0$, $\Delta_z \to 0$ and $\Delta_t \to 0$. Therefore smaller Yee cell sizes form a substantially smaller numerical dispersion, since Δ_t will be determined by the spatial parameters (inequality 3.3).

$$\begin{aligned}\left[\frac{1}{c\Delta t}\sin\left(\frac{\omega\Delta t}{2}\right)\right]^2 = &\left[\frac{1}{\Delta x}\sin\left(\frac{k_x\Delta x}{2}\right)\right]^2 \\ &+ \left[\frac{1}{\Delta y}\sin\left(\frac{k_y\Delta y}{2}\right)\right]^2 \\ &+ \left[\frac{1}{\Delta z}\sin\left(\frac{k_z\Delta z}{2}\right)\right]^2\end{aligned} \tag{3.2}$$

Since the discretization process of space and time in the FDTD method will approximate the real properties of vacuum or free space, the period of sampling will control the error generation, propagation, convergence, and divergence. Numerical stability study will determine the restriction of sampling period of space (Δ_x, Δ_y, and Δ_z parameters) and time (Δ_t parameter). The Courant-Friedrichs-Lewy (CFL) factor is used to determine the numerical stability of the FDTD numerical approximation, which can be given as in inequality 3.3 for the rectangular grid.

$$\Delta_t \leqslant \frac{1}{c\sqrt{\frac{1}{(\Delta_x)^2} + \frac{1}{(\Delta_y)^2} + \frac{1}{(\Delta_z)^2}}} \tag{3.3}$$

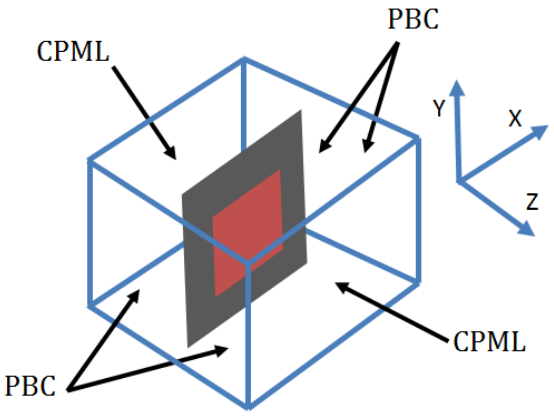

FIGURE 3.1: Unit cell for FDTD simulation for Planar array.

3.1.2 Periodic Boundary Condition

In this EM simulator, these updating equations are altered to realize the periodic boundaries as in [81–83]. Yee cells at $i_x = 1$, $i_y = 1$, $i_x = N_x + 1$, and $i_y = N_y + 1$ are used to form the periodic boundaries as illustrated in Figure 3.2. In the $+\hat{z}$ and $-\hat{z}$ directions, convolutional perfectly match layers (CPML) are implemented with proper air gaps to truncate the problem space in the finite region. The PBC method used in this program is called *constant horizontal wavenumber approach* [84–86]. This approach can be used for simulating EM structures in a wide-band frequency domain. Since the same approach was adapted to implement the periodic boundary condition in cylindrical and nonorthogonal grids in sections 3.2.3 and 3.3.3, the detailed procedure with equations of this approach in the rectangular grid are not presented in this section. But the exclusive discussion of this approach can be found in the chapter 14 of the newer edition of [53]. Figure 3.2 illustrates the electric field calculation procedure of *constant horizontal wavenumber approach* in rectangular grid. The problem space is surrounded with electric field components which are tangent to the terminating surface. This is the way to discretize the electric field in all of the other cases in this simulation program. Therefore, as an example, E_y and E_z electric field components can be found on the yOz surface at $i_x = N_x + 1$. In other words, The sizes of E_x, E_y, E_z, H_x, H_y, and

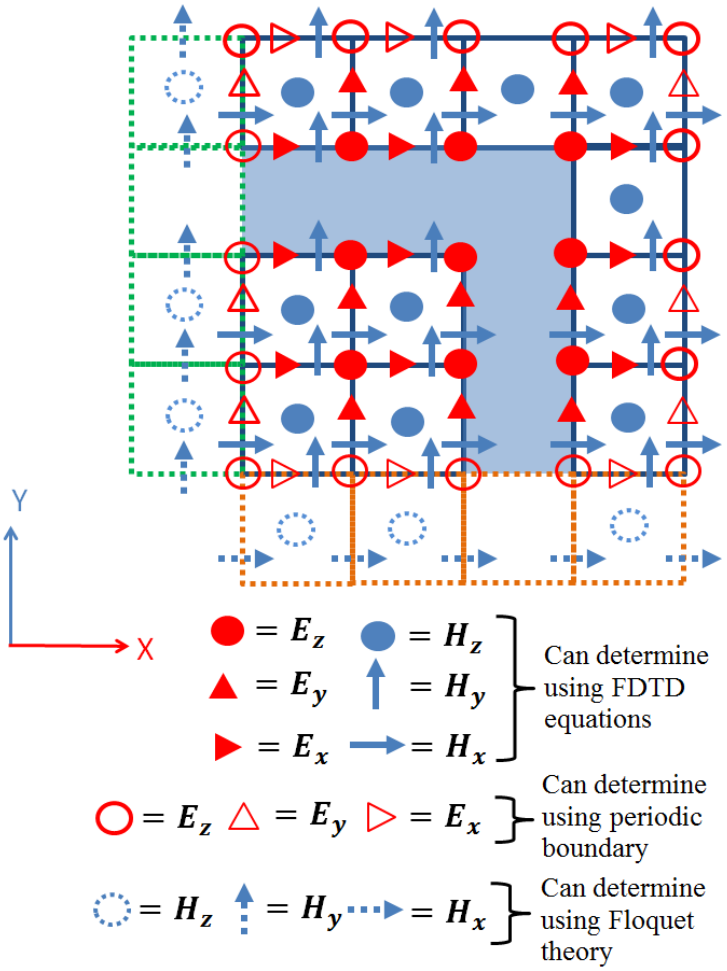

FIGURE 3.2: Field components in one unit cell.

H_z are $(N_x)\times(N_y+1)\times(N_z+1)$, $(N_x+1)\times(N_y)\times(N_z+1)$, $(N_x+1)\times(N_y+1)\times(N_z)$, $(N_x+1)\times(N_y)\times(N_z)$, $(N_x)\times(N_y+1)\times(N_z)$, and $(N_x)\times(N_y)\times(N_z+1)$ respectively. In the case of CPML, the electric field components on the terminating surface are forced to be zero in the entire time marching loop. However in the case of PBC, those electric field components which are illustrated by red circles and tangles with no fill, in Figure 3.2, are not zero and need to be updated using magnetic field components looping around them. The magnetic filed components which are illustrated by blue dashed circles and arrows do not exist in the problem space. Then in this procedure, electric field components inside the problem space are updated with FDTD updating equations, while the electric field components tangent to the periodic boundary are updated with the FDTD equation modified

by Floquet theory.

3.2 The FDTD Method for Cylindrical Grid

3.2.1 Derivation of FDTD Updating Equations for Diagonally Anisotropic Media in Cylindrical Coordinate System

Most of the derivations of Yee algorithm that can be found in the literature are for problem space in the rectangular coordinate system filled with isotropic media. However, as we discussed before, there are strong needs for FDTD solutions in cylindrical coordinates. In this section, the Yee algorithm is re-derived for diagonally anisotropic media in cylindrical coordinate systems starting from Maxwell's equations.

In this derivation, 2.1 and 2.2 will be used to derive field updating equations and updating coefficients. Constitutive relations are for linear materials which can linearly relate electric/magnetic fields with electric/magnetic flux densities (equations 3.4a and 3.4b) and electric/magnetic fields with electric/magnetic current densities (equations 3.4c and 3.4d).

$$\vec{D} = \underline{\epsilon}\vec{E} \tag{3.4a}$$

$$\vec{B} = \underline{\mu}\vec{H} \tag{3.4b}$$

$$\vec{J}_c = \underline{\sigma^e}\vec{E} \tag{3.4c}$$

$$\vec{M}_c = \underline{\sigma^m}\vec{H} \tag{3.4d}$$

$\underline{\epsilon}$, $\underline{\mu}$, $\underline{\sigma^e}$, and $\underline{\sigma^m}$ are diagonal tensors for electric permittivity, magnetic permeability, electric conductivity and magnetic conductivity, hence the diagonal anisotropic

material is considered. Using the constitutive relations and decomposition of electric and magnetic current densities, one can eliminate flux densities and rewrite equations 2.1 and 2.2 with material properties (equations 3.5 and 3.6.

$$\nabla \times \vec{H} = \underline{\epsilon}\frac{\partial \vec{E}}{\partial t} + \underline{\sigma^e}\vec{E} + \vec{J_i} \tag{3.5}$$

$$\nabla \times \vec{E} = -\underline{\mu}\frac{\partial \vec{H}}{\partial t} - \underline{\sigma^m}\vec{H} - \vec{M_i} \tag{3.6}$$

The Curl of vector in cylindrical coordinate system (equation B.1) can be plugged in to equations 3.5 and 3.6 to extract six scalar equations (equations 3.7, 3.8, 3.9, 3.10, 3.11, and 3.12).

$$\frac{1}{r}\frac{\partial H_z}{\partial \phi} - \frac{\partial H_\phi}{\partial z} = \epsilon_r \frac{\partial E_r}{\partial t} + \sigma_r^e E_r + J_r \tag{3.7}$$

$$\frac{\partial H_r}{\partial z} - \frac{\partial H_z}{\partial r} = \epsilon_\phi \frac{\partial E_\phi}{\partial t} + \sigma_\phi^e E_\phi + J_\phi \tag{3.8}$$

$$\frac{1}{r}\left(\frac{\partial r H_\phi}{\partial r} - \frac{\partial H_r}{\partial \phi}\right) = \epsilon_z \frac{\partial E_z}{\partial t} + \sigma_z^e E_z + J_z \tag{3.9}$$

$$\frac{1}{r}\frac{\partial E_z}{\partial \phi} - \frac{\partial E_\phi}{\partial z} = -\mu_r \frac{\partial H_r}{\partial t} - \sigma_r^m E_r - M_r \tag{3.10}$$

$$\frac{\partial E_r}{\partial z} - \frac{\partial E_z}{\partial r} = -\mu_\phi \frac{\partial H_\phi}{\partial t} - \sigma_\phi^m H_\phi - M_\phi \tag{3.11}$$

$$\frac{1}{r}\left(\frac{\partial r E_\phi}{\partial r} - \frac{\partial E_r}{\partial \phi}\right) = -\mu_z \frac{\partial H_z}{\partial t} - \sigma_z^m E_z - M_z \tag{3.12}$$

Equations 3.7, 3.8, 3.9, 3.10, 3.11, and 3.12 can be rearranged to derive equations 3.13, 3.14, 3.15, 3.16, 3.17, and 3.18. Then all the temporal derivations of the field components on the left hand side and all the electric or magnetic field components, spacial derivations of electric or magnetic field components, and current densities

are on the right hand side.

$$\frac{\partial E_r}{\partial t} = \frac{1}{\epsilon_r}\left(\frac{1}{r}\frac{\partial H_z}{\partial \phi} - \frac{\partial H_\phi}{\partial z} - \sigma_r^e E_r - J_r\right) \tag{3.13}$$

$$\frac{\partial E_\phi}{\partial t} = \frac{1}{\epsilon_\phi}\left(\frac{\partial H_r}{\partial z} - \frac{\partial H_z}{\partial r} - \sigma_\phi^e E_\phi - J_\phi\right) \tag{3.14}$$

$$\frac{\partial E_z}{\partial t} = \frac{1}{\epsilon_z}\left(\frac{1}{r}\frac{\partial r H_\phi}{\partial r} - \frac{1}{r}\frac{\partial H_r}{\partial \phi} - \sigma_z^e E_z - J_z\right) \tag{3.15}$$

$$\frac{\partial H_r}{\partial t} = \frac{1}{\mu_r}\left(\frac{\partial E_\phi}{\partial z} - \frac{1}{r}\frac{\partial E_z}{\partial \phi} - \sigma_r^m E_r - M_r\right) \tag{3.16}$$

$$\frac{\partial H_\phi}{\partial t} = \frac{1}{\mu_\phi}\left(\frac{\partial E_z}{\partial r} - \frac{\partial E_r}{\partial z} - \sigma_\phi^m H_\phi - M_\phi\right) \tag{3.17}$$

$$\frac{\partial H_z}{\partial t} = \frac{1}{\mu_z}\left(\frac{1}{r}\frac{\partial E_r}{\partial \phi} - \frac{1}{r}\frac{\partial r E_\phi}{\partial r} - \sigma_z^m E_z - M_z\right) \tag{3.18}$$

The equation 3.21 can be derived by applying finite deference equations B.5 for $\frac{\partial E_r}{\partial t}$, similar equation to B.7 for $\frac{\partial H_z}{\partial \phi}$, similar equation to B.8 for $\frac{\partial E_\phi}{\partial z}$ and the averaging equation B.10 for $E_r^{n+\frac{1}{2}}$ field components to express in E_r^n and E_r^{n+1}. Then all the electric field components are in $n+1(\sim \Delta_t(n+1))$ and n time-steps and all the magnetic field and electric current density components are in $n+\frac{1}{2}$ time-step on the left side of the equation. all the FDTD equation derived are in the same format. Left hand side electric field is the future value to be predicted from the past value of electric field component, present current density component, and present H field components (only perpendicular) surrounded by or looping around the electric field. the visual illustration of equation 3.19 is shown in Figure 3.3.

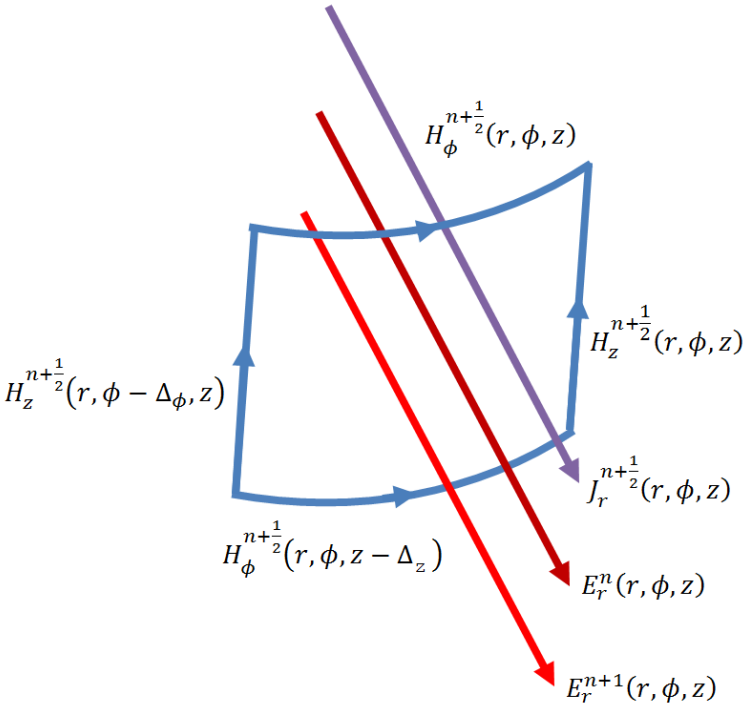

FIGURE 3.3: Field components for E_r computation formula.

$$
\begin{aligned}
E_r^{n+1}(i_r,i_\phi,i_z) &= C_{ere}(i_r,i_\phi,i_z)\times E_r^{n}(i_r,i_\phi,i_z)\\
&+ C_{erhz}(i_r,i_\phi,i_z)\times\left(H_z^{n+\frac{1}{2}}(i_r,i_\phi,i_z)-H_z^{n+\frac{1}{2}}(i_r,i_\phi-1,i_z)\right)\\
&+ C_{erh\phi}(i_r,i_\phi,i_z)\times\left(H_\phi^{n+\frac{1}{2}}(i_r,i_\phi,i_z)-H_\phi^{n+\frac{1}{2}}(i_r,i_\phi,i_z-1)\right)\\
&+ C_{erj}(i_r,i_\phi,i_z)\times J_r^{n+\frac{1}{2}}(i_r,i_\phi,i_z)
\end{aligned}
\tag{3.19}
$$

The updating coefficients $C_{ere}(i_r,i_\phi,i_z)$, $C_{erhz}(i_r,i_\phi,i_z)$, $C_{erh\phi}(i_r,i_\phi,i_z)$, and $C_{erj}(i_r,i_\phi,i_z)$ of the equation (3.19) can be computed as in equations (3.20a), (3.20b), (3.20c), and (3.20d).

$$
C_{ere}(i_r,i_\phi,i_z)=\left(\frac{2\epsilon_r(i_r,i_\phi,i_z)-{\sigma^e}_r(i_r,i_\phi,i_z)\Delta_t}{2\epsilon_r(i_r,i_\phi,i_z)+{\sigma^e}_r(i_r,i_\phi,i_z)\Delta_t}\right) \tag{3.20a}
$$

$$
C_{erhz}(i_r,i_\phi,i_z)=\left(\frac{2\Delta_t}{r\Delta_\phi\left(2\epsilon_r(i_r,i_\phi,i_z)+{\sigma^e}_r(i_r,i_\phi,i_z)\Delta_t\right)}\right) \tag{3.20b}
$$

$$
C_{erh\phi}(i_r,i_\phi,i_z)=\left(\frac{-2\Delta_t}{\Delta_z\left(2\epsilon_r(i_r,i_\phi,i_z)+{\sigma^e}_r(i_r,i_\phi,i_z)\Delta_t\right)}\right) \tag{3.20c}
$$

$$C_{erj}(i_r, i_\phi, i_z) = \left(\frac{-2\Delta_t}{2\epsilon_r(i_r, i_\phi, i_z) + {\sigma^e}_r(i_r, i_\phi, i_z)\Delta_t} \right) \tag{3.20d}$$

Applying finite deference equations B.5 for E_ϕ, B.7 for H_r, B.8 for H_z and averaging equation B.10 for E_ϕ field components, the equation 3.21 can be derived.

$$\begin{aligned} E_\phi^{n+1}(i_r, i_\phi, i_z) &= C_{e\phi e}(i_r, i_\phi, i_z) \times E_\phi^n(i_r, i_\phi, i_z) \\ &+ C_{e\phi hr}(i_r, i_\phi, i_z) \times \left(H_r^{n+\frac{1}{2}}(i_r, i_\phi, i_z) - H_r^{n+\frac{1}{2}}(i_r, i_\phi, i_z - 1) \right) \\ &- C_{e\phi hz}(i_r, i_\phi, i_z) \times \left(H_z^{n+\frac{1}{2}}(i_r, i_\phi, i_z) - H_z^{n+\frac{1}{2}}(i_r - 1, i_\phi, i_z) \right) \\ &+ C_{e\phi j}(i_r, i_\phi, i_z) \times J_\phi^{n+\frac{1}{2}}(i_r, i_\phi, i_z) \end{aligned} \tag{3.21}$$

The updating coefficients $C_{e\phi e}(i_r, i_\phi, i_z)$, $C_{e\phi hr}(i_r, i_\phi, i_z)$, and $C_{e\phi hz}(i_r, i_\phi, i_z)$ of the equation (3.21) can be computed as in equations (3.22a), (3.22b), (3.22c), and (3.22d).

$$C_{e\phi e}(i_r, i_\phi, i_z) = \left(\frac{2\epsilon_\phi(i_r, i_\phi, i_z) - {\sigma^e}_\phi(i_r, i_\phi, i_z)\Delta_t}{2\epsilon_\phi(i_r, i_\phi, i_z) + {\sigma^e}_\phi(i_r, i_\phi, i_z)\Delta_t} \right) \tag{3.22a}$$

$$C_{e\phi hr}(i_r, i_\phi, i_z) = \left(\frac{2\Delta_t}{\Delta_z \left(2\epsilon_\phi(i_r, i_\phi, i_z) + {\sigma^e}_\phi(i_r, i_\phi, i_z)\Delta_t\right)} \right) \tag{3.22b}$$

$$C_{e\phi hz}(i_r, i_\phi, i_z) = \left(\frac{-2\Delta_t}{\Delta_r \left(2\epsilon_\phi(i_r, i_\phi, i_z) + {\sigma^e}_\phi(i_r, i_\phi, i_z)\Delta_t\right)} \right) \tag{3.22c}$$

$$C_{e\phi j}(i_r, i_\phi, i_z) = \left(\frac{-2\Delta_t}{2\epsilon_\phi(i_r, i_\phi, i_z) + {\sigma^e}_\phi(i_r, i_\phi, i_z)\Delta_t} \right) \tag{3.22d}$$

Applying finite deference equations B.5 for E_z, B.7 for H_r, B.8 for H_ϕ and averaging equation B.10 for E_z field components, the equation 3.23 can be derived.

$$
\begin{aligned}
E_z^{n+1}(i_r, i_\phi, i_z) &= C_{eze}(i_r, i_\phi, i_z) \times E_z^n(i_r, i_\phi, i_z) \\
&+ C_{ezh\phi}(i_r, i_\phi, i_z) \times \left(r H_\phi^{n+\frac{1}{2}}(i_r, i_\phi, i_z) - (r - \Delta_r) H_\phi^{n+\frac{1}{2}}(i_r - 1, i_\phi, i_z) \right) \\
&- C_{ezhr}(i_r, i_\phi, i_z) \times \left(H_r^{n+\frac{1}{2}}(i_r, i_\phi, i_z) - H_r^{n+\frac{1}{2}}(i_r, i_\phi - 1, i_z) \right) \\
&+ C_{ezj}(i_r, i_\phi, i_z) \times J_z^{n+\frac{1}{2}}(i_r, i_\phi, i_z)
\end{aligned}
\tag{3.23}
$$

The updating coefficients $C_{eze}(i_r, i_\phi, i_z)$, $C_{ezh\phi}(i_r, i_\phi, i_z)$, $C_{ezhr}(i_r, i_\phi, i_z)$, and $C_{ezj}(i_r, i_\phi, i_z)$ of the equation (3.23) can be computed as in equations (3.24a), (3.24b), (3.24c), and (3.24d).

$$
C_{eze}(i_r, i_\phi, i_z) = \left(\frac{2\epsilon_z(i_r, i_\phi, i_z) - {\sigma^e}_z(i_r, i_\phi, i_z)\Delta_t}{2\epsilon_z(i_r, i_\phi, i_z) + {\sigma^e}_z(i_r, i_\phi, i_z)\Delta_t} \right) \tag{3.24a}
$$

$$
C_{ezh\phi}(i_r, i_\phi, i_z) = \left(\frac{2\Delta_t}{r\Delta_z \left(2\epsilon_z(i_r, i_\phi, i_z) + {\sigma^e}_z(i_r, i_\phi, i_z)\Delta_t\right)} \right) \tag{3.24b}
$$

$$
C_{ezhr}(i_r, i_\phi, i_z) = \left(\frac{-2\Delta_t}{r\Delta_\phi \left(2\epsilon_z(i_r, i_\phi, i_z) + {\sigma^e}_z(i_r, i_\phi, i_z)\Delta_t\right)} \right) \tag{3.24c}
$$

$$
C_{ezj}(i_r, i_\phi, i_z) = \left(\frac{-2\Delta_t}{2\epsilon_z(i_r, i_\phi, i_z) + {\sigma^e}_z(i_r, i_\phi, i_z)\Delta_t} \right) \tag{3.24d}
$$

Applying finite deference equations B.9 for H_r, B.3 for E_z, B.4 for E_ϕ and averaging equation B.10 for H_r field components, the equation 3.25 can be derived.

$$
\begin{aligned}
H_r^{n+\frac{1}{2}}(i_r, i_\phi, i_z) &= C_{hrh}(i_r, i_\phi, i_z) \times H_r^{n-\frac{1}{2}}(i_r, i_\phi, i_z) \\
&+ C_{hrez}(i_r, i_\phi, i_z) \times (E_z^n(i_r, i_\phi + 1, i_z) - E_z^n(i_r, i_\phi, i_z)) \\
&+ C_{hre\phi}(i_r, i_\phi, i_z) \times \left(E_\phi^n(i_r, i_\phi, i_z + 1) - E_\phi^n(i_r, i_\phi, i_z)\right) \\
&+ C_{hrm}(i_r, i_\phi, i_z) \times M_r^n(i_r, i_\phi, i_z)
\end{aligned}
\tag{3.25}
$$

The updating coefficients $C_{e\phi e}(i_r, i_\phi, i_z)$, $C_{e\phi hr}(i_r, i_\phi, i_z)$, $C_{e\phi hz}(i_r, i_\phi, i_z)$ and $C_{hrm}(i_r, i_\phi, i_z)$ of the equation (3.25) can be computed as in equations (3.26a),

(3.26b), (3.26c), and (3.26d).

$$C_{hrh}(i_r, i_\phi, i_z) = \left(\frac{2\mu_r(i_r, i_\phi, i_z) - {\sigma^m}_r(i_r, i_\phi, i_z)\Delta_t}{2\mu_r(i_r, i_\phi, i_z) + {\sigma^m}_r(i_r, i_\phi, i_z)\Delta_t} \right) \tag{3.26a}$$

$$C_{hrez}(i_r, i_\phi, i_z) = \left(\frac{-2\Delta_t}{r\Delta_\phi \left(2\mu_r(i_r, i_\phi, i_z) + {\sigma^m}_r(i_r, i_\phi, i_z)\Delta_t\right)} \right) \tag{3.26b}$$

$$C_{hre\phi}(i_r, i_\phi, i_z) = \left(\frac{2\Delta_t}{\Delta_z \left(2\mu_r(i_r, i_\phi, i_z) + {\sigma^m}_r(i_r, i_\phi, i_z)\Delta_t\right)} \right) \tag{3.26c}$$

$$C_{hrm}(i_r, i_\phi, i_z) = \left(\frac{-2\Delta_t}{2\mu_r(i_r, i_\phi, i_z) + {\sigma^m}_r(i_r, i_\phi, i_z)\Delta_t} \right) \tag{3.26d}$$

Applying finite deference equations B.9 for H_ϕ, B.3 for H_z, B.4 for H_r and averaging equation B.10 for H_ϕ field components, the equation 3.27 can be derived.

$$\begin{aligned} H_\phi^{n+\frac{1}{2}}(i_r, i_\phi, i_z) &= C_{h\phi h}(i_r, i_\phi, i_z) \times H_\phi^{n-\frac{1}{2}}(i_r, i_\phi, i_z) \\ &+ C_{h\phi ez}(i_r, i_\phi, i_z) \times (E_z^n(i_r + 1, i_\phi, i_z) - E_z^n(i_r, i_\phi, i_z)) \\ &+ C_{h\phi er}(i_r, i_\phi, i_z) \times (E_r^n(i_r, i_\phi, i_z + 1) - E_r^n(i_r, i_\phi, i_z)) \\ &+ C_{h\phi m}(i_r, i_\phi, i_z) \times M_\phi^n(i_r, i_\phi, i_z) \end{aligned} \tag{3.27}$$

The updating coefficients $C_{e\phi e}(i_r, i_\phi, i_z)$, $C_{e\phi hr}(i_r, i_\phi, i_z)$, $C_{e\phi hz}(i_r, i_\phi, i_z)$, and $C_{h\phi m}(i_r, i_\phi, i_z)$ of the equation (3.27) can be computed as in equations (3.28a), (3.28b), (3.28c), and (3.28d).

$$C_{h\phi h}(i_r, i_\phi, i_z) = \left(\frac{2\mu_\phi(i_r, i_\phi, i_z) - {\sigma^m}_\phi(i_r, i_\phi, i_z)\Delta_t}{2\mu_\phi(i_r, i_\phi, i_z) + {\sigma^m}_\phi(i_r, i_\phi, i_z)\Delta_t} \right) \tag{3.28a}$$

$$C_{h\phi ez}(i_r, i_\phi, i_z) = \left(\frac{2\Delta_t}{\Delta_r \left(2\mu_\phi(i_r, i_\phi, i_z) + {\sigma^m}_\phi(i_r, i_\phi, i_z)\Delta_t\right)} \right) \tag{3.28b}$$

$$C_{h\phi er}(i_r, i_\phi, i_z) = \left(\frac{-2\Delta_t}{\Delta_z \left(2\mu_\phi(i_r, i_\phi, i_z) + {\sigma^m}_\phi(i_r, i_\phi, i_z)\Delta_t\right)} \right) \tag{3.28c}$$

$$C_{h\phi m}(i_r, i_\phi, i_z) = \left(\frac{-2\Delta_t}{2\mu_\phi(i_r, i_\phi, i_z) + {\sigma^m}_\phi(i_r, i_\phi, i_z)\Delta_t} \right) \tag{3.28d}$$

Applying finite deference equations B.9 for H_z, B.3 for E_ϕ, B.8 for E_r and averaging equation B.10 for H_z field components, the equation 3.29 can be derived.

$$\begin{aligned} H_z^{n+\frac{1}{2}}(i_r, i_\phi, i_z) &= C_{hzh}(i_r, i_\phi, i_z) \times H_z^{n-\frac{1}{2}}(i_r, i_\phi, i_z) \\ &+ C_{hzer}(i_r, i_\phi, i_z) \times (E_r^n(i_r, i_\phi + 1, i_z) - E_r^n(i_r, i_\phi, i_z)) \\ &+ C_{hze\phi}(i_r, i_\phi, i_z) \times \left((r + \Delta_r)E_\phi^n(i_r + 1, i_\phi, i_z) - rE_\phi^n(i_r, i_\phi, i_z)\right) \\ &+ C_{hzm}(i_r, i_\phi, i_z) \times M_z^n(i_r, i_\phi, i_z) \end{aligned} \tag{3.29}$$

The updating coefficients $C_{hzh}(i_r, i_\phi, i_z)$, $C_{hzer}(i_r, i_\phi, i_z)$, $C_{hze\phi}(i_r, i_\phi, i_z)$, and $C_{hzm}(i_r, i_\phi, i_z)$ of the equation (3.29) can be computed as in equations (3.30a), (3.30b), (3.30c), and (3.30d).

$$C_{hzh}(i_r, i_\phi, i_z) = \left(\frac{2\mu_z(i_r, i_\phi, i_z) - \sigma^m{}_z(i_r, i_\phi, i_z)\Delta_t}{2\mu_z(i_r, i_\phi, i_z) + \sigma^m{}_z(i_r, i_\phi, i_z)\Delta_t}\right) \tag{3.30a}$$

$$C_{hzer}(i_r, i_\phi, i_z) = \left(\frac{2\Delta_t}{r\Delta_\phi\left(2\mu_z(i_r, i_\phi, i_z) + \sigma^m{}_z(i_r, i_\phi, i_z)\Delta_t\right)}\right) \tag{3.30b}$$

$$C_{hze\phi}(i_r, i_\phi, i_z) = \left(\frac{-2\Delta_t}{r\Delta_r\left(2\mu_z(i_r, i_\phi, i_z) + \sigma^m{}_z(i_r, i_\phi, i_z)\Delta_t\right)}\right) \tag{3.30c}$$

$$C_{hzm}(i_r, i_\phi, i_z) = \left(\frac{-2\Delta_t}{2\mu_z(i_r, i_\phi, i_z) + \sigma^m{}_z(i_r, i_\phi, i_z)\Delta_t}\right) \tag{3.30d}$$

3.2.2 Numerical Stability

The numerical dispersion analysis and numerical stability analysis for FDTD scheme in a cylindrical grid were done by some investigators [87–89]. The result of numerical stability analysis in a cylindrical grid is used in this program to calculate the time step size for a given Courant factor and Yee cell dimensions. The Courant-Friedrichs-Lewy (CFL) condition can be presented as in inequality 3.31.

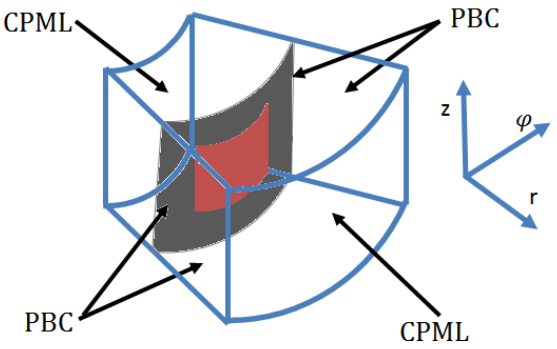

FIGURE 3.4: Unit cell for FDTD simulation for a fully conformal (circular) cylindrical array.

$$\Delta_t \leqslant \frac{1}{c\sqrt{\frac{1}{(\Delta_r)^2} + \frac{4}{(\Delta_r \Delta_\phi)^2} + \frac{1}{(\Delta_z)^2}}} \tag{3.31}$$

3.2.3 Periodic Boundary Condition

The simulation model for fully conformal cylindrical phased array antenna can be implemented using absorbing boundaries and periodic boundaries in the cylindrical coordinate system as presented in this subsection. The PBC implementation used in the rectangular grid (*constant horizontal wavenumber approach* [53]) can be adapted for PBC in the cylindrical grid and the detail computational procedure is presented in the rest of this section. The periodic boundaries are implemented in $+\hat{\phi}$, $-\hat{\phi}$, $+\hat{z}$, and $-\hat{z}$ directions and the Convolutional Perfect Match Layers (CPML) are implemented in $+\hat{r}$ and $-\hat{r}$ directions. The circular array active element or an isolated element based on the cylindrical coordinate system can be simulated by switching the PBC to CPML of the unit cell in Figure 3.4, even though the main objective is to simulate AEP of a cylindrical array antenna. The cylindrical arrays in the real world have a finite number of elements. Because of the periodicity in a circle, the antenna elements can be treated as an element in a semi-infinite array. In this theory, infinite columns are assumed on a cylinder with large radius comparing to λ.

3.2.3.1 Periodicity in $\hat{z}$ Direction

The equation (3.32) is for calculating the field components E_ϕ at the lower bound of z ($i_z = 1$). The field components $E_\phi^{n+1}(i_r, i_\phi, 1)$ is computed using $E_\phi^n(i_r, i_\phi, 1)$ and magnetic field components in $\widehat{z}$ and $\widehat{r}$ directions, which are $H_r^{n+\frac{1}{2}}(i_r, i_\phi, 1)$, $H_r^{n+\frac{1}{2}}(i_r, i_\phi, \nexists)$, $H_z^{n+\frac{1}{2}}(i_r, i_\phi, 1)$, and $H_z^{n+\frac{1}{2}}(i_r - 1, i_\phi, 1)$. The updating coefficients $C_{e\phi e}(i_r, i_\phi, 1)$, $C_{e\phi hr}(i_r, i_\phi, 1)$, and $C_{e\phi hz}(i_r, i_\phi, 1)$ of the equation (3.32) can be computed using the equations 3.22 in section 3.2.1.

$$\begin{aligned} E_\phi^{n+1}(i_r, i_\phi, 1) &= C_{e\phi e}(i_r, i_\phi, 1) \times E_\phi^n(i_r, i_\phi, 1) \\ &+ C_{e\phi hr}(i_r, i_\phi, 1) \times \left(H_r^{n+\frac{1}{2}}(i_r, i_\phi, 1) - H_r^{n+\frac{1}{2}}(i_r, i_\phi, \nexists) \right) \\ &- C_{e\phi hz}(i_r, i_\phi, 1) \times \left(H_z^{n+\frac{1}{2}}(i_r, i_\phi, 1) - H_z^{n+\frac{1}{2}}(i_r - 1, i_\phi, 1) \right) \end{aligned} \tag{3.32}$$

The magnetic field component $H_r^{n+\frac{1}{2}}(i_r, i_\phi, \nexists)$ does not exist in the problem space. Using the Floquet theory $H_r^{n+\frac{1}{2}}(i_r, i_\phi, \nexists)$ can be calculated as in equation 3.33. k_z is the wave number in $\hat{z}$ direction and can be computed as $k_z = \frac{\omega}{c} \sin \varpi_z$ (ϖ_z is the incident angle of the wave to $\hat{z}$ direction)

$$H_r^{n+\frac{1}{2}}(i_r, i_\phi, \nexists) = H_r^{n+\frac{1}{2}}(i_r, i_\phi, N_z) e^{jk_z N_z \Delta_z} \tag{3.33}$$

A similar procedure can be carried out to compute $E_\phi^{n+1}(i_r, i_\phi, N_z + 1)$. But using the Floquet theory, $E_\phi^{n+1}(i_r, i_\phi, N_z + 1)$ can be computed using $E_\phi^{n+1}(i_r, i_\phi, 1)$ as equation 3.34.

$$E_\phi^{n+1}(i_r, i_\phi, N_z + 1) = E_\phi^{n+1}(i_r, i_\phi, 1) e^{-jk_z N_z \Delta_z} \tag{3.34}$$

The equation (3.35) is for calculating the E_r field components at the lower bound of ϕ ($i_\phi = 1$). The field components $E_r^{n+1}(i_r, i_\phi, 1)$ is computed using $E_r^n(i_r, i_\phi, 1)$

and magnetic field components in z and ϕ directions, which are $H_z^{n+\frac{1}{2}}(i_r, i_\phi, 1)$, $H_z^{n+\frac{1}{2}}(i_r, i_\phi, 1)$, $H_\phi^{n+\frac{1}{2}}(i_r, i_\phi, 1)$, and $H_\phi^{n+\frac{1}{2}}(i_r, i_\phi, 1)$. The magnetic field components $H_z^{n+\frac{1}{2}}(i_r, 1, i_z)$ are at $\phi = 0$. The updating coefficients $C_{ere}(i_r, N_\phi, i_z)$, $C_{erhz}(i_r, N_\phi, i_z)$, and $C_{erh\phi}(i_r, N_\phi, i_z)$ of the equation (3.35) can be computed using equation 3.20.

$$\begin{aligned} E_r^{n+1}(i_r, i_\phi, 1) &= C_{ere}(i_r, N_\phi, i_z) E_r^n(i_r, i_\phi, 1) \\ &+ C_{erhz}(i_r, i_\phi, 1) \times \left(H_z^{n+\frac{1}{2}}(i_r, i_\phi, 1) - H_z^{n+\frac{1}{2}}(i_r, i_\phi, 1) \right) \\ &+ C_{erh\phi}(i_r, i_\phi, i_z) \times \left(H_\phi^{n+\frac{1}{2}}(i_r, i_\phi, 1) - H_\phi^{n+\frac{1}{2}}(i_r, i_\phi, 1) \right) \end{aligned} \tag{3.35}$$

The magnetic field component $H_\phi^{n+\frac{1}{2}}(i_r, i_\phi, \nexists)$ does not exist in the problem space. Using the Floquet theory $H_\phi^{n+\frac{1}{2}}(i_r, i_\phi, \nexists)$ can be calculated as in equation 3.36. k_ϕ is the wave number in $\hat{\phi}$ direction and can be computed as $k_\phi = \frac{\omega}{c} \sin \varpi_\phi$ (ϖ_ϕ is the incident angle of the wave to $\hat{\phi}$ direction)

$$H_\phi^{n+\frac{1}{2}}(i_r, i_\phi, \nexists) = H_\phi^{n+\frac{1}{2}}(i_r, i_\phi, N_z) e^{jk_z N_z \Delta_z} \tag{3.36}$$

Using the Floquet theory, $E_r^{n+1}(i_r, i_\phi, N_z+1)$ can be computed using $E_r^{n+1}(i_r, i_\phi, 1)$ as equation 3.37.

$$E_r^{n+1}(i_r, i_\phi, N_z + 1) = E_r^{n+1}(i_r, i_\phi, 1) e^{-jk_z N_z \Delta_z} \tag{3.37}$$

3.2.3.2 Periodicity in $\hat{\phi}$ Direction

The equation (3.38) is for calculating the E_z field components at the lower bound of ϕ ($i_\phi = 1$). The field components $E_z^{n+1}(i_r, 1, i_z)$ is computed using $E_z^n(i_r, 1, i_z)$ and magnetic field components in $\hat{\phi}$ and $\hat{r}$ directions, which are $H_\phi^{n+\frac{1}{2}}(i_r, 1, i_z)$, $H_\phi^{n+\frac{1}{2}}(i_r - 1, 1, N_z)$, $H_r^{n+\frac{1}{2}}(i_r, 1, i_z)$, $H_r^{n+\frac{1}{2}}(i_r, \nexists, i_z)$. The updating coefficients of the

equation (3.38) $C_{eze}(i_r, 1, i_z)$, $C_{ezhr}(i_r, 1, i_z)$, and $C_{ezh\phi}(i_r, 1, i_z)$ can be computed using equation 3.24.

$$\begin{aligned} E_z^{n+1}(i_r, 1, i_z) &= C_{eze}(i_r, 1, i_z) E_z^n(i_r, 1, i_z) \\ &+ C_{ezh\phi}(i_r, 1, i_z) \times \left(r H_\phi^{n+\frac{1}{2}}(i_r, 1, i_z) - (r - \Delta r) H_\phi^{n+\frac{1}{2}}(i_r - 1, 1, i_z) \right) \\ &+ C_{ezhr}(i_r, 1, i_z) \times \left(H_r^{n+\frac{1}{2}}(i_r, 1, i_z) - H_r^{n+\frac{1}{2}}(i_r, \nexists, i_z) \right) \end{aligned} \tag{3.38}$$

The magnetic field component $H_r^{n+\frac{1}{2}}(i_r, \nexists, i_z)$ does not exist in the problem space. Using the Floquet theory $H_r^{n+\frac{1}{2}}(i_r, \nexists, i_z)$ can be calculated as in equation 3.39. k_z is the wave number in $\hat{\phi}$ direction and can be computed as $k_\phi = \frac{\omega}{c} \sin \varpi_\phi$ (ϖ_ϕ is the incident angle of the wave to $\hat{\phi}$ direction)

$$H_r^{n+\frac{1}{2}}(i_r, \nexists, i_z) = H_r^{n+\frac{1}{2}}(i_r, N_\phi, i_z) e^{j k_\phi N_\phi \Delta_\phi} \tag{3.39}$$

Using the Floquet theory, $E_z^{n+1}(i_r, i_\phi, N_z+1)$ can be computed using $E_z^{n+1}(i_r, i_\phi, 1)$ as equation 3.40.

$$E_z^{n+1}(i_r, N_\phi + 1, i_z) = E_z^{n+1}(i_r, 1, i_z) e^{-j k_\phi N_\phi \Delta_\phi} \tag{3.40}$$

The equation (3.41) is for calculating the E_r field component at the lower bound of ϕ ($i_\phi = 1$). The field component $E_r^{n+1}(i_r, 1, i_z)$ is computed using $E_r^n(i_r, 1, i_z)$ and magnetic field components in $\hat{z}$ and $\hat{\phi}$ directions, which are $H_z^{n+\frac{1}{2}}(i_r, 1, i_z)$, $H_z^{n+\frac{1}{2}}(i_r, N_\phi, i_z)$, $H_\phi^{n+\frac{1}{2}}(i_r, 1, i_z)$, and $H_\phi^{n+\frac{1}{2}}(i_r, 1, i_z - 1)$. The updating coefficients $C_{ere}(i_r, N_\phi, i_z)$, $C_{erhz}(i_r, N_\phi, i_z)$, and $C_{erh\phi}(i_r, N_\phi, i_z)$ of the equation 3.41 can be computed using equation 3.20.

$$
\begin{aligned}
E_r^{n+1}(i_r, i_\phi, 1) &= C_{ere}(i_r, N_\phi, i_z) E_r^n(i_r, i_\phi, 1) \\
&+ C_{erhz}(i_r, i_\phi, 1) \times \left(H_z^{n+\frac{1}{2}}(i_r, i_\phi, 1) - H_z^{n+\frac{1}{2}}(i_r, i_\phi, 1) \right) \\
&+ C_{erh\phi}(i_r, i_\phi, i_z) \times \left(H_\phi^{n+\frac{1}{2}}(i_r, i_\phi, 1) - H_\phi^{n+\frac{1}{2}}(i_r, i_\phi, 1) \right)
\end{aligned} \tag{3.41}
$$

The magnetic field component $H_\phi^{n+\frac{1}{2}}(i_r, i_\phi, \nexists)$ does not exist in the problem space. Using the Floquet theory $H_\phi^{n+\frac{1}{2}}(i_r, i_\phi, \nexists)$ can be calculated as in equation 3.42. k_ϕ is the wave number in $\hat{\phi}$ direction and can be computed as $k_\phi = \frac{\omega}{c} \sin \varpi_\phi$ (ϖ_ϕ is the incident angle of the wave to $\hat{\phi}$ direction)

$$
H_\phi^{n+\frac{1}{2}}(i_r, i_\phi, \nexists) = H_\phi^{n+\frac{1}{2}}(i_r, i_\phi, N_z) e^{jk_z N_z \Delta_z} \tag{3.42}
$$

Using the Floquet theory, $E_r^{n+1}(i_r, i_\phi, N_z+1)$ can be computed using $E_r^{n+1}(i_r, i_\phi, 1)$ as equation 3.43.

$$
E_r^{n+1}(i_r, i_\phi, N_z + 1) = E_r^{n+1}(i_r, i_\phi, 1) e^{-jk_z N_z \Delta_z} \tag{3.43}
$$

3.2.3.3 Treatment at the Corners

At the corners of the cell, E_rs are updated using (3.44), (3.46), (3.47), and (3.48) equations.

$$
\begin{aligned}
E_r^{n+1}(i_r, 1, 1) &= C_{ere}(i_r, 1, 1) E_r^n(i_r, 1, 1) \\
&+ C_{erhz}(i_r, 1, 1) \times \left(H_z^{n+\frac{1}{2}}(i_r, 1, 1) - H_z^{n+\frac{1}{2}}(i_r, \nexists, 1) \right) \\
&+ C_{erh\phi}(i_r, 1, 1) \times \left(H_\phi^{n+\frac{1}{2}}(i_r, 1, 1) - H_\phi^{n+\frac{1}{2}}(i_r, 1, \nexists) \right)
\end{aligned} \tag{3.44}
$$

The magnetic field components $H_{\phi}^{n+\frac{1}{2}}(i_r, 1, \nexists)$ and $H_{z}^{n+\frac{1}{2}}(i_r, \nexists, 1)$ do not exist in the problem space. They can be calculated as in equation 3.45a and 3.45a.

$$H_{\phi}^{n+\frac{1}{2}}(i_r, 1, \nexists) = H_{\phi}^{n+\frac{1}{2}}(i_r, 1, N_z) \times e^{jk_{\phi}N_{\phi}\Delta_{\phi}} \tag{3.45a}$$

$$H_{z}^{n+\frac{1}{2}}(i_r, \nexists, 1) = H_{\phi}^{n+\frac{1}{2}}(i_r, N_{\phi}, 1) \times e^{jk_{z}N_{z}\Delta_{z}} \tag{3.45b}$$

After electric field component $E_r^{n+1}(i_r, 1, 1)$ is computed using equation 3.44, All the electric field components $E_r^{n+1}(i_r, N_{\phi}+1, 1)$, $E_r^{n+1}(i_r, 1, N_z+1)$, and $E_r^{n+1}(i_r, N_{\phi}+1, N_z+1)$ at other corners can be computed using equations 3.46, 3.47, and 3.47.

$$E_r^{n+1}(i_r, N_{\phi}+1, 1) = E_r^{n+1}(i_r, 1, 1) \times e^{-jk_{\phi}N_{\phi}\Delta_{\phi}} \tag{3.46}$$

$$E_r^{n+1}(i_r, 1, N_z+1) = E_r^{n+1}(i_r, 1, 1) \times e^{-jk_{z}N_{z}\Delta_{z}} \tag{3.47}$$

$$E_r^{n+1}(i_r, N_{\phi}+1, N_z+1) = E_r^{n+1}(i_r, 1, 1) \times e^{-jk_{\phi}N_{\phi}\Delta_{\phi}} \times e^{-jk_{z}N_{z}\Delta_{z}} \tag{3.48}$$

The convolutional perfectly match layer (CPML) for cylindrical grid [89–92] will be located in the direction of $+\hat{r}$ and $-\hat{r}$ directions in all the simulations presented in this work. If finite-by-infinite array needs to be simulated, CPML layes will be located in the direction of $+\hat{r}$, $-\hat{r}$, $+\hat{z}$, and $-\hat{z}$ directions.

3.3 The FDTD Method for Nonorthogonal and Unstructured Grid

FDTD updating equations, updating coefficients, numerical stability, numerical dispersion, and periodic boundary in the nonorthogonal and unstructured grid

will be discussed in the following subsections. Since CPML layer needs orthogonal field components, the isotropic case will only be discussed.

3.3.1 Derivation of FDTD Updating Equations

Even though FDTD updating equation can be derived for nonorthogonal grid starting from Maxwell's equation as presented in section 3.2, the derivation process is simplified by taking the geometry into consideration. In 1992, Jin-Fa Lee and others [93] presented their work on generalizing the FDTD algorithm on a nonorthogonal coordinate system. In this derivation, the initial results from Lee's generalization are used to obtain the updating equations.

Figure 3.5 illustrates the derivation of FDTD equations for electric field components using the FDTD equations for rectangular grid. Let's consider the nonorthogonal coordinate system is represented by $\hat{\alpha}$, $\hat{\beta}$, and $\hat{\gamma}$ unit vectors for representing electric field components. notice that $\hat{\alpha}$ is depend on the location (α, β, γ) which make this grid unstructured. By inspection of the geometry, one can write equations 3.49a, 3.49b, and 3.49c to express E_x, E_y, and E_z in terms of E_α, E_β, and E_γ.

$$E_x(x, y, z) = E_\alpha(\alpha, \beta, \gamma) \cos \Omega_{\alpha,\beta,\gamma} \tag{3.49a}$$

$$E_y(x, y, z) = E_\beta(\alpha, \beta, \gamma) - E_\alpha(\alpha, \beta, \gamma) \sin \Omega_{\alpha,\beta,\gamma} \tag{3.49b}$$

$$E_z(x, y, z) = E_\gamma(\alpha, \beta, \gamma) \tag{3.49c}$$

$$J_x(x, y, z) = J_\alpha(\alpha, \beta, \gamma) \cos \Omega_{\alpha,\beta,\gamma} \tag{3.49d}$$

$$J_y(x, y, z) = J_\beta(\alpha, \beta, \gamma) - J_\alpha(\alpha, \beta, \gamma) \sin \Omega_{\alpha,\beta,\gamma} \tag{3.49e}$$

$$J_z(x, y, z) = J_\gamma(\alpha, \beta, \gamma) \tag{3.49f}$$

In the same way, Let's consider the nonorthogonal coordinate system is represented by $\hat{\alpha}'$, $\hat{\beta}'$, and $\hat{\gamma}'$ unit vectors for representing magnetic field components. Using the same procedure, by which the electric field component was determined, one

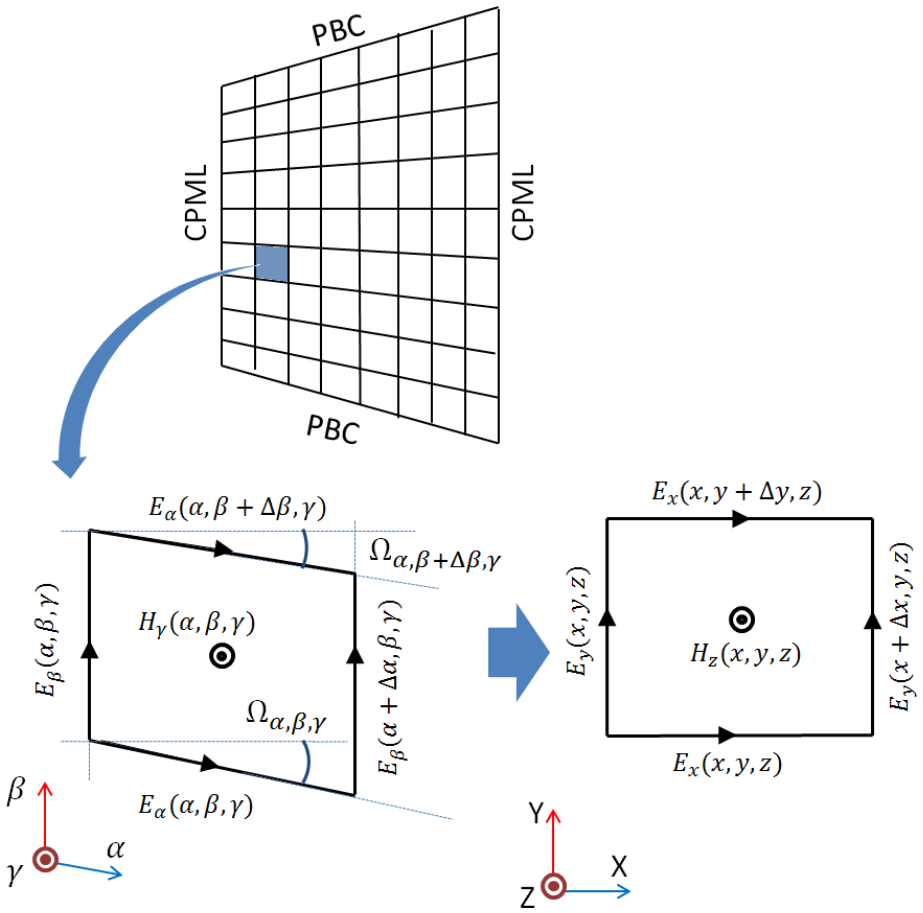

FIGURE 3.5: Illustration of the process of transforming nonorthogonal grid electric field into orthogonal grid electric field.

can write equations 3.50a, 3.50b, and 3.50c to express E_x, E_y, and E_z in terms of $E_{\alpha'}$, $E_{\beta'}$, and $E_{\gamma'}$ (Figure 3.6).

$$H_x(x,y,z) = H_{\alpha'}(\alpha',\beta',\gamma') + H_{\beta'}(\alpha',\beta',\gamma')\sin\Omega_{\alpha',\beta',\gamma'} \tag{3.50a}$$

$$H_y(x,y,z) = H_{\beta'}(\alpha',\beta',\gamma')\cos\Omega_{\alpha',\beta',\gamma'} \tag{3.50b}$$

$$H_z(x,y,z) = H_{\gamma'}(\alpha',\beta',\gamma') \tag{3.50c}$$

$$M_x(x,y,z) = M_{\alpha'}(\alpha',\beta',\gamma') + M_{\beta'}(\alpha',\beta',\gamma')\sin\Omega_{\alpha',\beta',\gamma'} \tag{3.50d}$$

$$M_y(x,y,z) = M_{\beta'}(\alpha',\beta',\gamma')\cos\Omega_{\alpha',\beta',\gamma'} \tag{3.50e}$$

$$M_z(x,y,z) = M_{\gamma'}(\alpha',\beta',\gamma') \tag{3.50f}$$

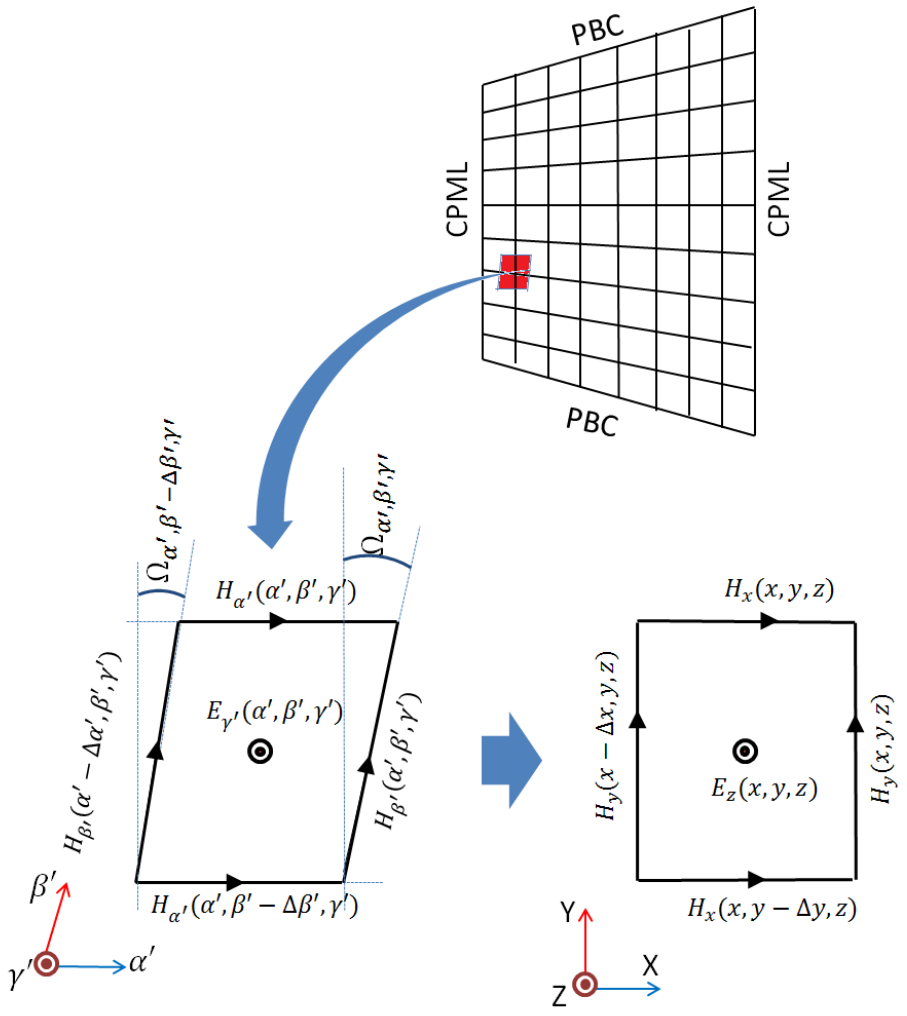

FIGURE 3.6: Illustration of the process of transforming nonorthogonal grid magnetic field into orthogonal grid magnetic field.

Let's consider $\Omega_{\alpha,\beta,\gamma}$ and $\Omega_{\alpha',\beta',\gamma'}$ are measured with reference to the blue colored dashed line and they are positive in clockwise direction. Notice that $\Omega_{\alpha,\beta,\gamma}$ and $\Omega_{\alpha',\beta',\gamma'}$ are depend on only β and β' spacial parameters respectively. So below relations (equations 3.51a, 3.51b, 3.51c, and 3.51d) are valid in this geometry.

$$\Omega_{\alpha,\beta,\gamma} = \Omega_{\alpha,\beta+\Delta\beta,\gamma} \tag{3.51a}$$

$$\Omega_{\alpha',\beta',\gamma'} = \Omega_{\alpha',\beta'+\Delta\beta',\gamma'} \tag{3.51b}$$

$$\Omega_{\alpha,\beta,\gamma} = \Omega_{\alpha+\Delta_\alpha,\beta,\gamma} = \Omega_{\alpha,\beta,\gamma+\Delta\gamma} \tag{3.51c}$$

$$\Omega_{\alpha',\beta',\gamma'} = \Omega_{\alpha'+\Delta\alpha',\beta',\gamma'} = \Omega_{\alpha',\beta',\gamma'+\Delta\gamma'} \tag{3.51d}$$

In addition to that one can simplify the problem by observing equality between $\Omega_{\alpha,\beta,\gamma}$ and $\Omega_{\alpha',\beta',\gamma'}$ in both sign and magnitude. Equation 3.52 can express all the simplification made using the geometry of this grid.

$$\Omega_\beta = \Omega_{\alpha,\beta,\gamma} = \Omega_{\alpha',\beta',\gamma'} = \Omega_{\beta'} \tag{3.52}$$

So in the transformed equations, Ω_β is used for representing angles at each β and β' locations. If the number of element in one ring of the cylindrical array ie N_E and the number of Yee cells in $\hat{\beta}$ direction is N_β Ω_β can be calculated using N_E and N_β as in equation 3.53.

$$\Omega_\beta = \frac{2\pi}{N_\beta N_E} \tag{3.53}$$

FDTD updating equation for determining E_α^{n+1} in terms of E_α^n, $H_{\beta'}^{n-\frac{1}{2}}$, $H_{\beta'}^{n+\frac{1}{2}}$, $H_{\gamma'}^{n-\frac{1}{2}}$, and $H_{\gamma'}^{n+\frac{1}{2}}$ can be obtained, by plugging in E_x, E_y, and E_z from equations 3.49a, 3.50b, and 3.50c in FDTD updating equation A.1.

$$\begin{aligned}
E_\alpha^{n+1}(i_\alpha, i_\beta, i_\gamma) &= C_{ea}(i_\alpha, i_\beta, i_\gamma) \times E_\alpha^n(i_\alpha, i_\beta, i_\gamma) \\
&+ \frac{C_{eb}(i_{\alpha'}, i_{\beta'}, i_{\gamma'}) \sec\Omega_\beta}{\Delta\beta} \times \left(H_{\gamma'}^{n+\frac{1}{2}}(i_{\alpha'}, i_{\beta'}, i_{\gamma'}) - H_{\gamma'}^{n+\frac{1}{2}}(i_{\alpha'}, i_{\beta'}-1, i_{\gamma'})\right) \\
&- \frac{C_{eb}(i_{\alpha'}, i_{\beta'}, i_{\gamma'})}{\Delta\gamma} \times \left(H_{\beta'}^{n+\frac{1}{2}}(i_{\alpha'}, i_{\beta'}, i_{\gamma'}) - H_{\beta'}^{n+\frac{1}{2}}(i_{\alpha'}, i_{\beta'}, i_{\gamma'}-1)\right) \\
&- C_{eb}(i_{\alpha'}, i_{\beta'}, i_{\gamma'}) \times J_\alpha^{n+\frac{1}{2}}(i_\alpha, i_\beta, i_\gamma)
\end{aligned} \tag{3.54}$$

The updating coefficients $C_{ea}(i_\alpha, i_\beta, i_\gamma)$ and $C_{eb}(i_{\alpha'}, i_{\beta'}, i_{\gamma'})$ can be derived from the updating coefficients of rectangular case (Appendix A).

$$C_{ea}(i_\alpha, i_\beta, i_\gamma) = \left(\frac{2\epsilon(i_\alpha, i_\beta, i_\gamma) - \sigma^e(i_\alpha, i_\beta, i_\gamma)\Delta_t}{2\epsilon(i_\alpha, i_\beta, i_\gamma) + \sigma^e(i_\alpha, i_\beta, i_\gamma)\Delta_t}\right) \tag{3.55a}$$

$$C_{eb}(i_{\alpha'}, i_{\beta'}, i_{\gamma'}) = \left(\frac{2\Delta_t}{2\epsilon(i_{\alpha'}, i_{\beta'}, i_{\gamma'}) + \sigma^e(i_{\alpha'}, i_{\beta'}, i_{\gamma'})\Delta_t} \right) \tag{3.55b}$$

FDTD updating equation for determining E_β^{n+1} in terms of E_β^n, E_α^{n+1}, E_α^n, $H_{\alpha'}^{n-\frac{1}{2}}$, $H_{\alpha'}^{n+\frac{1}{2}}$, $H_{\gamma'}^{n-\frac{1}{2}}$, and $H_{\gamma'}^{n+\frac{1}{2}}$ can be obtained, by plugging in E_x, E_y, and E_z from equations 3.49b, 3.50a, and 3.50c in FDTD updating equation A.3.

$$\begin{aligned}
E_\beta^{n+1}(i_\alpha, i_\beta, i_\gamma) &= C_{ea}(i_\alpha, i_\beta, i_\gamma) \times E_\beta^n(i_\alpha, i_\beta, i_\gamma) \\
&- C_{ea}(i_\alpha, i_\beta, i_\gamma) \sin\Omega_\beta \times E_\alpha^n(i_\alpha, i_\beta, i_\gamma) + \sin\Omega_\beta \times E_\alpha^{n+1}(i_\alpha, i_\beta, i_\gamma) \\
&+ \frac{C_{eb}(i_{\alpha'}, i_{\beta'}, i_{\gamma'})}{\Delta\beta} \times \left(H_{\alpha'}^{n+\frac{1}{2}}(i_{\alpha'}, i_{\beta'}, i_{\gamma'}) - H_{\alpha'}^{n+\frac{1}{2}}(i_{\alpha'}, i_{\beta'}, i_{\gamma'} - 1) \right) \\
&+ \frac{C_{eb}(i_{\alpha'}, i_{\beta'}, i_{\gamma'}) \sin\Omega_\beta}{\Delta\beta} \times \left(H_{\beta'}^{n+\frac{1}{2}}(i_{\alpha'}, i_{\beta'}, i_{\gamma'}) - H_{\beta'}^{n+\frac{1}{2}}(i_{\alpha'}, i_{\beta'}, i_{\gamma'} - 1) \right) \\
&- \frac{C_{eb}(i_{\alpha'}, i_{\beta'}, i_{\gamma'})}{\Delta\gamma} \times \left(H_{\gamma'}^{n+\frac{1}{2}}(i_{\alpha'}, i_{\beta'}, i_{\gamma'}) - H_{\gamma'}^{n+\frac{1}{2}}(i_{\alpha'} - 1, i_{\beta'}, i_{\gamma'}) \right) \\
&- C_{eb}(i_{\alpha'}, i_{\beta'}, i_{\gamma'}) \times J_\beta^{n+\frac{1}{2}}(i_\alpha, i_\beta, i_\gamma) \\
&+ C_{eb}(i_{\alpha'}, i_{\beta'}, i_{\gamma'}) \sin\Omega_\beta \times J_\alpha^{n+\frac{1}{2}}(i_\alpha, i_\beta, i_\gamma)
\end{aligned} \tag{3.56}$$

FDTD updating equation for determining E_γ^{n+1} in terms of E_γ^n, $H_{\alpha'}^{n-\frac{1}{2}}$, $H_{\alpha'}^{n+\frac{1}{2}}$, $H_{\beta'}^{n-\frac{1}{2}}$, and $H_{\beta'}^{n+\frac{1}{2}}$ can be obtained, by plugging in H_x, H_y, and E_z from equations 3.50a, 3.50b, and 3.49c in FDTD updating equation A.5.

$$\begin{aligned}
E_\gamma^{n+1}(i_\alpha, i_\beta, i_\gamma) &= C_{ea}(i_\alpha, i_\beta, i_\gamma) \times E_\gamma^n(i_\alpha, i_\beta, i_\gamma) \\
&+ \frac{C_{eb}(i_{\alpha'}, i_{\beta'}, i_{\gamma'}) \cos\Omega_\beta}{\Delta\beta} \times \left(H_{\beta'}^{n+\frac{1}{2}}(i_{\alpha'}, i_{\beta'}, i_{\gamma'}) - H_{\beta'}^{n+\frac{1}{2}}(i_{\alpha'} - 1, i_{\beta'}, i_{\gamma'}) \right) \\
&- \frac{C_{eb}(i_{\alpha'}, i_{\beta'}, i_{\gamma'})}{\Delta\gamma} \times \left(H_{\alpha'}^{n+\frac{1}{2}}(i_{\alpha'}, i_{\beta'}, i_{\gamma'}) - H_{\alpha'}^{n+\frac{1}{2}}(i_{\alpha'}, i_{\beta'} - 1, i_{\gamma'}) \right) \\
&- \frac{C_{eb}(i_{\alpha'}, i_{\beta'}, i_{\gamma'}) \sin\Omega_\beta}{\Delta\gamma} \times \left(H_{\beta'}^{n+\frac{1}{2}}(i_{\alpha'}, i_{\beta'}, i_{\gamma'}) - H_{\beta'}^{n+\frac{1}{2}}(i_{\alpha'}, i_{\beta'} - 1, i_{\gamma'}) \right) \\
&- C_{eb}(i_{\alpha'}, i_{\beta'}, i_{\gamma'}) \times J_\gamma^{n+\frac{1}{2}}(i_\alpha, i_\beta, i_\gamma)
\end{aligned} \tag{3.57}$$

FDTD updating equation for determining $H_{\alpha'}^{n+\frac{1}{2}}$ in terms of $H_{\alpha'}^{n-\frac{1}{2}}$, $H_{\beta'}^{n-\frac{1}{2}}$, $H_{\beta'}^{n+\frac{1}{2}}$, E_{β}^{n}, E_{α}^{n}, E_{γ}^{n}, $M_{\alpha'}^{n}$, and $M_{\beta'}^{n}$ can be obtained, by plugging in H_x, E_y, E_z and M_x from equations 3.50a, 3.49b, 3.49c, and 3.50f in FDTD updating equation A.7. Notice the present value of magnetic field component in $\hat{\beta}'$ ($H_{\beta'}^{n+\frac{1}{2}}$) is required to calculate the present magnetic field component in $\hat{\alpha}'$ direction. So in the computer program, $H_{\beta'}^{n+\frac{1}{2}}$ should be computed before computing $H_{\alpha'}^{n+\frac{1}{2}}$.

$$
\begin{aligned}
H_{\alpha'}^{n+\frac{1}{2}}(i_{\alpha'}, i_{\beta'}, i_{\gamma'}) &= C_{ha}(i_{\alpha'}, i_{\beta'}, i_{\gamma'}) \times H_{\alpha'}^{n-\frac{1}{2}}(i_{\alpha'}, i_{\beta'}, i_{\gamma'}) \\
&+ \Big(C_{ha}(i_{\alpha'}, i_{\beta'}, i_{\gamma'}) \times H_{\beta'}^{n-\frac{1}{2}}(i_{\alpha'}, i_{\beta'}, i_{\gamma'}) - H_{\beta'}^{n+\frac{1}{2}}(i_{\alpha'}, i_{\beta'}, i_{\gamma'}) \Big) \sin\Omega_{\beta} \\
&+ \frac{C_{hb}(i_{\alpha}, i_{\beta}, i_{\gamma})}{\Delta\beta} \times \big(E_{\beta}^{n}(i_{\alpha}, i_{\beta}, i_{\gamma}+1) - E_{\beta}^{n}(i_{\alpha}, i_{\beta}, i_{\gamma}) \big) \\
&- \frac{C_{hb}(i_{\alpha}, i_{\beta}, i_{\gamma}) \sin\Omega_{\beta}}{\Delta\beta} \times \big(E_{\alpha}^{n}(i_{\alpha}, i_{\beta}, i_{\gamma}+1) - E_{\alpha}^{n}(i_{\alpha}, i_{\beta}, i_{\gamma}) \big) \\
&- \frac{C_{hb}(i_{\alpha}, i_{\beta}, i_{\gamma})}{\Delta\gamma} \times \big(E_{\gamma}^{n}(i_{\alpha}, i_{\beta}+1, i_{\gamma}) - E_{\gamma}^{n}(i_{\alpha}, i_{\beta}, i_{\gamma}) \big) \\
&- C_{hb}(i_{\alpha}, i_{\beta}, i_{\gamma}) \times M_{\alpha'}^{n}(i_{\alpha'}, i_{\beta'}, i_{\gamma'}) \\
&- C_{hb}(i_{\alpha}, i_{\beta}, i_{\gamma}) \sin\Omega_{\beta} \times M_{\beta'}^{n}(i_{\alpha'}, i_{\beta'}, i_{\gamma'})
\end{aligned}
\tag{3.58}
$$

The updating coefficients $C_{ha}(i_{\alpha'}, i_{\beta'}, i_{\gamma'})$ and $C_{hb}(i_{\alpha}, i_{\beta}, i_{\gamma})$ can be derived from the updating coefficients of rectangular case (Appendix A).

$$
C_{ha}(i_{\alpha'}, i_{\beta'}, i_{\gamma'}) = \left(\frac{2\mu(i_{\alpha}, i_{\beta}, i_{\gamma}) - \sigma^{m}(i_{\alpha}, i_{\beta}, i_{\gamma})\Delta_t}{2\mu(i_{\alpha}, i_{\beta}, i_{\gamma}) + \sigma^{m}(i_{\alpha}, i_{\beta}, i_{\gamma})\Delta_t} \right) \tag{3.59a}
$$

$$
C_{hb}(i_{\alpha}, i_{\beta}, i_{\gamma}) = \left(\frac{2\Delta_t}{2\mu(i_{\alpha'}, i_{\beta'}, i_{\gamma'}) + \sigma^{m}(i_{\alpha'}, i_{\beta'}, i_{\gamma'})\Delta_t} \right) \tag{3.59b}
$$

FDTD updating equation for determining E_{β}^{n+1} in terms of E_{β}^{n}, E_{α}^{n+1}, E_{α}^{n}, $H_{\alpha'}^{n-\frac{1}{2}}$, $H_{\alpha'}^{n+\frac{1}{2}}$, $H_{\gamma'}^{n-\frac{1}{2}}$, and $H_{\gamma'}^{n+\frac{1}{2}}$ can be obtained, by plugging in E_x, E_y, and E_z from equations 3.49b, 3.50a, and 3.50c in FDTD updating equation A.9.

$$
\begin{aligned}
H_{\beta'}^{n+\frac{1}{2}}(i_{\alpha'}, i_{\beta'}, i_{\gamma'}) &= C_{ha}(i_{\alpha'}, i_{\beta'}, i_{\gamma'}) \times H_{\beta'}^{n-\frac{1}{2}}(i_{\alpha'}, i_{\beta'}, i_{\gamma'}) \\
&+ \frac{C_{hb}(i_\alpha, i_\beta, i_\gamma)\sec\Omega_\beta}{\Delta\beta} \times \left(E_\gamma^n(i_\alpha, i_\beta, i_\gamma + 1) - E_\gamma^n(i_\alpha, i_\beta, i_\gamma)\right) \\
&- \frac{C_{hb}(i_\alpha, i_\beta, i_\gamma)}{\Delta\gamma} \times \left(E_\alpha^n(i_\alpha, i_\beta + 1, i_\gamma) - E_\alpha^n(i_\alpha, i_\beta, i_\gamma)\right) \\
&- C_{hb}(i_\alpha, i_\beta, i_\gamma) \times M_\beta^n(i_{\alpha'}, i_{\beta'}, i_{\gamma'})
\end{aligned}
\tag{3.60}
$$

FDTD updating equation for determining E_γ^{n+1} in terms of E_γ^n, $H_{\alpha'}^{n-\frac{1}{2}}$, $H_{\alpha'}^{n+\frac{1}{2}}$, $H_{\beta'}^{n-\frac{1}{2}}$, and $H_{\beta'}^{n+\frac{1}{2}}$ can be obtained, by plugging in H_x, H_y, and E_z from equations 3.50a, 3.50b, and 3.49c in FDTD updating equation A.11.

$$
\begin{aligned}
H_{\gamma'}^{n+\frac{1}{2}}(i_{\alpha'}, i_{\beta'}, i_{\gamma'}) &= C_{ha}(i_{\alpha'}, i_{\beta'}, i_{\gamma'}) \times H_{\gamma'}^{n-\frac{1}{2}}(i_{\alpha'}, i_{\beta'}, i_{\gamma'}) \\
&+ \frac{C_{hb}(i_\alpha, i_\beta, i_\gamma)\cos\Omega_\beta}{\Delta\beta} \times \left(E_\alpha^n(i_\alpha, i_\beta + 1, i_\gamma) - E_\alpha^n(i_\alpha, i_\beta, i_\gamma)\right) \\
&- \frac{C_{hb}(i_\alpha, i_\beta, i_\gamma)}{\Delta\gamma} \times \left(E_\beta^n(i_\alpha + 1, i_\beta, i_\gamma) - E_\beta^n(i_\alpha, i_\beta, i_\gamma)\right) \\
&+ \frac{C_{hb}(i_\alpha, i_\beta, i_\gamma)\sin\Omega_\beta}{\Delta\gamma} \times \left(E_\alpha^n(i_\alpha + 1, i_\beta, i_\gamma) - E_\alpha^n(i_\alpha, i_\beta, i_\gamma)\right) \\
&- C_{hb}(i_\alpha, i_\beta, i_\gamma) \times M_\alpha^n(i_{\alpha'}, i_{\beta'}, i_{\gamma'})
\end{aligned}
\tag{3.61}
$$

3.3.2 Numerical Stability

According to the Jin-Fa Lee's paper [93], the stability criteria for generalized grid can be written in terms of the dot products of dual or reciprocal basis which can be derived from the unit vectors of each electric field component's directions ($\hat{\alpha}$, $\hat{\beta}$, and $\hat{\gamma}$ coordinate system). Let's define the reciprocal bases as $\hat{A_\alpha}$, $\hat{A_\beta}$, and $\hat{A_\gamma}$.

$$
\hat{A_\alpha} = \frac{\hat{\beta} \times \hat{\gamma}}{\hat{\alpha} \cdot \hat{\beta} \times \hat{\gamma}} = \frac{\hat{\beta} \times \hat{\gamma}}{\Delta_\alpha \Delta_\beta \Delta_\gamma \cos\Omega_\beta} \tag{3.62a}
$$

$$
\hat{A_\beta} = \frac{\hat{\gamma} \times \hat{\alpha}}{\hat{\beta} \cdot \hat{\gamma} \times \hat{\alpha}} = \frac{\hat{\gamma} \times \hat{\alpha}}{\Delta_\alpha \Delta_\beta \Delta_\gamma \cos\Omega_\beta} \tag{3.62b}
$$

$$\hat{A}_\gamma = \frac{\hat{\alpha} \times \hat{\beta}}{\hat{\gamma} \cdot \hat{\alpha} \times \hat{\beta}} = \frac{\hat{\alpha} \times \hat{\beta}}{\Delta_\alpha \Delta_\beta \Delta_\gamma \cos \Omega_\beta} \tag{3.62c}$$

The same inequality can be derived using $\hat{\alpha'}$, $\hat{\beta'}$, and $\hat{\gamma'}$ coordinate system. The equation 3.63 is the the stability criteria for generalized FDTD equation as explained in [93].

$$\Delta t \leqslant \frac{1}{c\sqrt{\sum\limits_{p,q \in \alpha, i_\beta, \gamma} \hat{A}_p \cdot \hat{A}_q}} \tag{3.63}$$

By substituting the unit vectors in equation 3.63, one can deduce the inequation 3.64.

$$\Delta t \leqslant \frac{1}{c\sqrt{\frac{1}{(\Delta_\alpha)^2} + \frac{1}{(\Delta_\beta)^2} + \frac{1}{(\Delta_\gamma)^2} - \frac{2\sin\Omega_\beta}{\Delta_\alpha \Delta_\beta}}} \tag{3.64}$$

This inequality is the CFL limit for this particulate geometry. Notice there is an another criteria for Ω_β, since time step size Δ_t should be a real value. Analysis of that requirement will lead to the minimum number of element that can be in a circular ring of the cylinder. The minimum number of elements will not guarantee the stability but required to construct the model.

$$\frac{1}{(\Delta_\alpha)^2} + \frac{1}{(\Delta_\beta)^2} + \frac{1}{(\Delta_\gamma)^2} > \frac{2\sin\Omega_\beta}{\Delta_\alpha \Delta_\beta} \tag{3.65}$$

$$\Omega_\beta < \arcsin\left(\frac{\Delta_\beta}{2\Delta_\alpha} + \frac{\Delta_\alpha}{2\Delta_\beta} + \frac{\Delta_\alpha \Delta_\beta}{2(\Delta_\gamma)^2}\right) < \frac{\pi}{2} \tag{3.66}$$

Then the maximum value of Ω_β is depend on the selection of Δ_α, Δ_β, and Δ_γ. From the geometry of faceted-cylindrical array, one can write the range of Ω_β in terms of the number of elements (N_e) in one ring of the array.

$$-\frac{\pi}{N_e} < \Omega_\beta < \frac{\pi}{N_e} \tag{3.67}$$

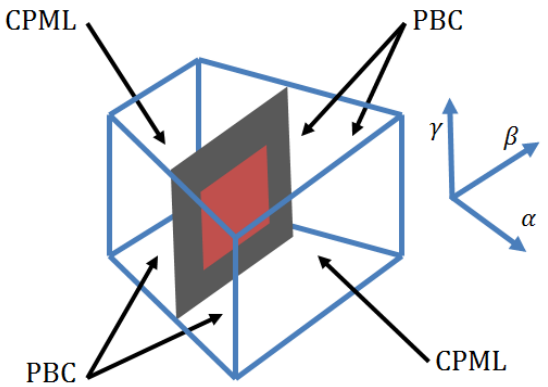

FIGURE 3.7: Unit cell for FDTD simulation for faceted-cylindrical array.

3.3.3 Periodic Boundary Condition

In figure 3.7, a unit cell in unstructured nonorthogonal coordinates is illustrated with PBCs and CPMLs. This model is unitized to simulate an active element of a *faceted-cylindrical array*, which is the manifold structure used in the testbed under measurement as shown in figure 4.9. The PBC for planar array unit cell can be adapted for simulate antenna element with PBC for this kind array using updating equations for a nonorthogonal grid. Since the nonorthogonality happens to appeared only in a two-dimensional plane, a modified equation from rectangular grid model is used. The key idea of formulating the proper projection scheme is the very nature of this geometry of the unit cell of the faceted-cylindrical array. The equations to calculate the field components in $\widehat{y}$ direction can be used without any alteration. The field components in $\widehat{x}$ and $\widehat{z}$ direction have to be computed with irregular non-orthogonal structured grid [80].

3.3.3.1 Periodicity in $\hat{\gamma}$ Direction

The equation (3.68) is for calculating the field components E_β at the lower bound of γ ($i_\gamma = 1$). The field components $E_\beta^{n+1}(i_\alpha, i_\beta, 1)$ is computed using $E_\beta^n(i_\alpha, i_\beta, 1)$ and magnetic field components in $\widehat{\alpha}$, $\widehat{\beta}$, and $\widehat{\gamma}$ directions, which are $H_{\alpha'}^{n+\frac{1}{2}}(i_{\alpha'}, i_{\beta'}, 1)$, $H_{\alpha'}^{n+\frac{1}{2}}(i_{\alpha'}, i_{\beta'}, \nexists)$, $H_{\beta'}^{n+\frac{1}{2}}(i_{\alpha'}, i_{\beta'}, 1)$, $H_{\beta'}^{n+\frac{1}{2}}(i_{\alpha'}, i_{\beta'}, \nexists)$, $H_{\gamma'}^{n+\frac{1}{2}}(i_{\alpha'}, i_{\beta'}, 1)$, and $H_{\gamma'}^{n+\frac{1}{2}}(i_{\alpha'}-$

$1, i_{\beta'}, 1)$. The updating coefficients $C_{ea}(i_\alpha, i_\beta, 1)$ and $C_{eb}(i_{\alpha'}, i_{\beta'}, 1)$ of the equation 3.68 can be computed using equation 3.55.

$$\begin{aligned} E_\beta^{n+1}(i_\alpha, i_\beta, 1) &= C_{ea}(i_\alpha, i_\beta, 1) \times E_\beta^n(i_\alpha, i_\beta, 1) \\ &- C_{ea}(i_\alpha, i_\beta, 1)\sin\Omega_\beta \times E_\alpha^n(i_\alpha, i_\beta, 1) + \sin\Omega_\beta \times E_\alpha^{n+1}(i_\alpha, i_\beta, 1) \\ &+ \frac{C_{eb}(i_{\alpha'}, i_{\beta'}, 1)}{\Delta\beta} \times \left(H_{\alpha'}^{n+\frac{1}{2}}(i_{\alpha'}, i_{\beta'}, 1) - H_{\alpha'}^{n+\frac{1}{2}}(i_{\alpha'}, i_{\beta'}, \nexists)\right) \\ &+ \frac{C_{eb}(i_{\alpha'}, i_{\beta'}, 1)\sin\Omega_\beta}{\Delta\beta} \times \left(H_{\beta'}^{n+\frac{1}{2}}(i_{\alpha'}, i_{\beta'}, 1) - H_{\beta'}^{n+\frac{1}{2}}(i_{\alpha'}, i_{\beta'}, \nexists)\right) \\ &- \frac{C_{eb}(i_{\alpha'}, i_{\beta'}, 1)}{\Delta\gamma} \times \left(H_{\gamma'}^{n+\frac{1}{2}}(i_{\alpha'}, i_{\beta'}, 1) - H_{\gamma'}^{n+\frac{1}{2}}(i_{\alpha'} - 1, i_{\beta'}, 1)\right) \end{aligned} \tag{3.68}$$

The magnetic field components $H_{\alpha'}^{n+\frac{1}{2}}(i_{\alpha'}, i_{\beta'}, \nexists)$ and $H_{\beta'}^{n+\frac{1}{2}}(i_{\alpha'}, i_{\beta'}, \nexists)$ do not exist in the problem space. Using the Floquet theory, $H_{\alpha'}^{n+\frac{1}{2}}(i_{\alpha'}, i_{\beta'}, \nexists)$ and $H_{\beta'}^{n+\frac{1}{2}}(i_{\alpha'}, i_{\beta'}, \nexists)$ can be calculated as in equation 3.69a and 3.69b. k_β is the wave number in $\hat{\beta}$ direction and can be computed as $k_{\gamma'} = \frac{\omega}{c}\sin\varpi_{\gamma'}$ ($\varpi_{\gamma'}$ is the incident angle of the wave to $\hat{\beta}$ direction)

$$H_{\alpha'}^{n+\frac{1}{2}}(i_{\alpha'}, i_{\beta'}, \nexists) = H_{\alpha'}^{n+\frac{1}{2}}(i_{\alpha'}, i_{\beta'}, 1)e^{jk_{\gamma'}N_{\gamma'}\Delta_{\gamma'}} \tag{3.69a}$$

$$H_{\beta'}^{n+\frac{1}{2}}(i_{\alpha'}, i_{\beta'}, \nexists) = H_{\beta'}^{n+\frac{1}{2}}(i_{\alpha'}, i_{\beta'}, 1)e^{jk_{\gamma'}N_{\gamma'}\Delta_{\gamma'}} \tag{3.69b}$$

Using the Floquet theory, $E_\alpha^{n+1}(i_\alpha, i_\beta, N_\gamma{+}1)$ can be computed using $E_\alpha^{n+1}(i_\alpha, i_\beta, 1)$ as equation 3.70. k_γ is the wave number in $\hat{\gamma}$ direction and can be computed as $k_\gamma = \frac{\omega}{c}\sin\varpi_\gamma$ (ϖ_γ is the incident angle of the wave to $\hat{\gamma}$ direction)

$$E_\beta^{n+1}(i_\alpha, i_\beta, N_\gamma + 1) = E_\beta^{n+1}(i_\alpha, i_\beta, 1)e^{-jk_\gamma N_\gamma \Delta_\gamma} \tag{3.70}$$

The equation (3.71) is for calculating the E_α field component at the lower bound of γ ($i_\gamma = 1$). The field component $E_\alpha^{n+1}(i_\alpha, i_\beta, 1)$ is computed using $E_\alpha^n(i_\alpha, i_\beta, 1)$ and magnetic field components in γ and β directions, which are $H_{\gamma'}^{n+\frac{1}{2}}(i_{\alpha'}, i_{\beta'}, 1)$,

$H_{\gamma'}^{n+\frac{1}{2}}(i_{\alpha'}, i_{\beta'}-1, 1)$, $H_{\beta'}^{n+\frac{1}{2}}(i_{\alpha'}, i_{\beta'}, 1)$, and $H_{\beta'}^{n+\frac{1}{2}}(i_{\alpha'}, i_{\beta'}, \nexists)$. The updating coefficients $C_{eb}(i_\alpha, i_\beta, 1)$, and $C_{eb}(i_\alpha, i_\beta, 1)$ of the equation 3.71 can be computed using equation 3.55.

$$\begin{aligned} E_\alpha^{n+1}(i_\alpha, i_\beta, 1) &= C_{ea}(i_\alpha, i_\beta, 1) \times E_\alpha^n(i_\alpha, i_\beta, 1) \\ &+ \frac{C_{eb}(i_{\alpha'}, i_{\beta'}, 1)\sec\Omega_\beta}{\Delta\beta} \times \left(H_{\gamma'}^{n+\frac{1}{2}}(i_{\alpha'}, i_{\beta'}, 1) - H_{\gamma'}^{n+\frac{1}{2}}(i_{\alpha'}, i_{\beta'}-1, 1)\right) \\ &- \frac{C_{eb}(i_{\alpha'}, i_{\beta'}, 1)}{\Delta\gamma} \times \left(H_{\beta'}^{n+\frac{1}{2}}(i_{\alpha'}, i_{\beta'}, 1) - H_{\beta'}^{n+\frac{1}{2}}(i_{\alpha'}, i_{\beta'}, \nexists)\right) \end{aligned} \tag{3.71}$$

The magnetic field component $H_{\beta'}^{n+\frac{1}{2}}(i_{\alpha'}, i_{\beta'}, \nexists)$ does not exist in the problem space. Using the Floquet theory $H_{\beta'}^{n+\frac{1}{2}}(i_{\alpha'}, i_{\beta'}, \nexists)$ can be calculated as in equation 3.72.

$$H_{\beta'}^{n+\frac{1}{2}}(i_{\alpha'}, i_{\beta'}, \nexists) = H_{\beta'}^{n+\frac{1}{2}}(i_{\alpha'}, i_{\beta'}, 1)e^{jk_\gamma N_\gamma \Delta_\gamma} \tag{3.72}$$

Using the Floquet theory, $E_\alpha^{n+1}(i_\alpha, i_\beta, N_\gamma{+}1)$ can be computed using $E_\alpha^{n+1}(i_\alpha, i_\beta, 1)$ as equation 3.73.

$$E_\alpha^{n+1}(i_\alpha, i_\beta, N_z+1) = E_\alpha^{n+1}(i_\alpha, i_\beta, 1)e^{-jk_\gamma N_\gamma \Delta_\gamma} \tag{3.73}$$

3.3.3.2 Periodicity in $\hat{\beta}$ Direction

The equation (3.74) is for calculating the E_γ field components at the lower bound of β ($i_\beta = 1$). The field components $E_\gamma^{n+1}(i_\alpha, 1, i_\gamma)$ is computed using $E_\gamma^n(i_\alpha, 1, i_\gamma)$ and magnetic field components in $\hat{\beta}$ and $\hat{\alpha}$ directions, which are $H_{\beta'}^{n+\frac{1}{2}}(i_{\alpha'}, 1, i_{\gamma'})$, $H_{\beta'}^{n+\frac{1}{2}}(i_{\alpha'}-1, 1, i_{\gamma'})$, $H_{\alpha'}^{n+\frac{1}{2}}(i_{\alpha'}, 1, i_{\gamma'})$, $H_{\alpha'}^{n+\frac{1}{2}}(i_{\alpha'}, \nexists, i_{\gamma'})$, $H_{\beta'}^{n+\frac{1}{2}}(i_{\alpha'}, 1, i_{\gamma'})$, and $H_{\beta'}^{n+\frac{1}{2}}(i_{\alpha'}, \nexists, i_{\gamma'})$. The updating coefficients of the equation (3.74) $C_{ea}(i_\alpha, 1, i_\gamma)$ and $C_{eb}(i_{\alpha'}, 1, i_{\gamma'})$ can be computed using equation 3.55.

$$
\begin{aligned}
E_{\gamma}^{n+1}(i_\alpha, 1, i_\gamma) &= C_{ea}(i_\alpha, i_\beta, i_\gamma) \times E_{\gamma}^{n}(i_\alpha, 1, i_\gamma) \\
&+ \frac{C_{eb}(i_{\alpha'}, 1, i_{\gamma'}) \cos\Omega_\beta}{\Delta\beta} \times \left(H_{\beta'}^{n+\frac{1}{2}}(i_{\alpha'}, 1, i_{\gamma'}) - H_{\beta'}^{n+\frac{1}{2}}(i_{\alpha'} - 1, 1, i_{\gamma'}) \right) \\
&- \frac{C_{eb}(i_{\alpha'}, 1, i_{\gamma'})}{\Delta\gamma} \times \left(H_{\alpha'}^{n+\frac{1}{2}}(i_{\alpha'}, 1, i_{\gamma'}) - H_{\alpha'}^{n+\frac{1}{2}}(i_{\alpha'}, \nexists, i_{\gamma'}) \right) \\
&- \frac{C_{eb}(i_{\alpha'}, 1, i_{\gamma'}) \sin\Omega_\beta}{\Delta\gamma} \times \left(H_{\beta'}^{n+\frac{1}{2}}(i_{\alpha'}, 1, i_{\gamma'}) - H_{\beta'}^{n+\frac{1}{2}}(i_{\alpha'}, \nexists, i_{\gamma'}) \right)
\end{aligned}
\tag{3.74}
$$

The magnetic field components $H_{\alpha'}^{n+\frac{1}{2}}(i_{\alpha'}, \nexists, i_{\gamma'})$ and $H_{\beta'}^{n+\frac{1}{2}}(i_{\alpha'}, \nexists, i_{\gamma'})$ do not exist in the problem space. Using the Floquet theory $H_{\alpha'}^{n+\frac{1}{2}}(i_{\alpha'}, \nexists, i_{\gamma'})$ and $H_{\beta'}^{n+\frac{1}{2}}(i_{\alpha'}, \nexists, i_{\gamma'})$ can be calculated as in equation 3.75 and 3.76. $k_{\beta'}$ is the wave number in $\hat{\beta}'$ direction and can be computed as $k_{\beta'} = \frac{\omega}{c}\sin\varpi_{\beta'}$ ($\varpi_{\beta'}$ is the incident angle of the wave to $\hat{\beta}'$ direction)

$$
H_{\alpha'}^{n+\frac{1}{2}}(i_{\alpha'}, \nexists, i_{\gamma'}) = H_{\alpha'}^{n+\frac{1}{2}}(i_{\alpha'}, 1, i_{\gamma'}) e^{jk_{\beta'}N_{\beta'}\Delta_{\beta'}} \tag{3.75}
$$

$$
H_{\beta'}^{n+\frac{1}{2}}(i_{\alpha'}, \nexists, i_{\gamma'}) = H_{\beta'}^{n+\frac{1}{2}}(i_{\alpha'}, 1, i_{\gamma'}) e^{jk_{\beta'}N_{\beta'}\Delta_{\beta'}} \tag{3.76}
$$

$E_{\gamma}^{n+1}(i_\alpha, i_\beta, N_\gamma + 1)$ can be computed using $E_{\gamma}^{n+1}(i_\alpha, i_\beta, 1)$ as equation 3.77. k_β is the wave number in $\hat{\beta}$ direction and can be computed as $k_\beta = \frac{\omega}{c}\sin\varpi_\beta$ (ϖ_β is the incident angle of the wave to $\hat{\beta}$ direction)

$$
E_{\gamma}^{n+1}(i_\alpha, N_\beta + 1, i_\gamma) = E_{\gamma}^{n+1}(i_\alpha, 1, i_\gamma) e^{-jk_\beta N_\beta \Delta_\beta} \tag{3.77}
$$

The equation (3.78) is for calculating the E_α field component at the lower bound of β ($i_\beta = 1$). The field component $E_{\alpha}^{n+1}(i_\alpha, 1, i_\gamma)$ is computed using $E_{\alpha}^{n}(i_\alpha, 1, i_\gamma)$ and magnetic field components in $\hat{\gamma}$ and $\hat{\beta}$ directions, which are $H_{\gamma'}^{n+\frac{1}{2}}(i_{\alpha'}, 1, i_{\gamma'})$, $H_{\gamma'}^{n+\frac{1}{2}}(i_{\alpha'}, \nexists, i_{\gamma'})$, $H_{\beta'}^{n+\frac{1}{2}}(i_{\alpha'}, 1, i_{\gamma'})$, and $H_{\beta'}^{n+\frac{1}{2}}(i_{\alpha'}, 1, i_{\gamma'} - 1)$.

$$
\begin{aligned}
E_{\alpha}^{n+1}(i_{\alpha},1,i_{\gamma}) &= C_{ea}(i_{\alpha},1,i_{\gamma}) \times E_{\alpha}^{n}(i_{\alpha},1,i_{\gamma}) \\
&+ \frac{C_{eb}(i_{\alpha'},1,i_{\gamma'})\sec\Omega_{\beta}}{\Delta\beta} \times \left(H_{\gamma'}^{n+\frac{1}{2}}(i_{\alpha'},1,i_{\gamma'}) - H_{\gamma'}^{n+\frac{1}{2}}(i_{\alpha'},\nexists,i_{\gamma'})\right) \\
&- \frac{C_{eb}(i_{\alpha'},1,i_{\gamma'})}{\Delta\gamma} \times \left(H_{\beta'}^{n+\frac{1}{2}}(i_{\alpha'},1,i_{\gamma'}) - H_{\beta'}^{n+\frac{1}{2}}(i_{\alpha'},1,i_{\gamma'}-1)\right)
\end{aligned} \tag{3.78}
$$

The magnetic field component $H_{\beta'}^{n+\frac{1}{2}}(i_{\alpha'},\nexists,i_{\gamma'})$ does not exist in the problem space. Using the Floquet theory $H_{\beta'}^{n+\frac{1}{2}}(i_{\alpha'},\nexists,i_{\gamma'})$ can be calculated as in equation 3.79.

$$
H_{\gamma'}^{n+\frac{1}{2}}(i_{\alpha'},\nexists,i_{\gamma'}) = H_{\gamma'}^{n+\frac{1}{2}}(i_{\alpha'},N_{\beta'},i_{\gamma'})e^{jk_{\beta'}N_{\beta'}\Delta_{\beta'}} \tag{3.79}
$$

$E_{\alpha}^{n+1}(i_{\alpha},i_{\beta},N_{\gamma}+1)$ can be computed using $E_{\alpha}^{n+1}(i_{\alpha},i_{\beta},1)$ as equation 3.80.

$$
E_{\alpha}^{n+1}(i_{\alpha},N_{\beta}+1,i_{\gamma}) = E_{\alpha}^{n+1}(i_{\alpha},1,i_{\gamma})e^{-jk_{\beta}N_{\beta}\Delta_{\beta}} \tag{3.80}
$$

3.3.3.3 Treatment at the Corners

At the corners of the cell (the FDTD mesh of the patch antenna), E_{α} has to be updated using (3.81), (3.83), (3.84), and (3.85) equation.

$$
\begin{aligned}
E_{\alpha}^{n+1}(i_{\alpha},1,1) &= C_{ea}(i_{\alpha},1,1) \times E_{\alpha}^{n}(i_{\alpha},1,1) \\
&+ \frac{C_{eb}(i_{\alpha'},1,1)\sec\Omega_{\beta}}{\Delta\beta} \times \left(H_{\gamma'}^{n+\frac{1}{2}}(i_{\alpha'},1,1) - H_{\gamma'}^{n+\frac{1}{2}}(i_{\alpha'},\nexists,1)\right) \\
&- \frac{C_{eb}(i_{\alpha'},1,1)}{\Delta\gamma} \times \left(H_{\beta'}^{n+\frac{1}{2}}(i_{\alpha'},1,1) - H_{\beta'}^{n+\frac{1}{2}}(i_{\alpha'},1,\nexists)\right)
\end{aligned} \tag{3.81}
$$

The magnetic field components $H_{\gamma'}^{n+\frac{1}{2}}(i_{\alpha'},\nexists,1)$ and $H_{\beta'}^{n+\frac{1}{2}}(i_{\alpha'},1,\nexists)$ do not exist in the problem space. They can be calculated as in equation 3.82a and 3.82b.

$$
H_{\beta'}^{n+\frac{1}{2}}(i_{\alpha'},1,\nexists) = H_{\beta'}^{n+\frac{1}{2}}(i_{\alpha'},1,N_{\gamma}) \times e^{jk_{\beta}N_{\beta}\Delta_{\beta}} \tag{3.82a}
$$

$$
H_{\gamma'}^{n+\frac{1}{2}}(i_{\alpha'},\nexists,1) = H_{\gamma'}^{n+\frac{1}{2}}(i_{\alpha'},N_{\beta},1) \times e^{jk_{\gamma}N_{\gamma}\Delta_{\gamma}} \tag{3.82b}
$$

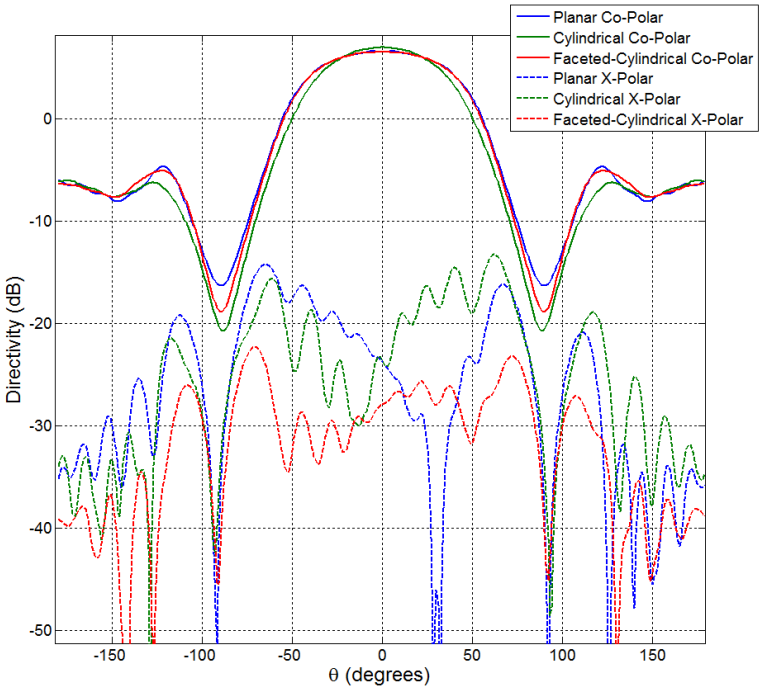

FIGURE 3.8: *PASim* Simulation of AEPs of planar, cylindrical(100λ radius), and faceted-cylindrical(100λ radius) arrays.

After electric field component $E_\alpha^{n+1}(i_\alpha, 1, 1)$ are computed using equation 3.44, All the electric field components $E_\alpha^{n+1}(i_\alpha, N_\beta + 1, 1)$, $E_\alpha^{n+1}(i_\alpha, 1, N_\gamma + 1)$, and $E_\alpha^{n+1}(i_\alpha, N_\beta + 1, N_\gamma + 1)$ at other corners can be computed using equations 3.83, 3.84, and 3.85.

$$E_\alpha^{n+1}(i_\alpha, N_\beta + 1, 1) = E_\alpha^{n+1}(i_\alpha, 1, 1) \times e^{-jk_\beta N_\beta \Delta_\beta} \tag{3.83}$$

$$E_\alpha^{n+1}(i_\alpha, 1, N_\gamma + 1) = E_\alpha^{n+1}(i_\alpha, 1, 1) \times e^{-jk_\gamma N_\gamma \Delta_\gamma} \tag{3.84}$$

$$E_\alpha^{n+1}(i_\alpha, N_\beta + 1, N_\gamma + 1) = E_\alpha^{n+1}(i_\alpha, 1, 1) \times e^{-jk_\beta N_\beta \Delta_\beta} \times e^{-jk_\gamma N_\gamma \Delta_\gamma} \tag{3.85}$$

3.4 Simulation of Active Element Patterns

Figure (3.8) shows an example of principle plane cuts for AEPs from an infinite-by-infinite planar array, a 100λ-diameter cylindrical array, and a 100λ-diameter faceted-cylindrical array. 1257 radiating elements with $\frac{\lambda}{2}$ spacing can occupy one ring (the circumference of the cylinder) of the 100λ-diameter cylindrical array. 1256 radiating elements with $\frac{\lambda}{2}$ spacing can occupy one ring of the 100λ-diameter faceted-cylindrical array. The array element was modeled using the same specification for all three manifolds and Figure 3.9 shows the dimensions of it. Therefore the operating frequency is 2.8 GHz with very narrow bandwidth. In the section 3.5.1, more details of this patch antennas are presented. The blind spot in each AEP at $\pm 90^{\circ}$ and slightly high directivity ($\sim$ 0.5dB) of cylindrical array case compare to the planar array case are noteworthy.

3.5 Applications and Validation of FDTD Simulations

The patch antennas in subsection 3.5.1 and subsection 3.5.2 are designed for 2.8 GHz (in S-band) center frequency and fabricated on Rogers RT/duroid 5880 with 0.062inch(1.575mm) thickness and 0.5 oz(17μm) copper cladding. This high thickness and a low relative dielectric constant of the substrate of microstrip patch antenna stimulate the process of radiation. In addition to that, RT/duroid 5880 has resistivity to absorb moisture and change the electrical properties with temperature, which make the material perfect for low-cost patch antenna application. Since the S-band is the most desirable microwave frequency band used in weather measurement, 2.8GHz was selected as the center frequency for both narrow band patch antennas. The patch size is $0.5\lambda \times 0.5\lambda$ (54×54 mm^2), since both antennas were designed for a planar array with 0.5λ element spacing. The pictures of fabricated patch antennas are in figure 4.6 in section 4.2.1.1. Simulation results from

HFSS and xFDTD are compared with the simulation data from *PASim* program. In addition to the simulation data comparison, the measurements of a fabricated patch antenna are plotted on the same plots of simulation for comparison.

3.5.1 A Simple Patch Antenna

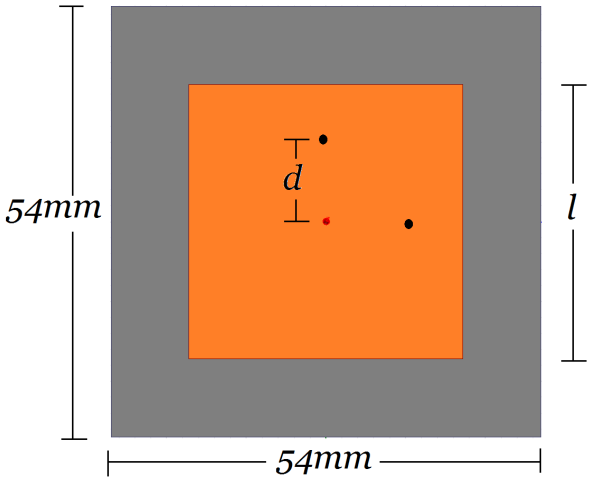

FIGURE 3.9: Geometry of the simple patch antenna design

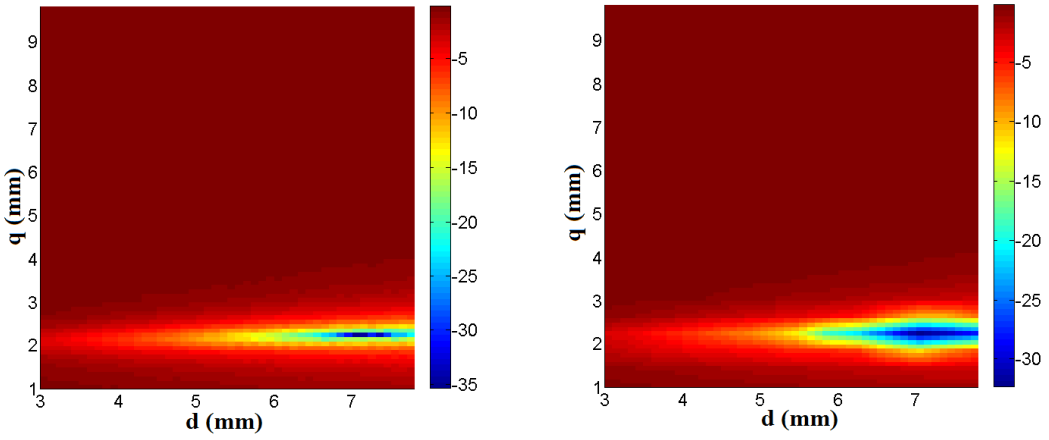

(a) Parameter analysis using HFSS

(b) Parameter analysis using *PASim*

FIGURE 3.10: Parameter analysis of Return Loss for the simple patch antenna

This is a simple patch antenna as depicted in Figure 3.9. This patch antenna which design was simulated and optimized , and then HFSS is used to validate the FDTD program. The genetic algorithm, which is a built-in capability of HFSS is

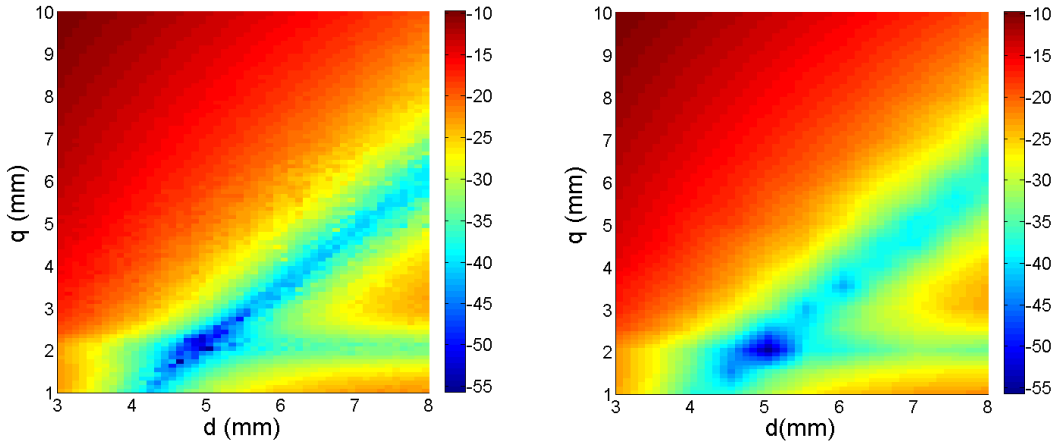

(a) Parameter analysis using HFSS

(b) Parameter analysis using *PASim*

FIGURE 3.11: Parameter analysis of Isolation for the simple patch antenna

Parameter	d	l
HFSS	7.082mm	34.371mm
PASim	6.825mm	34.125mm

TABLE 3.1: Best Case of Simple patch Antenna

used to do the optimization of a patch antenna for minimizing the possible return loss (RL) and insertion losses (IL). As presented in Table 3.1 HFSS and *PASim* optimizations based on the genetic algorithm are having excellent agreement. Note from Figure 3.10 and 3.11, the minimal IL and RL are not achieved by the same set of parameters. Here we have two design parameters - the probe location on x axis and y axis (parameter d) and the dimension of square shaped patch (parameter l). Since the *PASim* is using uniform grid with cell size 0.525mm×0.525mm×0.525mm and interpolation to generate parameter analysis plots, the parameter analysis plots has very few disagreements. Isolation and return loss is evaluated at 2.8GHz frequency for $d \in (3, 8)$ and $q \in (1, 10)$ where $l = 32 + q$. The minimum return loss and minimum isolation are not at the same location as in figure 3.10 and 3.11. Since there are only two degrees of freedom, we can not control the location of the minimum return loss and the minimum isolation.

The return loss and isolation of the best case of the patch antenna design are

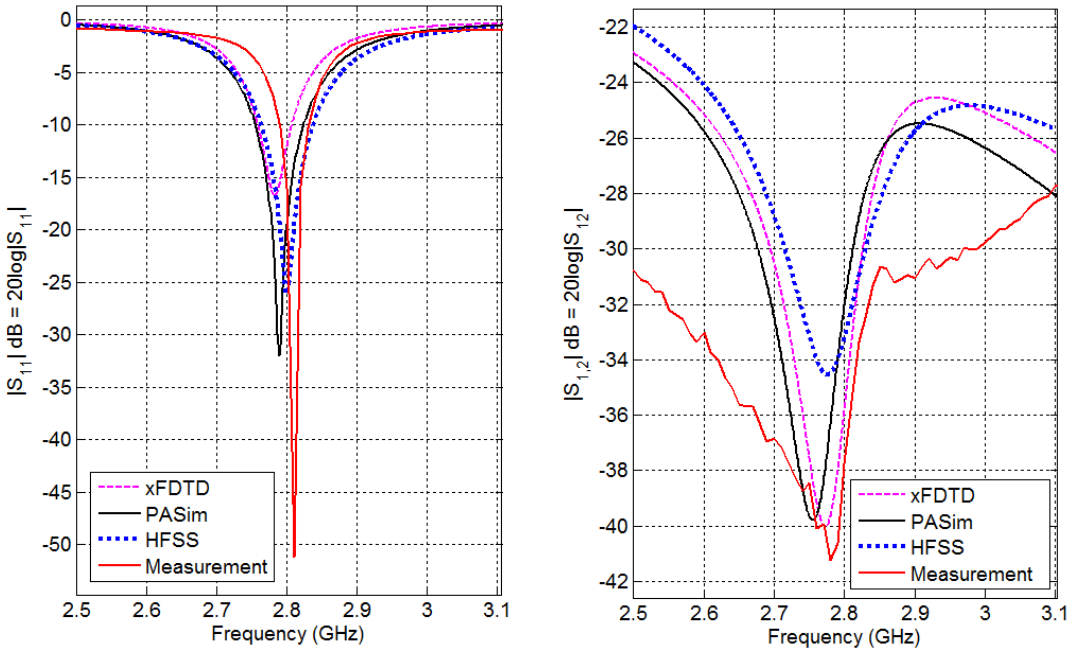

(a) Return Loss ($RL = -20\log|S_{11}|$)

(b) Isolation ($I = -20\log|S_{12}|$)

FIGURE 3.12: Return Loss, Isolation of the simple patch antenna

Parameter	a	d	l	p	q	t
Value(mm)	9.151	6.400	31.973	11.487	10.706	1.000

TABLE 3.2: Best Case of patch Antenna with slots

plotted in Figure 3.12. The return loss and isolation data taken through measurement and simulations by HFSS, xFDTD, and *PASim* was plotted on the same plot for comparison (figure 3.12). The radiation pattern measurement using near-field technique and simulation data from *PASim* are plotted in figure 3.13.

3.5.2 Patch Antenna with Arc-Shaped Slots

Parameter d and l are same as simple patch antenna. The parameter a is the radius of the arc slots. The parameter p is the coordinate of the center of arc slot ($x = y = p$). The parameter q will determine the sector size of the arc. The parameter t is the width of the slot. Since this designing has five parameters, the visualization of parameter analysis is not presented.The genetic algorithm with

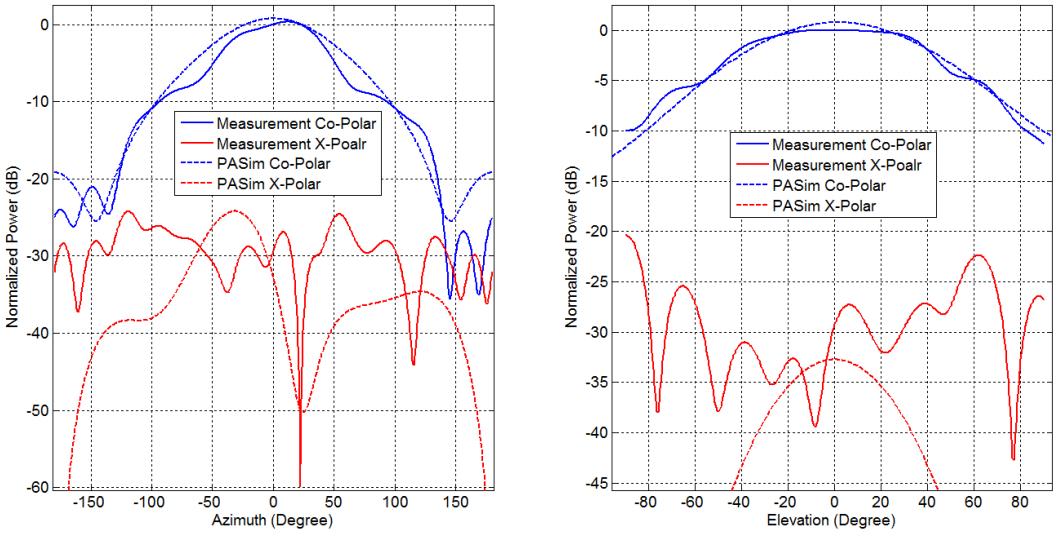

(a) Azimuth Principal Cut

(b) Elevation Principal Cut

FIGURE 3.13: Azimuth and Elevation Principal Cut of the simple patch antenna

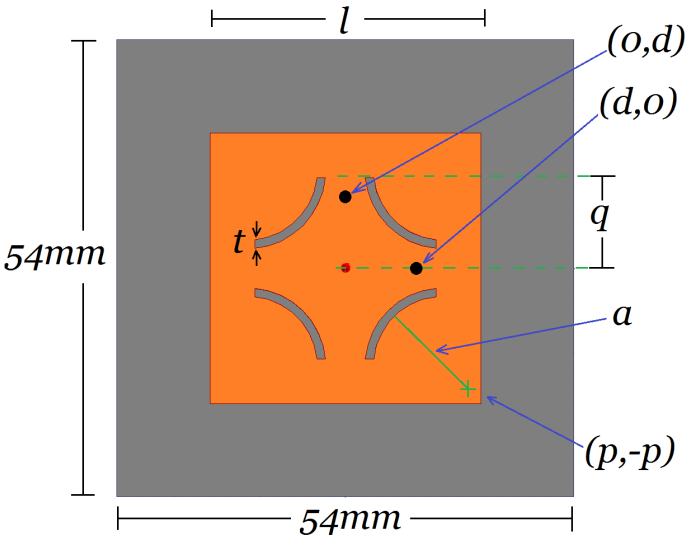

FIGURE 3.14: Geometry of patch antenna with slots

20,247 iterations is used to determined the best case of the patch antenna. The optimization and sensitivity analysis using HFSS is carried out for lowest possible return loss and isolation. The parameter values can be found in table 3.2.

The Figure 3.15 shows the return loss and isolation of the best case of the patch antenna. AS in the section 3.5.1, the PNA measurements and simulations by HFSS, xFDTD, and FDTD program are used to compare the return loss and isolation data (figure 3.15). The figure 3.13 shows the radiation pattern measurement using

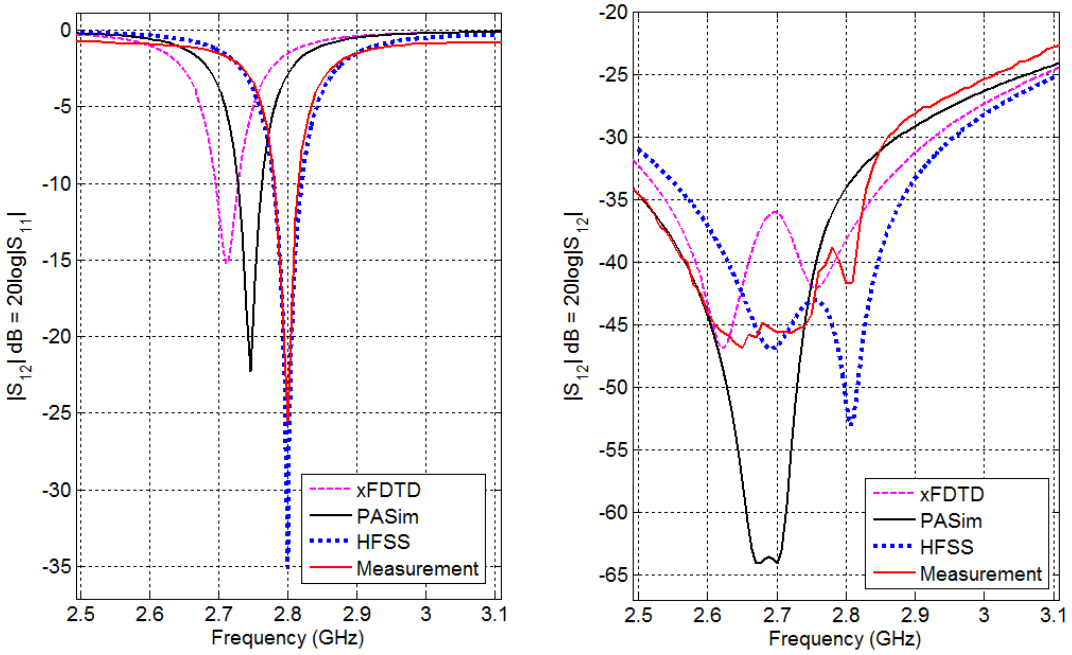

(a) Return Loss ($RL = -20\log|S_{11}|$)

(b) Isolation ($I = -20\log|S_{12}|$)

FIGURE 3.15: Return Loss, Isolation of the patch antenna with slots

near-field technique and simulation data from PASim.

3.5.3 Multilayer Patch Antenna Designed by MIT Lincoln Laboratory

MIT Lincoln Laboratory proposed a multilayer patch antenna for future MPAR application. In this subsection, the VSWR from both HFSS simulation and FDTD program will be presented and compared. The antenna element is simulated as an active element in Infinite-by-Infinite array in both HFSS and FDTD program. So HFSS is using Master-Slave boundary condition, a frequency domain method for handling periodic boundary. FDTD program is using periodic boundary condition in time domain, which was explained in this chapter with details. The size of the element is 25.4mm $\times$ 25.4mm with two substrate layers. Nelco N4000-13, which has 3.22 dielectric constant and 0.008 loss tangent is used to fabricate the bottom substrate. Rohacell - 71 HF, which has 1.075 dielectric constant and

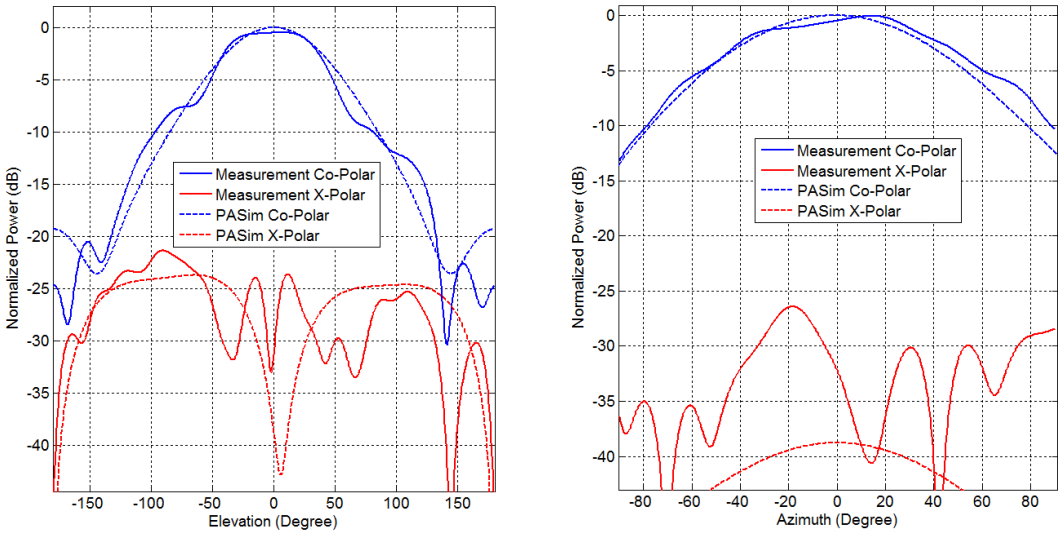

(a) Azimuth Principal Cut

(b) Elevation Principal Cut

FIGURE 3.16: Azimuth and Elevation Principal Cut of the patch antenna with slots

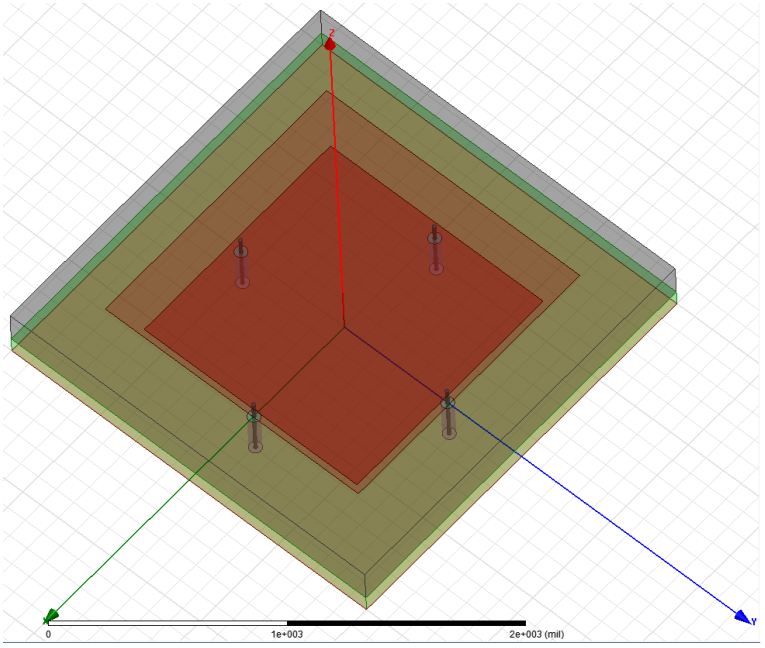

FIGURE 3.17: HFSS model of Multilayer Patch Antenna For The Future MPAR By MIT Lincoln Laboratory.

0.0002 loss tangent is used to fabricate the top substrate. Bottom gold patch size is 15.2354mm × 15.2354mm and the top gold patch sized is 18.1229mm × 18.1229mm. The ground plane is also gold. The ports are located at (0,14.76065), and (0,-14.76065) for H channel. They should be excited simultaneously with 180°

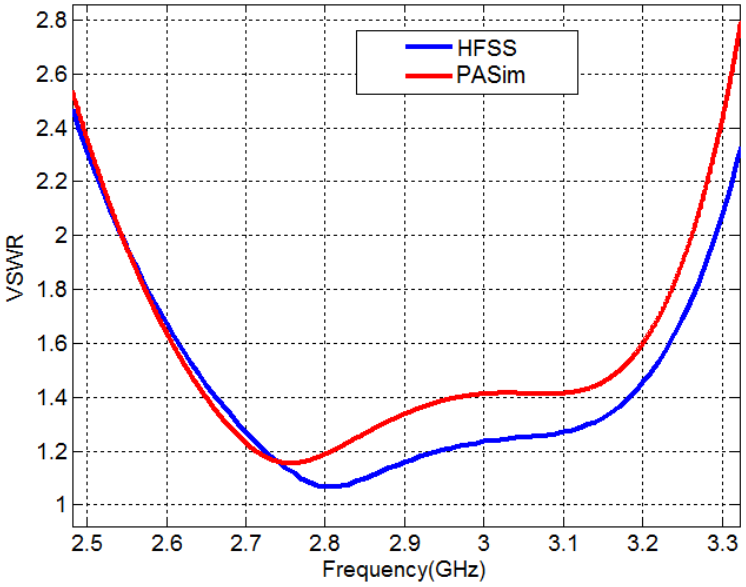

FIGURE 3.18: VSWR of Multilayer Patch Antenna For The Future MPAR By MIT Lincoln Laboratory.

phase shift. (14.76065,0) and (-14.76065,0) are the location for V channel.

Chapter 4

Laboratory Measurements

The physically observable phenomena of antennas are measured to investigate performance such as gain, pattern, directivity, and polarization. Mechanical rotation of the antenna under test (AUT) or the probe antenna will directly affect the measured pattern and natural polarization vectors and will affect the conclusions of performance caparisons with overlaid patterns or pass-fail specification lines. Before the comparison is carried out, it is utmost important to understand and select the proper coordinate system that AUT is being measured.

Some of the arrays and antennas presented in this dissertation are measured in old far-field measurement facility, which was merely a conversion of office area into an anechoic chamber with electromagnetic absorbers. The horizontal and vertical principal plane cuts off the antenna pattern was measured in the old far-field chamber. Since the measurements in different coordinated systems will be the same at principal plane cuts as shown in Section 4.1, it was not necessary to pay more attention to the coordinate system used in the old chamber. The modern antenna test ranges located at Radar Innovations Laboratory are used for all the antennas measurements taken after 2014. There is one near-field chamber installed and validated by Nearfield Systems Inc. (NSI) and a Far-Field chamber installed by ORBIT/FR.

The Near and Far-Field Chambers located at RIL can measure many free-space

characteristics of antennas. The most important measurable characteristics are free-space radiation pattern, directivity, and polarization. Other properties can be derivations of these three. As an example gain is proportional to directivity and the proportional constant is antennas efficiency. Essential theories and practices of antennas and array antenna measurement, which are used in this work will be presented in this chapter.

4.1 Coordinate systems

Antenna radiation patterns are measured using mechanical systems (robotic systems or automated rotary stage systems) in order to collect the field intensities at each point of imaginary surfaces. Then the data points are discrete and taken at the locations designated by the systems (mechanical systems and the software systems). In a near-field facility, the imaginary surface can be planar, cylindrical, spherical, or other surfaces. A typical far-field measurement system can take the measurement in spherical coordinate system [94]. If the system does not map the directivity, polarization, or radiation pattern to desired surfaces, proper formulas can convert them to the desired one. In this section, the conversion of those coordinate systems will be presented. More details can be found in [95] Appendix A1.5 of [94] and Appendix C of [96].

4.1.1 Coordinate System for Far-Field Data Acquisition

In the far-field measurement, one can have three kinds of spherical coordinate systems, using roll-over-elevation-over-azimuth positioner. In the description of these three systems, the pole is an important definition. In this three coordinate systems, all the data points are located at separate locations except that two sets of data points are overlapped at two locations. Those two exceptional points are recognized as poles. The importance of poles can be easily observed using a very common earth's surface map based on the Mercator projection [97].

The Mercator projection is used to plot the layout of the Earth's surface on a spherical shape earth onto a cylindrical shape. Even though world map generated by Mercator projection is so popular, the area of some lands located in the vicinity of north and south poles (Greenland, Alaska, Finland, and Antarctica) are very inaccurate. As an example, Mercator projection says the Greenland is larger than Africa. The real size of Africa is fourteen times larger than the real size Greenland. The distortions of the radiation pattern near to the poles are analogous to the inaccurate layout information of the Earth's surface from Mercator projection near to the north and south poles [94].

4.1.1.1 Direction Cosine

In the direction cosine coordinate system, the unit vector $\hat{r}$ of the position vector $\vec{r}$ to the data point is used to define the projected components in $\hat{x}$, $\hat{y}$ and $\hat{z}$ of the Cartesian coordinate system. Those projected components are commonly annotated as u, v, and w. Then it can be written in a mathematical formula as in the below equation.

$$\hat{r} = \cos\alpha\hat{x} + \cos\beta\hat{y} + \cos\gamma\hat{z} = u\hat{x} + v\hat{y} + w\hat{z} \tag{4.1}$$

The direction cosine is introduced first because it is used as a reference coordinate system to define the polar spherical, azimuth over elevation, and elevation over azimuth coordinate systems in subsequent subsections.

4.1.1.2 Polar Spherical

These are the coordinate systems specific to the roll-over-azimuth positioner system 4.1(a). The roll-over-azimuth positioner system has two positioners, which are for incrementing ϕ and θ angles. The data points can be taken in two ways, depending on the way ϕ and θ angles are incremented. While the θ angle is fixed in a position ϕ is incremented for all the possible set of values and vice versa.

Either way can generate the same set of data points, even though the first one can be the preferred choice to minimize wear and tear of the rotary stage. This is the only possible way to measure the radiation in a full spherical surface without any EM wave blockage by the positioner system [94]. The range of θ and ϕ can be defined in different ways in order to measure data point on a complete sphere.

$$u = \sin\theta\cos\phi \tag{4.2a}$$

$$v = \sin\theta\sin\phi \tag{4.2b}$$

$$w = \cos\theta \tag{4.2c}$$

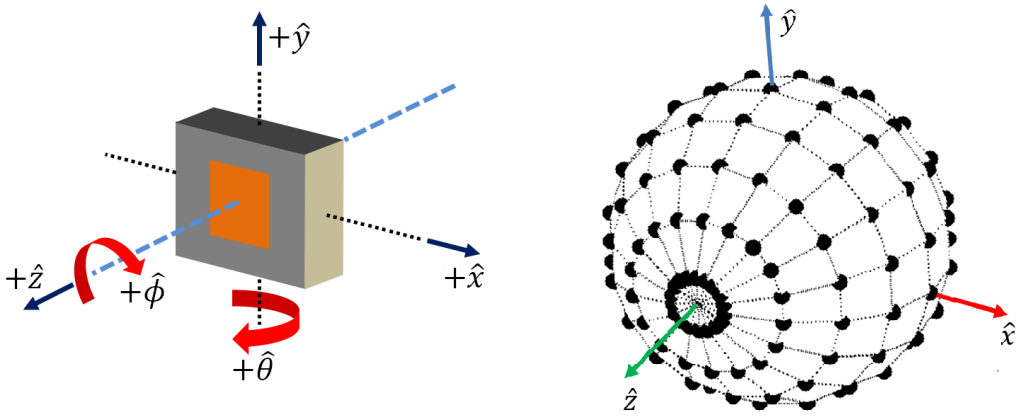

(a) A patch antennas being measured

(b) The data points on the sherical surface

FIGURE 4.1: Measurement using roll-over-azimuth.

4.1.1.3 Azimuth Over Elevation

An azimuth-over-elevation positioner systems also has two positioners, which are for incrementing azimuth (az) and elevation(el) angles. While el angle is fixed in a position az is incremented for all the values defined in the discrete range of az. then the pole is in $\hat{y}$ direction. The positioner system will not create any blockage for az range but el range is limited by a blockage. The possible moving direction of patch antenna and data point on spherical surface is shown on Figure 4.2(a) and

4.2(b). The direction cosines in terms of az and el can be related as on Equation 4.3a, 4.3b, and 4.3c.

$$u = \sin az \cos el \tag{4.3a}$$

$$v = \sin el \tag{4.3b}$$

$$w = \cos az \cos el \tag{4.3c}$$

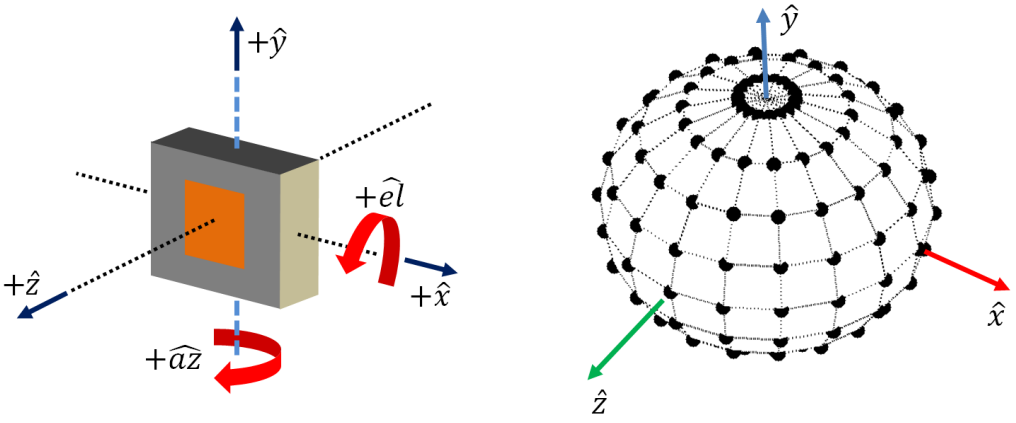

(a) A patch antennas being measured

(b) The data points on the sherical surface

FIGURE 4.2: Measurement using azimuth-over-elevation.

4.1.1.4 Elevation Over Azimuth

An elevation-over-azimuth positioner system is same as the azimuth-over-elevation positioner system except that the pole of the system is in $\hat{x}$ direction. It is due to el is incremented, while az angle is fixed in a position. The similarity and difference between the elevation-over-azimuth and azimuth-over-elevation positionar systems can be clearly observed by the comparison of Figure 4.3(a) with 4.2(a) and Figure 4.3(b) with 4.3(b).

$$u = \sin az \tag{4.4a}$$

$$v = \cos az \sin el \tag{4.4b}$$

$$w = \cos az \cos el \tag{4.4c}$$

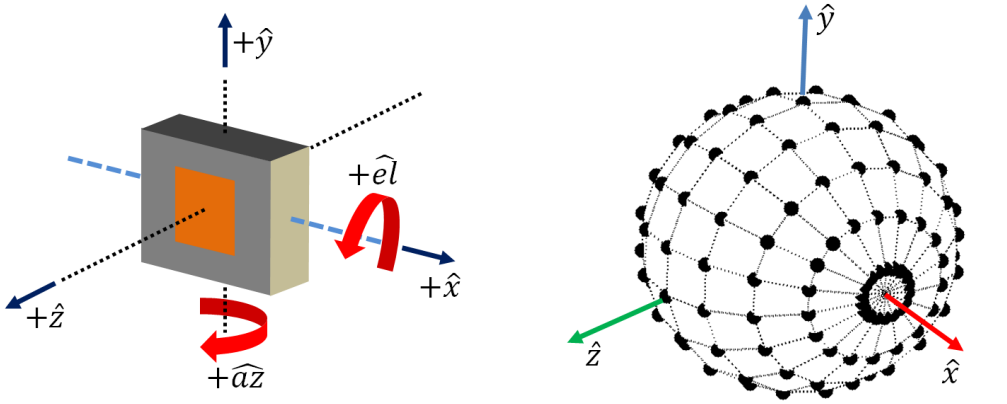

(a) A patch antennas being measured (b) The data points on the sherical surface

FIGURE 4.3: Measurement using elevation-over-azimuth.

4.1.2 Coordinate System for Near-Field Data Acquisition

There are three acquisition geometries commonly used in near-field range. Those are planar, cylindrical, and spherical acquisition geometries. In the near-field chamber located at Radar Innovations Laboratory, the AUT is always mounted on a vertical plane. The maximum AUT cross section and maximum probe cross section will be aligned at the initial position. The complex voltage values of each data location will be used to transform (near-field to far-field transformation) the far-field radiation. Rectangular waveguides are used as the range antenna or the near-field probe since they possess many attractive characteristics such as time invariant gain, low directivity, electrically small, wide bandwidth, low scattering cross-section, and polarization purity. The probe and the AUT should be positioned apart with recommended distance to avoid evanescent wave in data collection. Hence it collects signal in propagating near-field region, not the reactive near-field.

4.1.2.1 Planar Near-Field Scanner (PNFS)

Near-field measurement setup using planar acquisition geometry collects the data in plane rectilinear grid. The near-field probe scans the aperture of AUT on the

xOy plane, while the AUT is stationary. This scanner is more appropriate for highly directive antennas measurement since the probe can cover limited solid angle. The truncation of predictable far-field data is an intrinsic limitation of PNFS.

4.1.2.2 Cylindrical Near-Field Scanner (CNFS)

In this scanner, the probe is moving up and down vertically while AUT is rotating to change azimuth angle. Then the data points are located on a cylindrical grid. This scanner is more appropriate fan-beam type antennas measurements since there is a limitation in vertical scanning.

4.1.2.3 Spherical Near-Field Scanner (SNFS)

The pointing direction of a stationary probe is the pole of the spherical acquisition geometry. Initially, the AUT's aperture is on xOy plane and probe is perpendicular to xOy plane. When the data acquisition or measurement of the electric field at each designated point is being done, the incrementation of θ will be done by rotating the AUT in azimuth and the AUT rotates around its center of the aperture in order to increment the ϕ.

4.1.3 Cross Polarization Definitions

In the far-field measurement, the cross polarization is the polarization orthogonal to a reference polarization. However, this is neither formal nor a complete definition of cross polarization. The electric and magnetic fields at far-field are completely and unambiguously defined by an electric and magnetic field vectors perpendicular to the direction of EM wave propagation, as the EM wave will have the planar wave condition (locally) at far-field. Thereupon one can define the electric field and magnetic field with two transverse electric and magnetic field vector components. According to the IEEE145-2013 [98], the cross polarization is

defined as "In a specified plane containing the reference polarization ellipse, the polarization orthogonal to a specified reference polarization". However the classical definitions presented by Arthur Ludwig [99] in 1973 are the formal way to express the cross polarization in practice. In that paper, Ludwig had given three definitions of cross polarization, which are discussed in next three subsections.

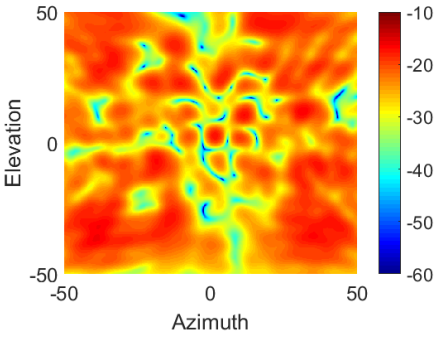

(a) Azimuth-over-elevation whith Ludwig II

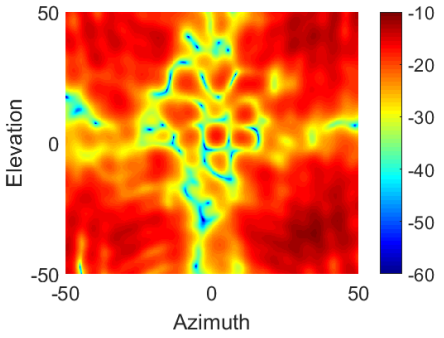

(b) Elevation-over-azimuth whith Ludwig II

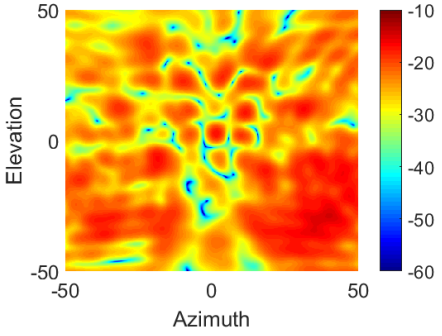

(c) Azimuth-over-elevation whith Ludwig III

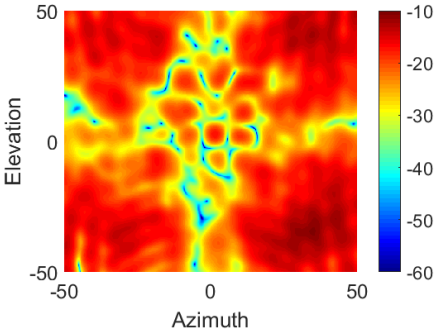

(d) Elevation-over-azimuth whith Ludwig III

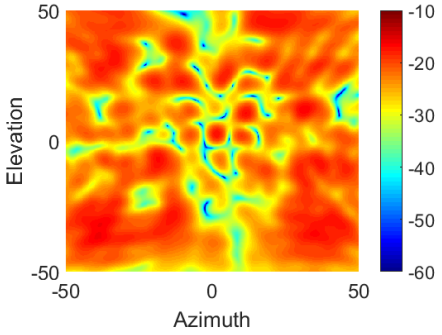

(e) Polar spherical whith Ludwig III

FIGURE 4.4: Cross popularization of an active element pattern at (4,4) location of an 8×8 planar array with different cross polar definitions and coordinate systems

4.1.3.1 Ludwig I

The Ludwing's first definition is presented with Cartesian polarisation basis $\hat{e}_x$, $\hat{e}_y$, and $\hat{e}_z$, which are unit vectors in X, Y, and Z directions respectively. The electric field vector using **Ludwig I** at any far-field data acquisition point can be expressed in simple mathematical form (equation 4.5).

$$\vec{E} = E_x\hat{e}_x + E_y\hat{e}_y + E_z\hat{e}_z \tag{4.5}$$

In equation 4.5, E_x is co-polar electric field intensity component and E_y is cross-polar electric field intensity component. The $E_y \approx 0$ can be considered valid approximation in the vicinity of $\theta = 0$. The Co-Polarization and Cross-polarization are oriented in $\hat{e}_x$ and $\hat{e}_y$ direction on every possible data acquisition points on the imaginary far-field spherical surface. If the data acquisition points are taken with polar spherical coordinate system, E_x and E_y can be calculated using E_θ and E_ϕ components measured using Ludwig's second definition with polar spherical coordinate system.

$$E_x = E_\theta \cos\theta \cos\phi - E_\phi \sin\phi$$

$$E_y = E_\theta \cos\theta \sin\phi + E_\phi \cos\phi$$

$$E_z = -E_\theta \sin\theta$$

Notice the E_z is not zero unless $\theta = 0$. Nevertheless only E_x and E_y are used to represent polarization at far-field measurements. Thus the measurements are accurate and reliable only in the vicinity of $\theta = 0$. Due to this reason, the community of antenna measurement is less favorable towards this definition.

4.1.3.2 Ludwig II

Generally, Ludwing's second definition of cross polarization can be presented in two different coordinate systems, which are azimuth-over-elevation and elevation-over-azimuth. Anyhow the near-field measurement systems at RIL has the option to translate the near field data taken by using PNFS, CNFS, or SNFS into polar, spherical coordinate system. The polar spherical coordinate system will have many E_θ and E_ϕ at $\theta = 0$, which is called the **singularity** at $\theta = 0$. That is the bore sight of the antenna pattern.

Whereas at far-field, the electric field in the direction of EM propagation is zero. In other words, the field components perpendicular to the imaginary spherical surface at far-field has to be zero. Subsequently the field at far-field can be expressed using azimuth-over-elevation or elevation-over-azimuth coordinate system as:

$$\vec{E} = E_{az}\hat{e}_{az} + E_{el}\hat{e}_{el} \tag{4.6}$$

The Co-Polarization and Cross-polarization are oriented in $\hat{e}_{az}$ and $\hat{e}_{el}$ direction on every possible data acquisition points on the imaginary far-field spherical surface with azimuth-over-elevation or elevation-over-azimuth coordinate system. The singularities are 90° away from bore sight

Note : *Entire measurements presented in this dissertation are in azimuth-over-elevation coordinate system with Ludwig's second definition of cross polarization.*

4.1.3.3 Ludwig III

The usage of this definition is more common in the antenna measurement community. The far-field data can be taken when the AUT is rolling in ϕ and positioning in θ (roll-over-azimuth) while the range antenna is rolling. Unlike the far-field measurement data taken with only polar spherical coordinate system, the probe and AUT coupling is invariant at $\theta = 0$ through out the measurement process. No singularity at any location is the main advantage of this definition. The electric

field vector at each data point can be given in three components E_{co}, E_{cr}, and E_r. Hence E_r are in the planar wave propagation direction, Considering $E_r = 0$ is both theoretically and experimentally accurate.

$$\vec{E} = E_{co}\hat{e}_{co} + E_{cr}\hat{e}_{cr} \tag{4.7}$$

The polar spherical electric field components and orthoganal electric field components from the third definition can be related as :

$$\vec{E}_{co} = E_\theta \cos\phi - E_\phi \sin\phi \tag{4.8a}$$

$$\vec{E}_{cr} = E_\theta \sin\phi + E_\phi \cos\phi \tag{4.8b}$$

More generalized and detailed definition of Ludwig's third definition will depend upon θ as presented by Roy and Shafai [100]. The generalized equation can be written as equation 4.9a for co-polarization and equation 4.9b for cross-polarization.

$$\vec{E}_{co} = E_\theta \cos\zeta - E_\phi \sin\zeta \tag{4.9a}$$

$$\vec{E}_{cr} = E_\theta \sin\zeta + E_\phi \cos\zeta \tag{4.9b}$$

The angle ζ depends on θ and ϕ given by the observation direction and φ, which is the direction of perfectly polarized aperture field.

$$\zeta = \arctan \frac{1}{\cos(\theta)\tan(\varphi - \phi)}$$

When the perfectly linear polarized field is oriented in $+\hat{y}$ direction, φ will be $\pi/2$ (90 degrees). Subsequently the equation will appear to be $\zeta = \arctan \frac{\tan(\phi)}{\cos(\theta)}$. It is important to note that equation 4.8a and 4.8b will be valid when $\theta = 0$ and perfectly linear polarized field is oriented in $+\hat{y}$ direction. Figure 4.4 shows the cross-polar active element pattern of the element at (4,4) location of planar

array antennas. Depending on the testing antenna's orientation and the channel excited, azimuth-over-elevation (Figure 4.4(a)) or elevation-over-azimuth (Figure 4.4(b)) coordinate system will be used. It is noteworthy that the Figure 4.4(b) and 4.4(d) are much smiler.

4.2 Measurement Setups in Near and Far-Field Chambers

4.2.1 Measurement Setups in Near-Field Chamber

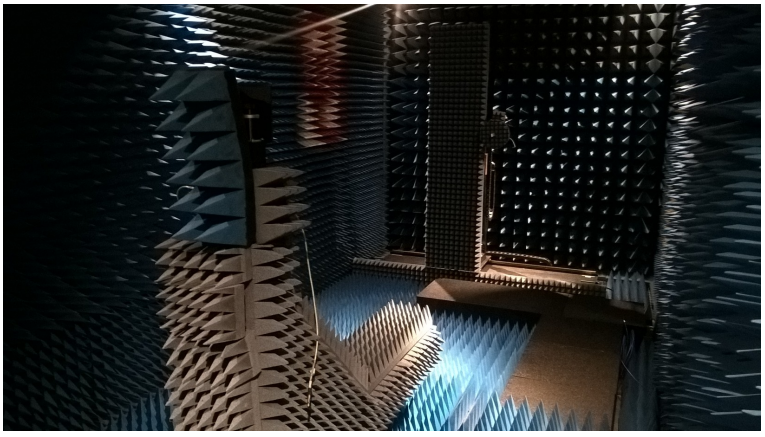

FIGURE 4.5: Near-Field Chamber at RIL

The chamber is 11 feet wide, 26 feet long, and 11 feet tall. The recommended temperature is $68° \pm 2°$ and the nonconducting humidity should be between 35% and 75% for taking a measurement with optimum accuracy. The probe can move ± 32.21 inch horizontally (X axis) and ± 31.23 vertically (Y axis). Then the probe can cover 4024 square inches (horizontally 64.42 inches $\times$ vertically 62.46 inches) on a planar surface in near field planar antenna measurements. The azimuth base can be rotated 360°, which can cover $\theta \in [-180, 180]$ in cylindrical and spherical near-field measurements. The $\phi \in [0, 360]$ in the spherical coordinate system can be incremented by a positioner mounted on the azimuth base. The azimuth base can move 78.74 inch in the z direction to make the initial fixed position of the

AUT. In addition to that, the probe can move 4 inches in the z direction to make small adjustments.

4.2.1.1 Isolated Patch Antennas

The isolated patch antennas (shown in Figure 4.6), which are used to validate the *PASim* program was measured in the near-field chamber for obtaining the far-field co-polar and cross-polar radiation pattern. The relevant antennas were measured using SNFS with 3 degrees θ and ϕ resolution. The probe was at a fixed position in the middle of XY plane. The antennas and cylindrical scanner alignment were done using laser alignment tools. Therefore the middle point of the probe is aligned with the middle point of the patch antenna at the initial position.

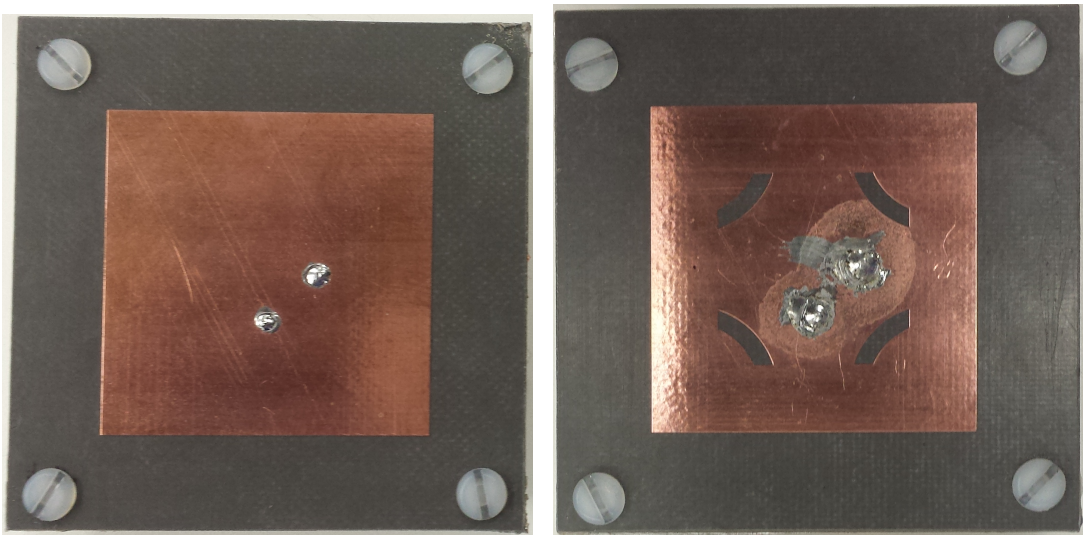

(a) The Simple Patch (b) The Patch with Slots

FIGURE 4.6: CPAD-1 : Measured 3D transmitting pattern of the planar 4×4 CPAD configuration.

The probe-to-azimuth stage radius, an important distance to be measured is the distance between the front of the probe to the axis of the azimuth stage where the AUT is mounted. The accuracy of this measurement should be within a wavelength of the operating frequency or the desired frequency. The AUT will not be able to locate on the axis of the azimuth stage. Then the distance between axis to the AUT, maximum radial extent (MRE) has to be measured. Even though the

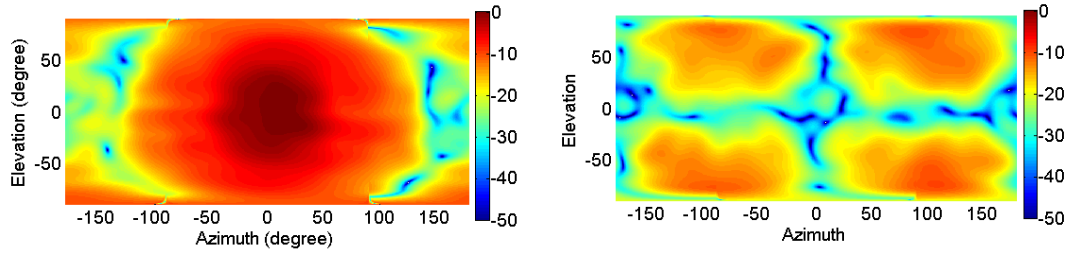

(a) Co-Polar 3D Pattern of the Simple Patch

(b) Cross-Polar 3D Pattern of the Simple Patch

(c) Co-Polar 3D Pattern of the Patch With Slots

(d) Cross-Polar 3D Pattern of the Patch With Slots

FIGURE 4.7: CPAD-1 : Measured 3D transmitting pattern of the planar 4×4 CPAD configuration.

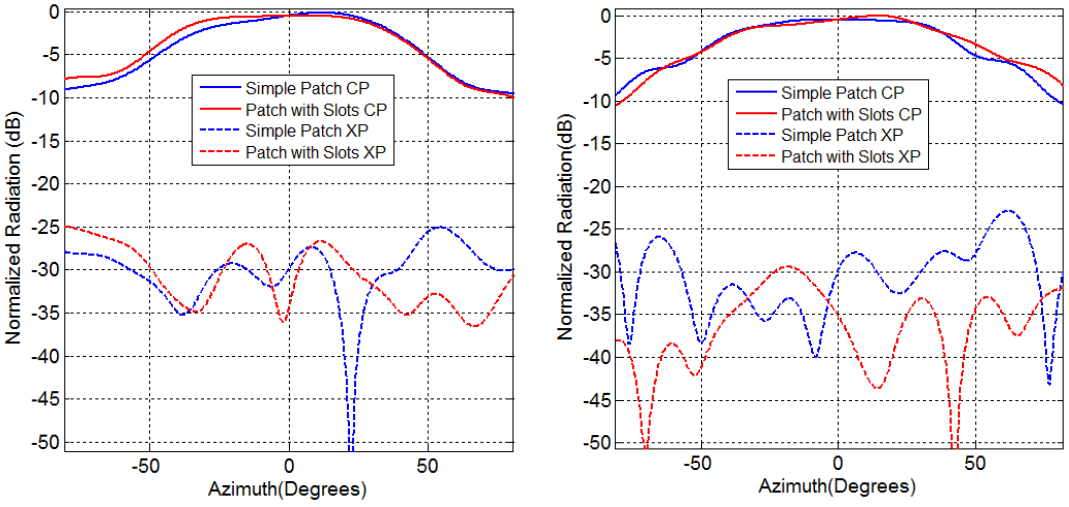

(a) Horizontal Plane Principal Cut

(b) Vertical Plane Principal Cut

FIGURE 4.8: CPAD-1 : Measured 3D transmitting pattern of the planar 4×4 CPAD configuration.

accuracy of MRE is not critical, this distance should be entered in the measurement software.

Figure 4.6(a) and 4.6(b) are the pictures of simple single layer patch antenna and single layer patch with slots. The patch in Figure 4.6(b) does have better isolation between ports than simple patch antenna. As the elements are separated by $\frac{\lambda}{2}$

in both array antennas and having compact the metal patch size, lower mutual coupling in an array of single layer patch antennas with slots can be anticipated. Thereupon both of them are having low-frequency bandwidth (BW $< 2\%$). These patch antennas are not suitable as radiating elements for MPAR. However, they revealed some interesting design tradeoffs. Hence antenna's manifolds and different configurations of radiating elements on particular antenna manifold can be characterized with low cost and limited resources.

4.2.1.2 Active Element Pattern

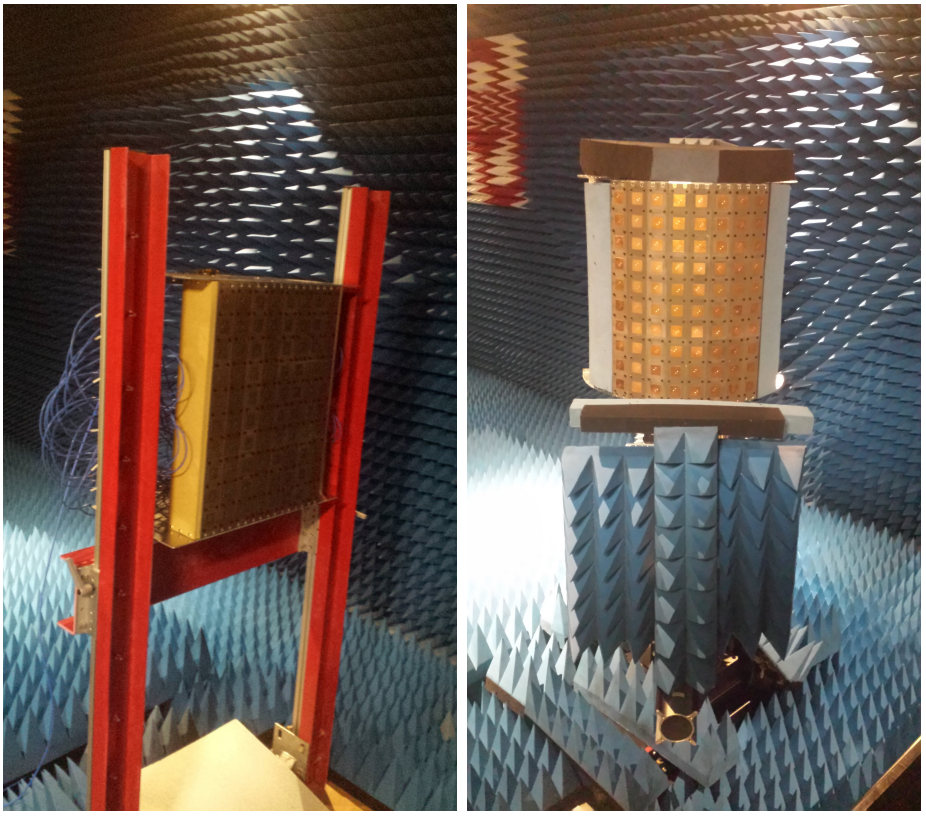

(a) Planar Array (b) Cylindrical Array

FIGURE 4.9: Planar and cylindrical array antenna configurations in near-field chamber measurement.

In some literature, the active element pattern is called embedded element pattern in order to avoid the misleading meaning in word *"active"* [101–103]. In this dissertation, active element pattern will be used to call this important measurable

parameter of phased array antennas. The AEP can be used to do the precise gain and radiation pattern generation using the same mathematical procedure used in isotropic array radiation pattern generation. In addition to that, AEP can be used to calculate the mutual coupling between radiation elements. In order to measure the active element pattern, one port of a test patch antenna element is excited, while all the other ports are terminated with match load (50Ω). This element pattern includes the mutual coupling between element, as they are measured in an array environment. AEPs for the 64-element planar and cylindrical array elements are measured in a near-field chamber at RIL. The initial goal was to do the electromagnetic characterization of planar and cylindrical array manifold with the same number of elements. The paper by Guifu Zhang and others [44] did the layout of theoretical works to compare polarimetric planar and cylindrical array antenna manifolds and discussed seven benefits of using cylindrical array manifold, more specifically in weather measurements. In this electromagnetic characterization, the validation of some of the benefits could be done. The polarization puerility, scan-invariant beamwidth, and scan-invariant polarization characteristics are the benefits that can be validated using these measurements. This is discussed more in section 5.5 and section 5.6.

The 64-element planar array was measured in planar near-field measurement scanner. Since the distance between AUT and the probe should be absolutely invariant in the measurements of all the elements the probe is moving in [a truncation of the range] to collect data at designated data points. The data points are separated by 0.5 inch in both x and y axises. The distance between probe to AUT is [around 5λ (20 inch)] and the operating frequency is 2.8GHz. Accordingly after near-field to far-field transformation with Azimuth-over-elevation coordinate system, the far-field radiation data could be predicted in $[-40°, 40°] \times [-40°, 40°]$ azimuth and elevation range. A special support had to be constructed to mount the planar array measurement in the near-field chamber (Figure 4.9(a)).

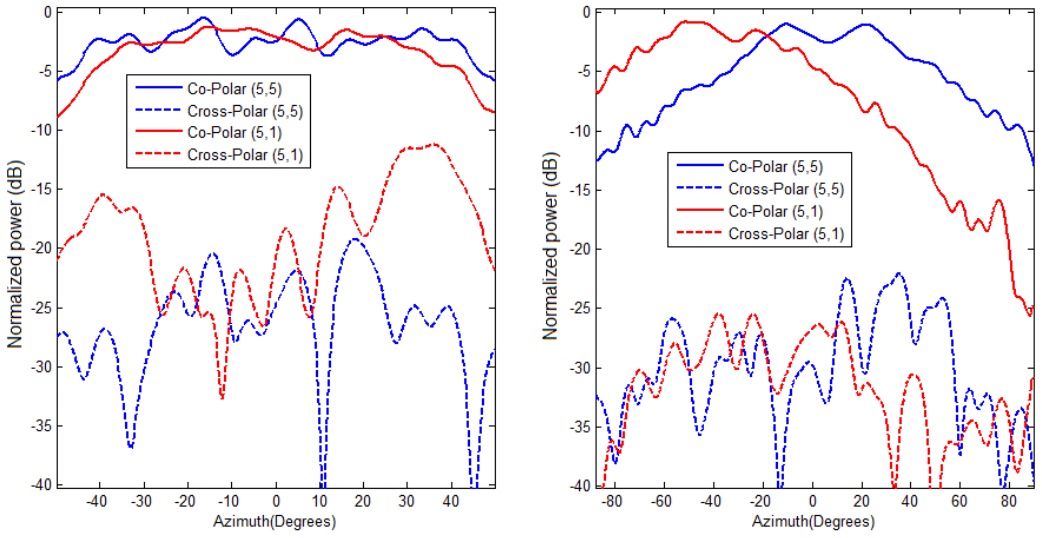

(a) Planar Array

(b) Faceted-Cylindrical Array

FIGURE 4.10: Planar and Faceted-cylindrical phased array antennas Measurement - Azimuth principal plane cut of AEP

The CNFS was used to take the near field measurement of the 64-element cylindrical array with 3 degrees and 0.622inch resolution. At the initial position, the probe is in the middle of XY plane. Then it can move $\sim$ 2.5 feet up and $\sim$ 2.5 feet down. Initially, the middle point of the probe is aligned with the middle point of the (1,1) patch antenna which is located at the upper left corner of the array. The probe-to-azimuth stage radius, an important distance to be measured is the distance between the front of the probe to the axis of the azimuth stage where the AUT is mounted. The accuracy of this measurement should be within a wavelength of the operating frequency or the desired frequency. The AUT will not be able to place on the axis of the azimuth stage. Thereon the distance between axis to the AUT, maximum radial extent (MRE) has to be measured. Even though the accuracy of MRE is not critical, this distance should be entered in the measurement software. In order to increase the elevation range, the probe required modifications. In this near-field chamber, the azimuth stage had no facilities to mount an 8×8 cylindrical array. Therefore a special mounting stage had to be constructed in the lab (Figure 4.9(b)).

The planar and faceted-cylindrical array measurement set up in the near-field

chamber is shown in figure 4.9. In the measurements, the AEPs varied with the location of the element due to the surface currents and edge currents, as presented in figures 4.10. The degradation of AEP's gain in edge elements can be observed in both planer (Figure 4.10(a)) and faceted-cylindrical arrays (Figure 4.10(b)). The number of oscillation of the co-polar pattern can not be observed in a crystal clear manner. Hence the diffraction field from edges of each column. However, in a planar array, AEP has four oscillations, which is half of the number of element in a row or column [104]. In the faceted-cylindrical array, the number of oscillations is lower (two oscillations) than the number of oscillations in planar array case but more intensive oscillations can be observed. EM characterization of a planar and faceted-cylindrical array with more details can be extracted from 3D plots as shown in Figure C.1 and Figure C.2.

4.2.2 Measurement Setups in Far-Field Chamber

In far-field measurement system, the planar wave approximation is made to minimize the size of the facility. In order to make this approximation reasonable and meaningful, two conditions are required to be satisfied. The source antennas and receiving antenna are coupled with separation distance R larger than $2D^2/\lambda$ and D/R should be extensively smaller in comparison with half-power beam width of the source antenna radiation pattern. D is the maximum dimension of receiving aperture. The reflected energy or electromagnetic waves can interfere with the field illuminating from the source antenna or absorbing from the receiving antenna. This interference can destroy the illuminating fields or absorbing fields which lead to the considerable degradation of the measurement accuracy. In order to minimize reflection from a wall and other objects in the chamber, absorbing forms are used to cover every possible area and object of the chamber.

The far-field measurement was done in both RIL old far field chamber and RIL new far field chamber. CPAD-1 measurements were done in the far-field chamber

and according to the nature of the measurement method, Ludwig's third definition of cross polarization [99] can be applied. There is no probe calibration used in old chamber measurement process. The KOUN feed horn antenna has a 35dB cross polar level. Then in the comparison of measurement and simulation, an excellent resemblance of cross pol level can not be identified. As an example in the full-wave simulation pattern, there is a deep null in the cross polarization pattern, but the measurement pattern results generally do not show this null.

4.2.2.1 Measurement Set-up in Old Chamber

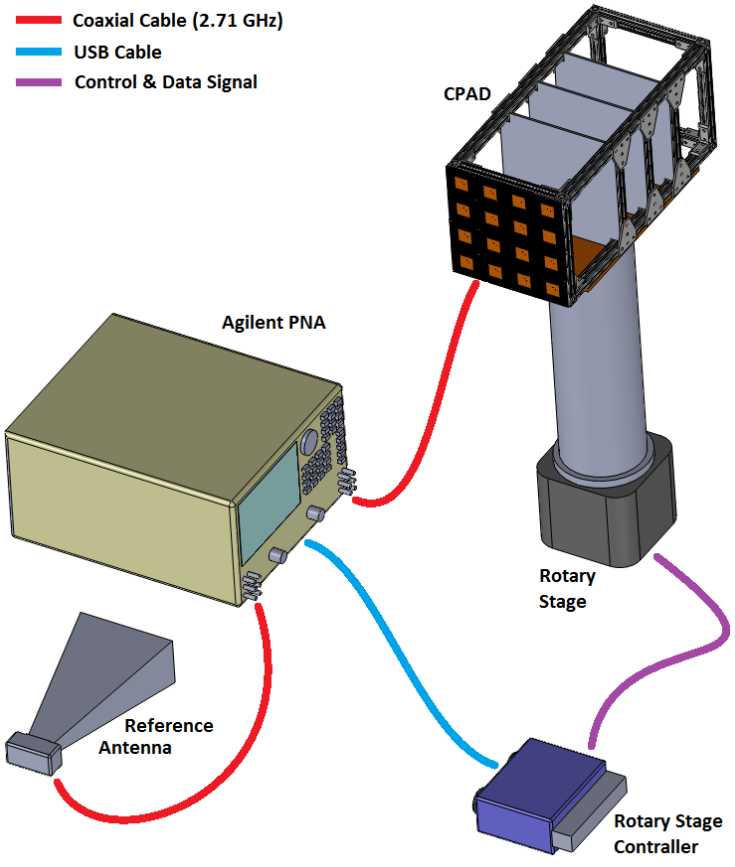

FIGURE 4.11: CPAD-I : Measurement Set Up At 1PP

The measurement of CPAD-I was done in an anechoic chamber located in the One Partner Place on the University Research Campus. This chamber was built by students at ARRC with absorbing forms in a regular office room. As in the figure

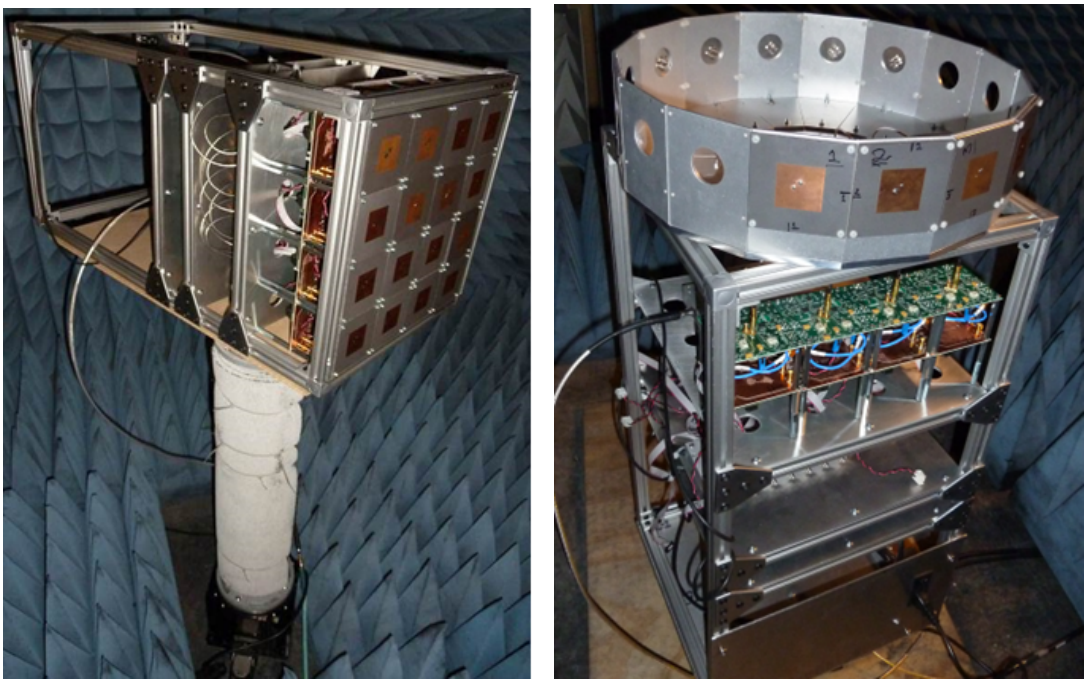

(a) Planar 4 × 4 CPAD-I (b) Circular CPAD-I

FIGURE 4.12: CPAD-I : 2 × 2 Planar Array Antenna Measurement With Mirrored and Regular Configurations

4.11, the test setup has a vector network analyzer (VNA)[1], a positioning system or a rotary stage, rotary stage controller[2], and the dual-polarized KOUN[3].

The CPAD-1 antenna array was mounted on a positioning system as shown in figure 4.12(a) and figure 4.12(b). The rotary stage can position the antenna in an azimuth plane for taking the reading by the VNA. The VNA is the central piece equipment of the measurement set-up. According to the Keysight Technologies antenna test guide, far-field chamber test need number of pieces of equipment such as microwave transmit source, test mixer module, amplifiers, LO/IF distribution unit, routers, hubs, and a computer. In order to reduce the number of pieces, the setup was simplified with the VNA and a script running on it. The VNA accomplished generating the transmitting signal, sending the control signal to the

[1]Agilent®E8364B PNA Network Analyzer has 10 MHz to 50 GHz and 104 dB of dynamic range

[2]Soloist®single-axis digital servo controller are used to control the azimuth (AZ) angle of the positioning system

[3]KOUN is a feed horn antenna of the dual-pol WSR-88D radar system. The Co-Polar and Cross-Polar measurement that was measured by in the same set-up with standard ATM horn antenna in in figure 4.15(a)

rotary stage for incrementing the azimuth position of the CPAD-I, receiving data from CPAD-I and recording the S-parameters for each position. The array with receive-mode and low power (the HPAs were not activated) transmit-mode was measured with this setup. Henceforth the CPAD-I was under measurement as the receive antenna; KOUN feed-horn antenna was connected to the transmitting signal generating port of the PNA. The transmit power was set to $9dBm$, which is the maximum power VNA can generate for this set-up. The microwave signals were transmitted to PNA and receive from PNA via the coaxial cable. The VNA was set to save S parameters with 200 samples between 2700 MHz and 2710 MHz. The S-parameter measurements were stored as PRN files which were processed by a MATLAB program to compute the array pattern.

4.2.2.2 Measurement Set-up in New Chamber

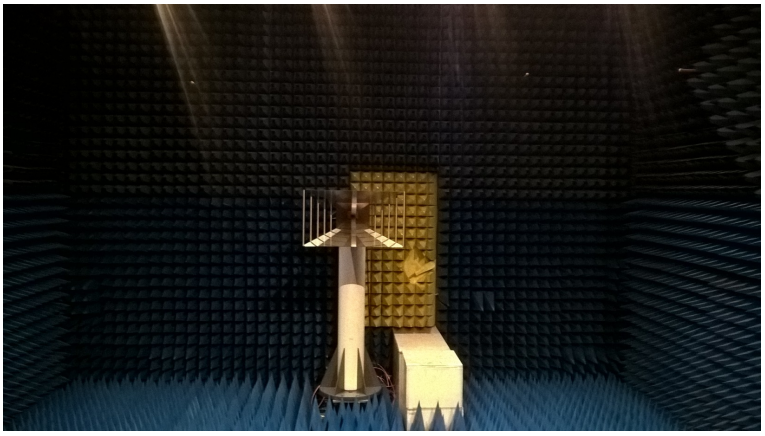

FIGURE 4.13: Far-Field Chamber at RIL

The size of the new far-field chamber located at RIL is 26 feet width, 38 feet long, and 26 feet hight. The probe or range antenna is a dual ridge horn antenna with constant gain of 12dBi from 0.3 to 3.0 GHz frequency range. The cross polarization level of the probe antenna is 45dB below the co-polarization level.

4.2.2.3 Old & New Far-Field Chamber Measurements

The old chamber at One Partner Place was build by ARRC students as a temporary far-field facility. In this section, a comparison of the measurement of KOUN fead horn antenna and NEXRAD feed horn antenna, which are taken in old and new chambers respectively is presented. Figure 4.14(a) show the KOUN fead horn, which was used as the reference antenna of the old chamber. The picture of NEXRAD feed horn, which is under measurement in new chamber can be seen in figure 4.14(b).

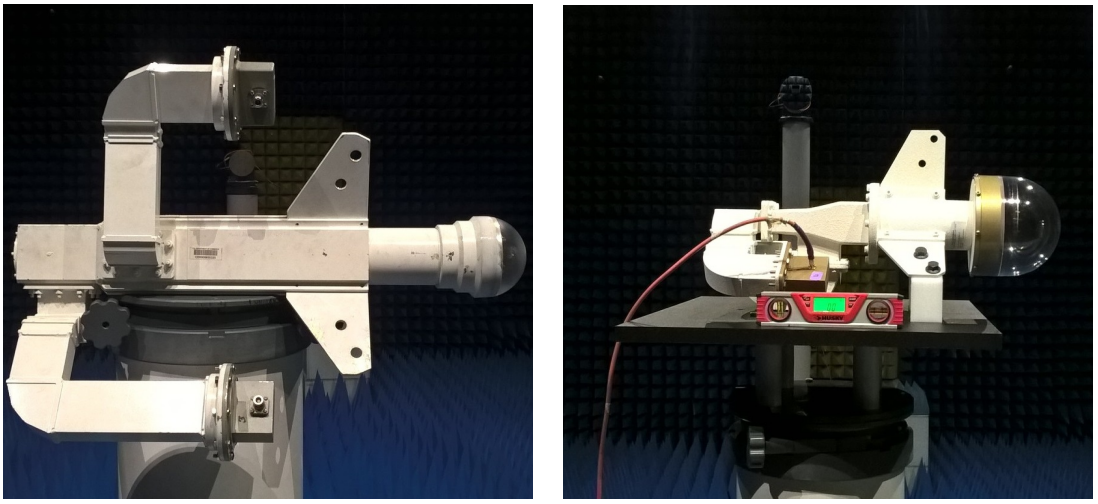

(a) KOUN Feed Horn Antenna (b) NEXRAD Feed Horn Antenna

FIGURE 4.14: NEXRAD and KOUN Feed Horn Antenna

4.3 Data Processing and The Array Pattern Generation Using Active Element Patterns

As near-field data needs to be transformed into far-field data with desired coordinate systems. However, the data processing is crucial in the near field measurement. If the active element patterns of the array are measured, additional data processing is needed to generate the array antenna pattern.

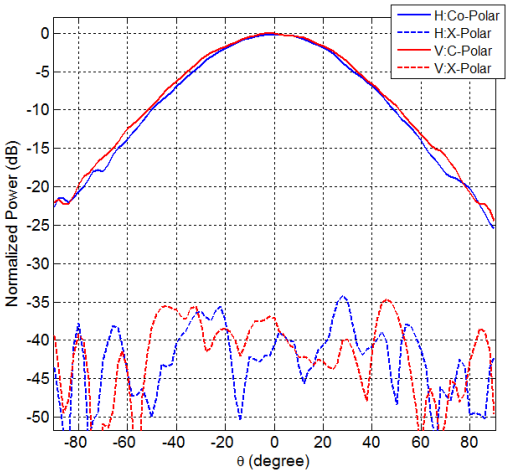

(a) KOUN Feed Horn Antenna

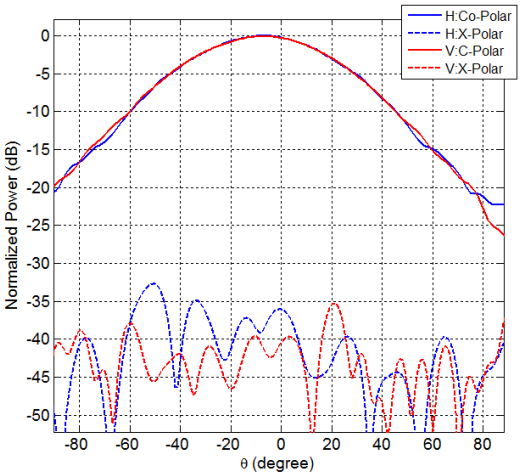

(b) NEXRAD Feed Horn Antenna

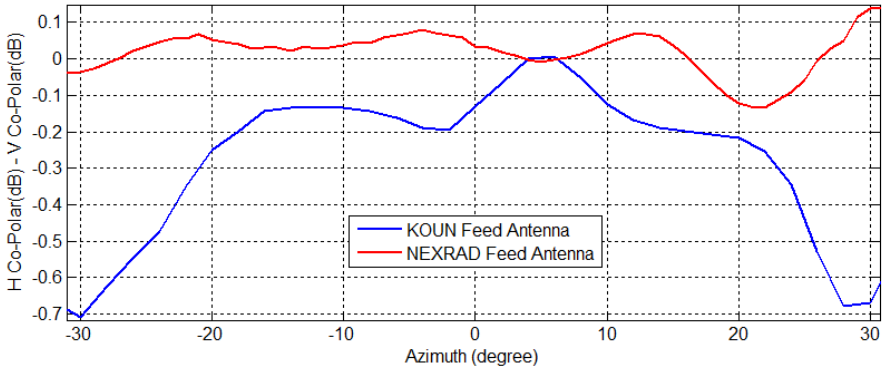

(c) KOUN and NEXRAD Co-Polar Ratios

FIGURE 4.15: NEXRAD(New Far-field Chamber) and KOUN(Old Far-field chamber) Feed Horn Antenna Measurement

4.3.1 Data Processing

After completing the near-field measurement scanning, the NFS software can be used for data processing. Hence the near-to-far field transformation, selecting the coordinate system to do the near-to-far field transformation, resolution of the far field pattern, polarization definition, and interpolation method. NSI 2000 software is able to process near-field row data and produces horizontal and vertical principal plane cuts (H- and V-cuts), 2D intensity view of the pattern using proper coordinate system definition (image), a contour of the image, 3D plots and far-field data (listing).

There are 128 measurements, which has to be taken for planar and cylindrical

array antennas. The manual data processing of each AEP is a laborious process. The ability to automate this job using NSI 2000 software is advantageous in this situation. This automation can be done with a program written in VBScript.

4.3.2 Generation of The Array Pattern Using AEP

The array theory can be used to develop the formula which can calculate an approximate radiation pattern from measured or simulated element pattern : $E(\theta, \phi) = AF \times EP$. AF is the array factor for given antenna array manifold and EP is element pattern measured or simulated in an array environment. In case, we have used the AEP of each elements of the array, we are capable of reading a much better approximation. In this section, the array pattern generation theory for planar and faceted-cylindrical arrays used in this work is discussed and the array patterns are presented.

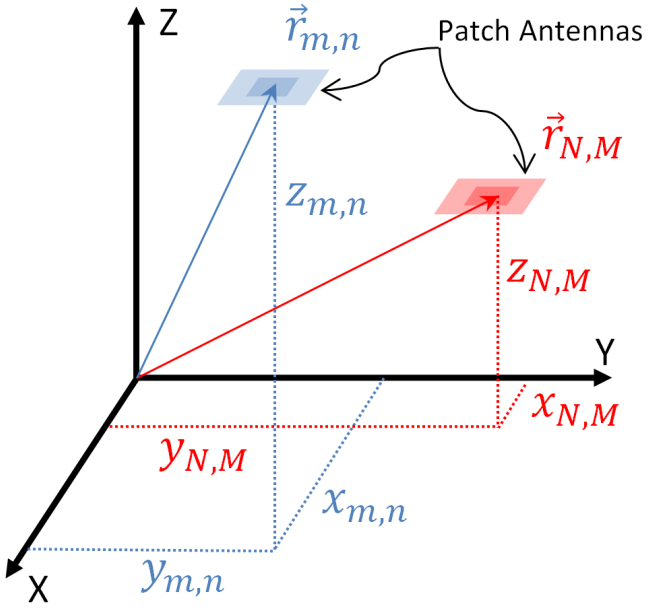

FIGURE 4.16: Array Pattern Generation Theory Illustration

$$E(\theta, \phi) = \sum_{\forall n,m} a_{m,n} c_{m,n} E_{m,n}(\theta, \phi) e^{jk\vec{r}_{m,n}\cdot\hat{r}_{\theta,\phi}} \tag{4.10}$$

Where $E_{m,n}(\theta, \phi)$ is the complex electric field in $\widehat{r}_{\theta,\phi}$ direction, which can be measured or simulated as phase and magnitude of each element's AEP. k is the wave number which is $2\pi/\lambda$. $m \in [-M/2+1, M/2]$ and $n \in [-N/2+1, N/2]$ are positive or negative integers. In this case, M and N are positive even numbers. $a_{m,n}$ is the complex excitation of (m, n) element.

$$a_{m,n} = |a_{m,n}|e^{-jk\overrightarrow{r}_{m,n}\cdot\widehat{r}_{\theta_0,\phi_0}} \tag{4.11}$$

$\widehat{r}_{\theta,\phi}$ is the unit vector in Cartesian coordinate system, which is in the direction of any point in space (r, θ, ϕ).

$$\widehat{r}_{\theta,\phi} = u\widehat{x} + v\widehat{y} + cos\theta\widehat{z} \tag{4.12}$$

u and v are the direction cosines and they are defined as $u = \sin\theta\cos\phi$ and $v = \sin\theta\sin\phi$. θ_0 and ϕ_0 define the beam steering direction.
$c_{m,n}$ is the complex calibration value for each elements. This value can be measured with proper test procedure. In this work, measured AEP could be used to compute the complex calibration value.

$$c_{m,n} = |c_{m,n}|e^{-j\alpha_{m,n}} \tag{4.13}$$

$\overrightarrow{r}_{m,n}$ is the position vector of each element. The measurements of elements are taken individually as far-field patterns (transform the near-field to far-field in near-field scanning system). Then $z_{m,n}$ was taken as zero.

$$\overrightarrow{r}_{m,n} = x_{m,n}\widehat{x} + y_{m,n}\widehat{y} + z_{m,n}\widehat{z} \tag{4.14}$$

In this work, the patch antenna size is $0.56\lambda \times 0.56\lambda$. Therefore let $d = 0.56\lambda$ in the planar and faceted-cylindrical array pattern generation.

4.3.2.1 Planar Array

Since the elements of planar array is arranged on XY plane, the determination of $\vec{r}_{m,n}$ is very intuitive with simple geometry. Let the number of elements $2M \times 2N$, where M and N are integers. When $m \in [-M+1, M]$ and $n \in [-N+1, N]$ the $x_{m,n}$, $y_{m,n}$, and $z_{m,n}$ can be determined as below.

$$x_{m,n} = d(2n-1)/2 \tag{4.15a}$$

$$y_{m,n} = d(2m-1)/2 \tag{4.15b}$$

$$z_{m,n} = 0 \tag{4.15c}$$

let the number of elements $(2M+1) \times (2N+1)$, where M and N are integers. When $m \in [-M, M]$ and $n \in [-N, N]$ the $x_{m,n}$, $y_{m,n}$, and $z_{m,n}$ can be determined as below.

$$x_{m,n} = dn \tag{4.16a}$$

$$y_{m,n} = dm \tag{4.16b}$$

$$z_{m,n} = 0 \tag{4.16c}$$

4.3.2.2 Faceted-Cylindrical Array

$x_{m,n}$, $y_{m,n}$, and $z_{m,n}$ can be computed using below equations, which are derived with geometrical information of a general faceted-cylindrical array with even number of elements in rows and columns.

$$x_{m,n} = \frac{d}{2}\left(\sin\frac{(2n-1)\Delta_\xi}{2}\cot\frac{\Delta_\xi}{2}\right)$$

$$y_{m,n} = (2m-1)\frac{d}{2}$$

$$z_{m,n} = -\frac{d}{2}\left(\csc\frac{\Delta_\xi}{2} - \cos\frac{(2n-1)\Delta_\xi}{2}\cot\frac{\Delta_\xi}{2}\right)$$

The generated planar phased and faceted-cylindrical array pattern using 64 AEPs for the H channel (horizontal polarization) is shown in figure 5.8 and 5.9 respectively. In the same manner, radiation pattern can be generated for the V channel using AEPs for V channels in both cases of planar array and faceted-cylindrical array.

Chapter 5

Lab-Scale, Reconfigurable Testbed Systems

In this chapter, the measurement procedures and some of the measurements taken in the Far-Field and Near-Field chamber facilities located at Radar Innovation Laboratory (RIL) are presented. Different isolated antenna elements, embedded elements, and phased arrays were measured using the near-field and far-field technique. A low-cost, small-scale testbed for the dual-polarized array antenna - the Configurable Phased Array Demonstrator (CPAD) was developed for the prototyping and educational purposes. In order to study the effect on antenna characteristics, this sixteen-element array with a beam-forming network (TR modules and power combiner/divider) could be configured into different antenna manifold (4×4 planar array, eight-element ring array, and 2×2 arrays with a mirrored orientation of element's configurations). The primary purpose of the measurements taken using CPAD-I is to investigate as to how the array manifold configurations affect the polarimetric array radiation pattern. Therefore all the elements (up to 16 elements) were excited with proper phase shiftings and attenuations to study the side-lobe levels, cross-polarizations, and beam steering performances. The investigation of active element patterns and generation of array patterns using active element patterns were done using CPAD-II, which is a 64-element (8×8)

array. The CPAD-II could essentially be configured into 8×8 planar and faceted-cylindrical array antennas to study the polarimetric characteristics of each array manifolds.

5.1 Concept of Configurable Phased Array Demonstrator (CPAD)

In the early works of Multi-functional Phased Array Radar research at Radar Innovations Laboratory, a phased array test bed was created with the participation of graduate research assistants. The test bed was called Configurable Phased Array Demonstrator (CPAD), comprised of 16 dual channel patch antennas, TR modules, and power divider/combiner (Figure 5.1). In this section, early CPAD works are to be presented briefly. Those works have already been published in both journal and conference papers [105–107]. The operating frequency was 2.705 GHz with 1.45% very narrow bandwidth. Nonetheless, S-band is more preferred frequency band in a radar system for weather measurement, 2.705GHz was selected. In order to make the system low-cost, narrow band simple dual-polarized microstrip patch antenna was used, despite the fact that CPAD front end hardware was capable of handling up to 8% of the frequency bandwidth of 2.8GHz center frequency.

The circuitry and systems for H channel and V channel were designed to have identical electrical characteristics. Each TR module of the CPAD-I had a variable phase shifter and variable attenuator in a common signal path for both transmitting and receiving channel's circuitry. A low noise amplifier (LNA), limiter, and filter were installed on receiving signal path of the microwave circuit. A power amplifier (PA) was designed to boost the transmitting signal up to 44dBm. This PA was fabricated on a separate board as CPAD was in the initial stage of designing and each functionality requires to be well designed and tested before designing one PCB for whole TR module. In addition, any EMC issue and possible heat transfer

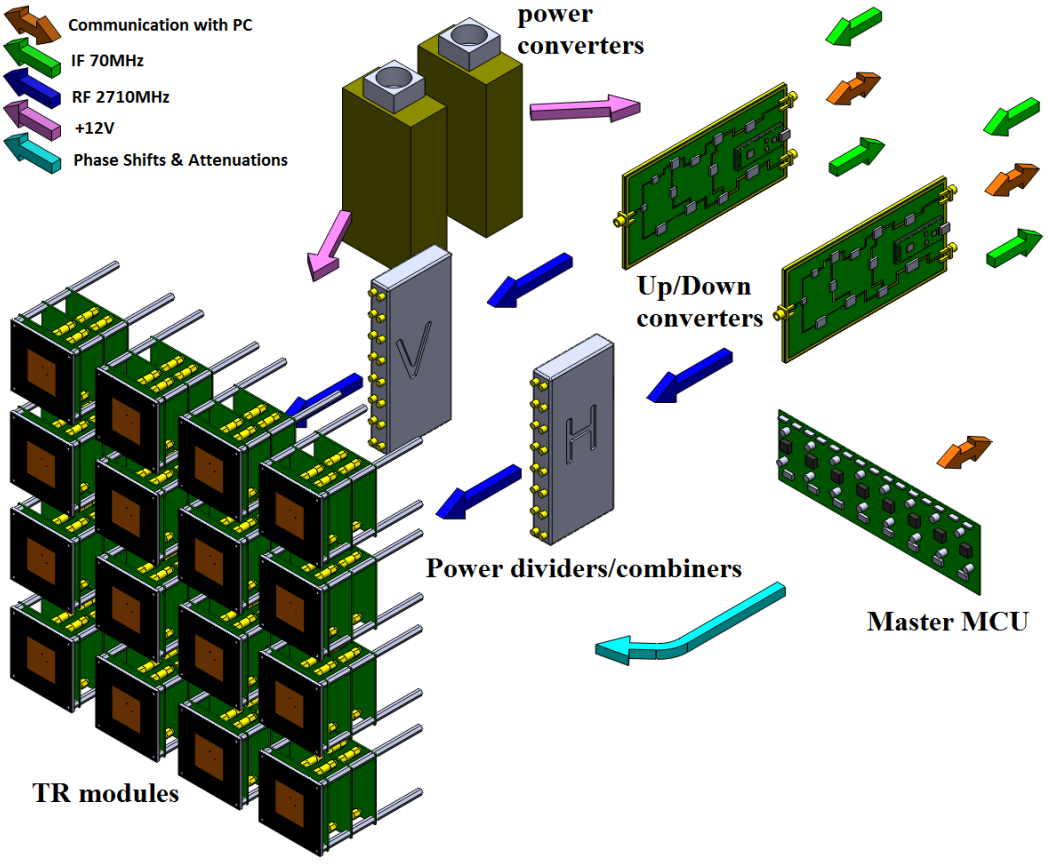

FIGURE 5.1: CPAD-I Concept

to the rest of the TR module would have been avoided. Four PCB boards (TRM, two PA, and MCU) with the microstrip patch antenna were integrated into one module, which can easily fit into different manifold structures. An extensive detail of the development of the TR module was published in [107]. Each TR module had a microcontroller unit (MCU), which was to be programmed to control the phase shift and attenuation of each polarimetric channel. The MCU in each TR module were running a program (slave program) in accordance with the command sent through a serial peripheral interface (SPI) by the master program running on master MCU board. An external global triggering/control signal was able to control and synchronize the TR switches, LNAs, preamplifiers, HPAs, and MCUs in TR modules with 5% duty cycle.

The signal from particular direction was received through all TR modules and combined coherently in power divider/combiner and delivered to up/down converter

or measurement equipment (VNA or Oscilloscope). When the CPAD was transmitting, a signal from up/down converter or equipment was subjected to split into identical signals and delivered to each TR modules. The power divider/splitters for each H and V channel accomplished this functionality. The power converters supplied $28V$ DC power converted from 110V 60Hz AC and it was the only power source to the whole system. A LabVIEW program with a simple graphic user interface (GUI) was implemented to communicate with master MCU to control the phased shifting and attenuation of each TR module individually.

5.2 CPAD-I : 16-Elements Planar Subarray

In this demonstration, CPAD-I, in which elements are regularly separated by 0.7λ spacing was configured as an 4×4 array for planar array measurements with beam steering and amplitude tapering for beam forming with low side-lobe level. The measured radiation pattern and simulation of planar 4×4 antenna array patterns for different beam steering directions are presented in figure 5.2. Figure 5.2(a), 5.2(b), 5.2(c), and 5.2(d) show the variation of array pattern with the variation of the beam steering of 0°, 10°, 20°, and 30°. These patterns were measured with uniform tapering (0dB attenuation in all the channels). Measured co-polarization (Co) and cross-polarization (X) patterns are plotted with the simulated patterns, which are having a good agreement.

The attenuation of each element of 4×4 planar array can be determined to get the minimum side lobe level. There are many techniques which can accomplish the amplitude tapering for sidelobe level reduction. In this measurement, the particle swarm optimization method[108] -a nonlinear optimization procedure was used to compute the attenuation of each element. The antenna elements were grouped into three regions as presented in Table 5.1, because they had equal attenuation. The elements (2,2), (2,3), (3,2), and (3,3) (region 1) were the middle four elements of the 4 array with no attenuation. The elements at the edges without corner

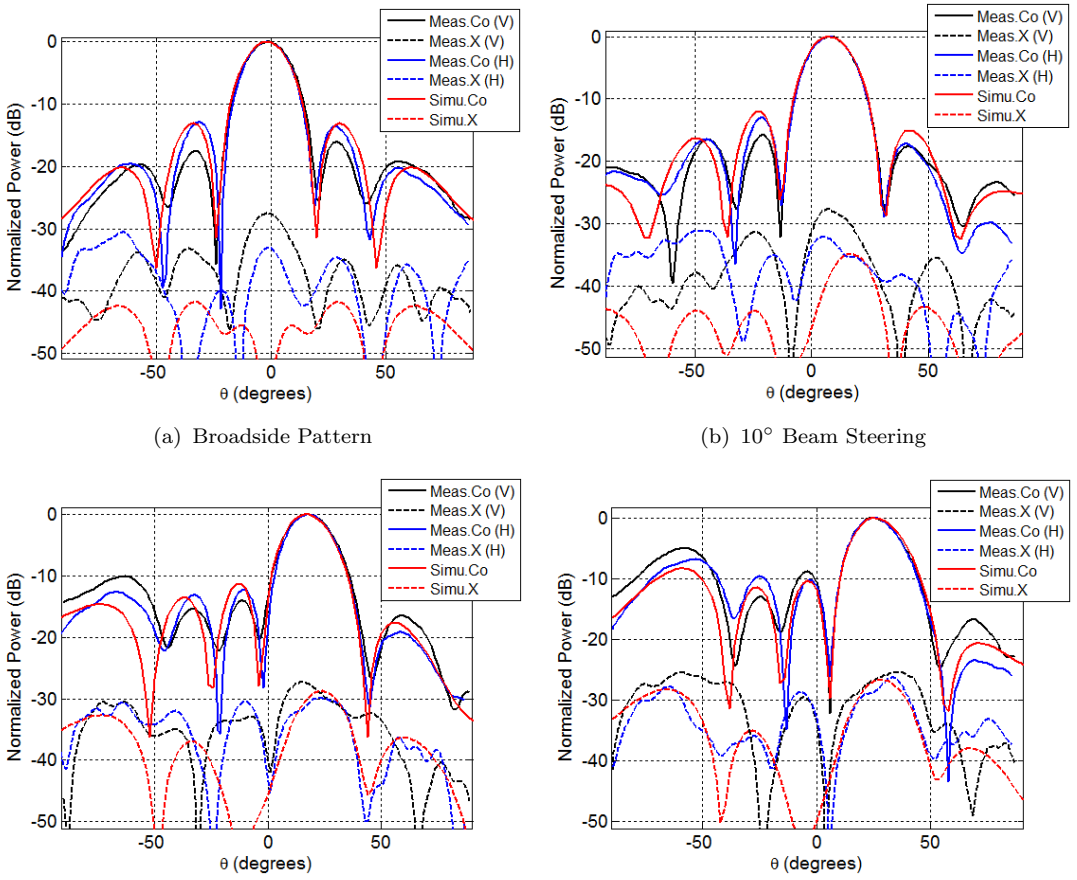

(a) Broadside Pattern

(b) 10° Beam Steering

(c) 20° Beam Steering

(d) 30° Beam Steering

FIGURE 5.2: CPAD-I : 4×4 Array Antenna Measurement with uniform illumination

elements (region 2) were having 5dB attenuation. The elements at corners (region 3) were set with 15dB attenuation. The tapering for achieving a minimum sidelobe level for the array was computed only for the broadband pattern. However that tapering was used in beam steering pattern measurements. The low side-lobe level which is 20 dB lower than the main beam could be achieved in the broadside pattern of this 4 array. Hence the attenuators are capable of introducing quantized attenuation in the receiving or transmitting signal path of a TR module, there are minor differences between computed attenuations and the attenuation that was set in the system. The measurements of H and V channels with the comparison of simulated data can be seen in Figure 5.3. Figure 5.3(a), 5.3(b), 5.3(c), 5.3(d), and 5.3(e) show the variation of array pattern with the variation of the beam steering

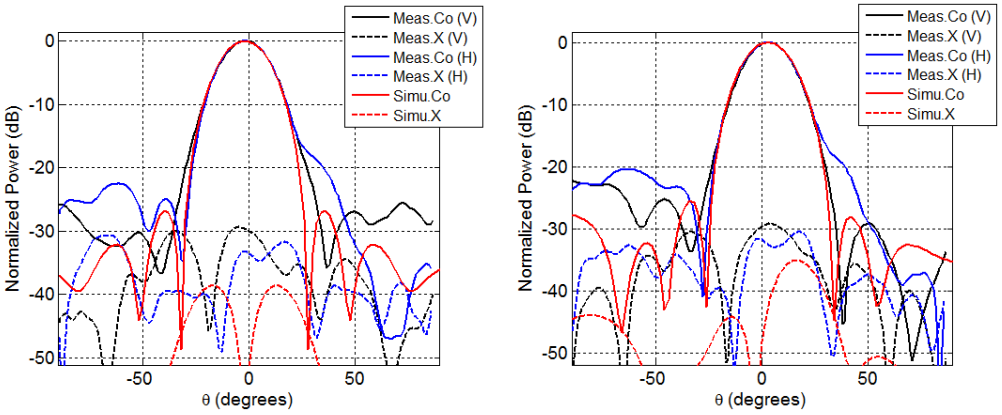

(a) Broadside Pattern

(b) 5° Beam Steering

(c) 10° Beam Steering

(d) 15° Beam Steering

(e) 20° Beam Steering

FIGURE 5.3: CPAD-I : 4×4 Array Antenna Measurement With Tapering of 0°, 5°, 10°, 15°, and 20°.

Region	Element labels	Attenuation (Theory)	Attenuation (Real)
1	(2,2), (2,3), (3,2), (3,3)	0dB	0dB
2	(1,2), (1,3), (2,1), (3,1), (4,2), (4,3), (2,4), (3,4)	5dB	5.18dB
3	(1,1), (1,4), (4,1), (4,4)	15dB	14.48dB

TABLE 5.1: Three regions of the antenna elements distribution on the 4×4 array.

5.3 CPAD-I : 4-Elements Planar Mirrored Array Configuration

This demonstration was used to show the orientation of radiating elements, which can effect on the improvement of cross polarization level of the array radiation. The mirrored configuration of each element's orientation in an array has been studied by some researchers [109, 110] and validated as a possible method for reducing cross-polarization levels. In addition to the reduction of cross-polarization level, undesired sidelobes can be avoided using this configuration of elements in an array [109]. The comparison of array patterns with radiating elements arranged in regular (all in the same orientation) and mirrored element configuration is presented for both H and V channel in figure 5.4. The measurements and simulation agree that there is some improvement of cross-polarization level around broadside.

5.4 CPAD-I : 16-Element Ring Array with the Excitation of Four and Eight Elements

As the first conformal array demonstration of CPAD, a full circular array with sixteen elements, which were equally spaced along the periphery of the ring was built with 16 TR modules. The illuminated set of successive elements is called the active sector of the full circular ring array. The different sizes of active sectors in a ring array have to be measured to demonstrate the effect of curvature on

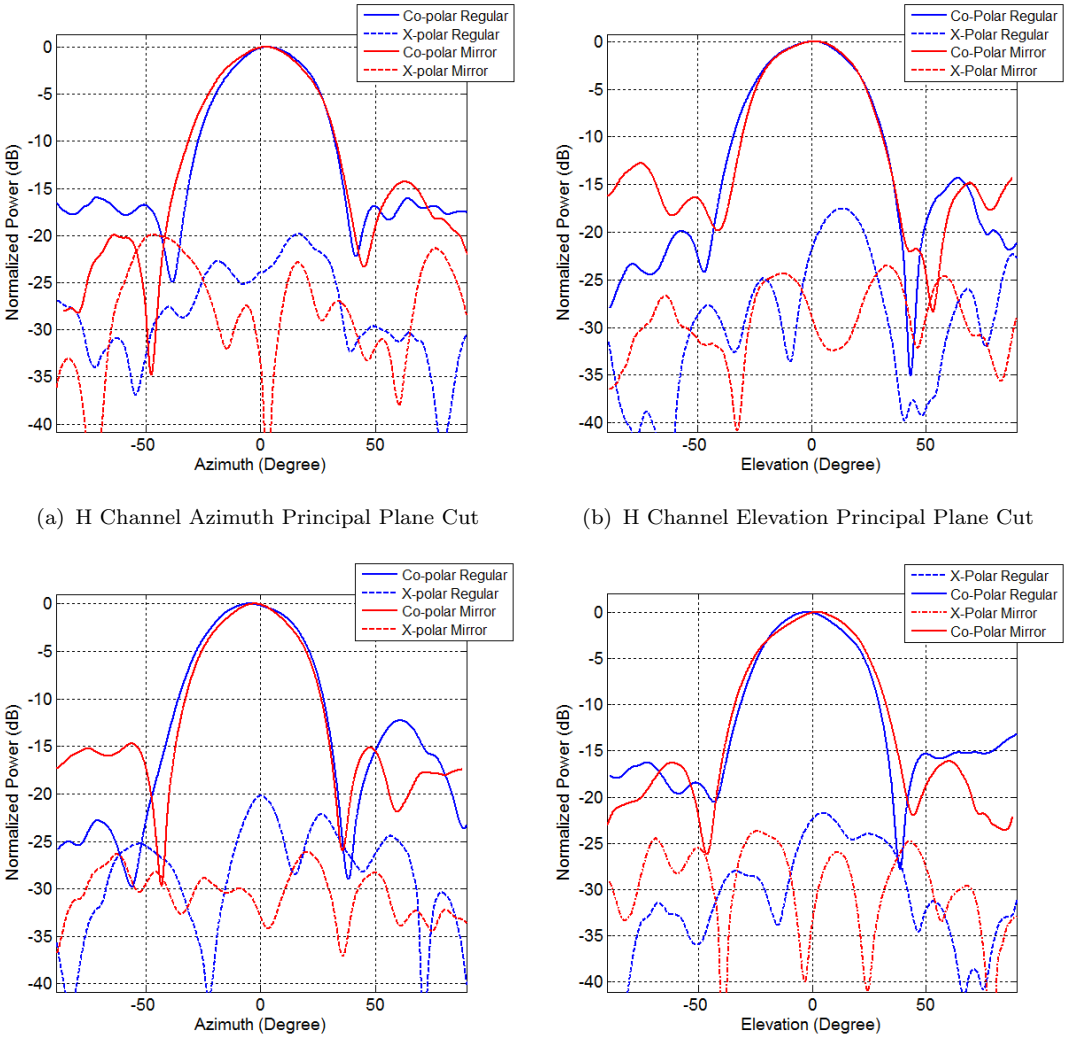

(a) H Channel Azimuth Principal Plane Cut

(b) H Channel Elevation Principal Plane Cut

(c) V Channel Azimuth Principal Plane Cut

(d) V Channel Elevation Principal Plane Cut

FIGURE 5.4: CPAD-I : 2×2 Planar Array Antenna Measurement With Mirrored and Regular Configurations

radiation characteristics of the focused beam. Then a four-element and an eight-element active sector of the ring were excited with proper phase shifting to form a focused beam and measured the radiation pattern using far-field measurement technique. The radius of the ring array was 1.736λ where the λ is 110 mm for 2.705GHz center frequency.

The ring array antenna with excitation of 4-element was measured and simulated for gathering radiation pattern with 0° (Figure 5.5(a)), 10° (Figure 5.5(b)), 20° (Figure 5.5(c)), and 30° (Figure 5.5(d)) beam steering (Figure 5.5). The lobes at $-90°$ and 90° are lower than the case of 8 element active sector array.

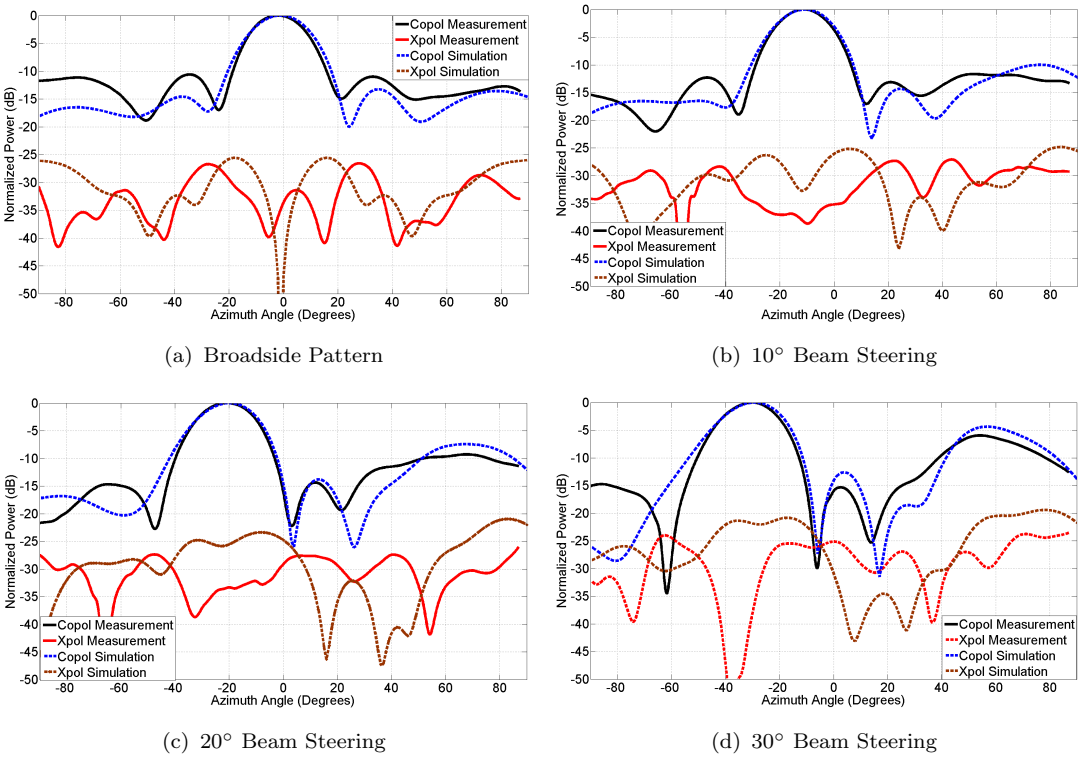

(a) Broadside Pattern

(b) 10° Beam Steering

(c) 20° Beam Steering

(d) 30° Beam Steering

FIGURE 5.5: CPAD-I : Measurements of 4-element active sector ring

The measurement and simulation of ring array antenna with excitation of 8-element were done for three steering beam in 0° (Figure 5.6(a)), 5° (Figure 5.6(b)), and 10° (Figure 5.6(c)) directions (figure 5.6). The lobes at $-90°$ and 90° are more apparent in this case.

The important fact, that the curvature of a faceted ring array creates lobes at $-90°$ and $+90°$ location can be verified by observing this ring array radiation characteristic. The same phenomenon can be observed in the faceted-cylindrical array measurements in Section 5.6. This was a very small ring array with 16 elements, therefore one element occupied 22.5° at the center of the ring. The commutating scanning is the method used in a large cylindrical array with 100λ diameter. One can use CPAD-1 in a radar system and implement a commutating scanning scheme with very low resolution. In addition, the investigation of fundamental properties of a faceted ring array manifold and compared the characteristics of a planar array could be done with measurement of steered beams.

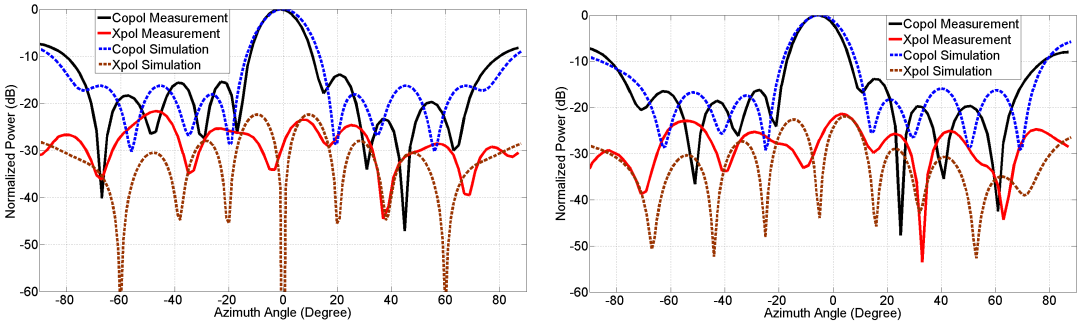

(a) Broadside Pattern

(b) 5° Beam Steering

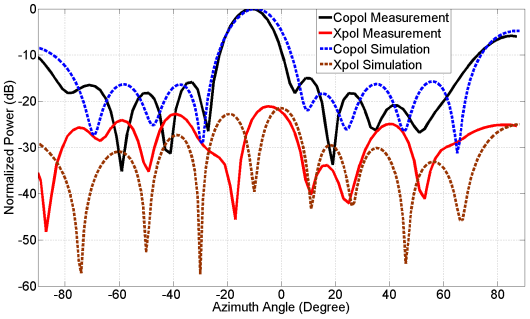

(c) 10° Beam Steering

FIGURE 5.6: CPAD-I : Measurements of 8-element active sector ring

5.5 CPAD-II : 64-Elements Planar Array Antenna

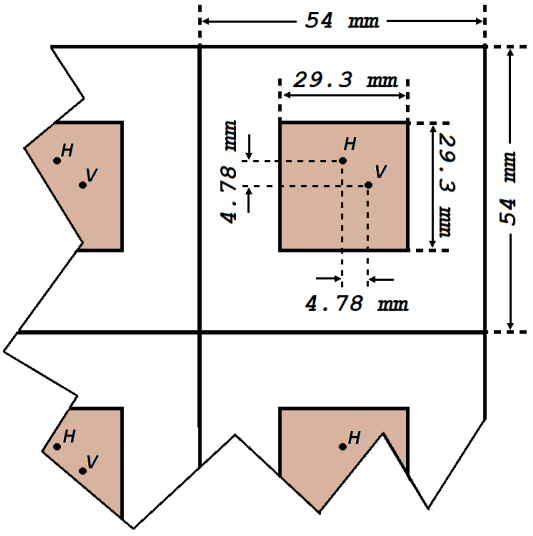

FIGURE 5.7: CPAD-II Array Antenna Specification

The patch antenna (Figure 5.7) was fabricated on RT/Duroid 5880 with 1.575 mm thickness and 1/2 oz copper cladding. The operating frequency was selected in

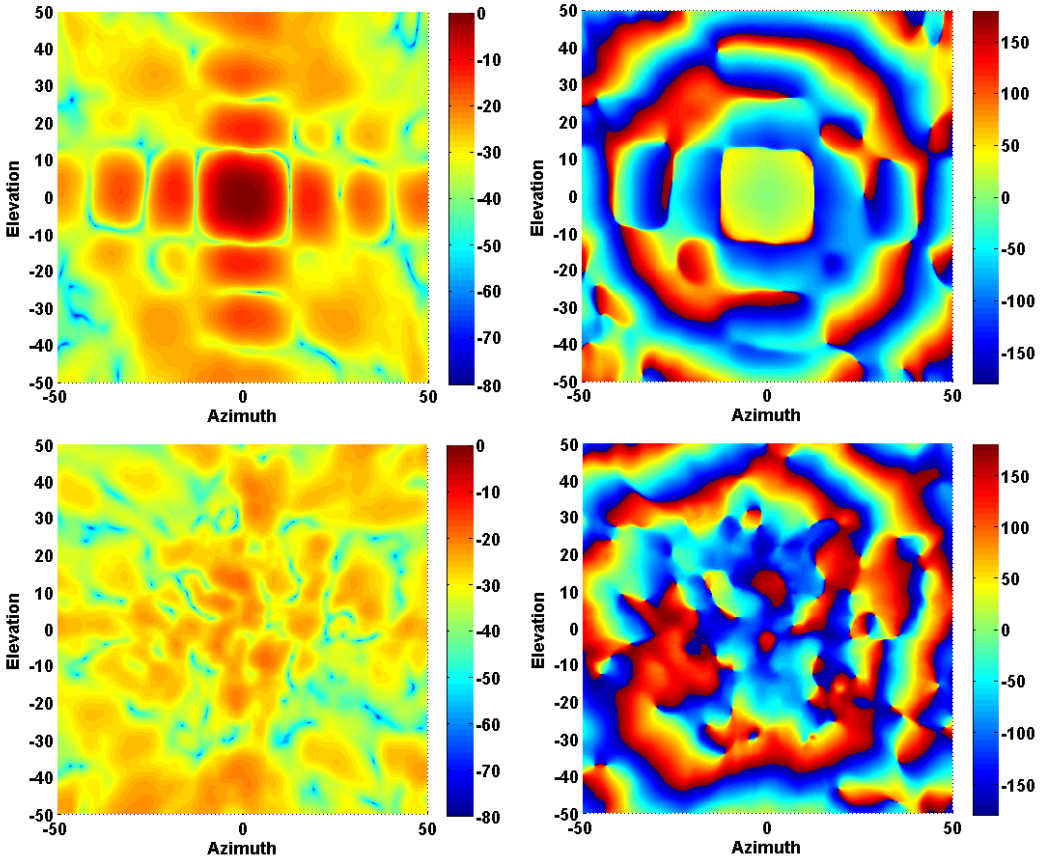

FIGURE 5.8: CPAD-II Planar Antenna Measurement - Radiation Patterns

S-band. The patch antennas are dual polarized single layer elements with 0.56λ size.

The average directivities of AEPs were $9.81dB$ and $9.98dB$ at $3.1GHz$ for H and V channel respectively. The S-band rectangular waveguide was utilized as the probe antenna. OEWG WR284 probe model in $[2.6GHz, 3.96GHz]$ frequency band was used for the probe correction. The near-field scanner is $5ft$ high and can measure $[-50°, +50°]$ in both Azimuth range and Elevation range. The co-polarization and cross polarization active element patterns of elements (4,1), (4,2), (4,3), and (4,4) are shown in figure C.1(a), C.1(b), C.1(c), and C.1(d) respectively. The cross-polarization level was around $15dB$ below the maximum of co-polarization level. 64-element were measured for both H and V channel to generate the radiation pattern of the planar array as shown in Figure 5.8, which shows H channel amplitude and phase patterns for co-polarization and cross-polarization. A similar pattern

for V channel can be obtained using the same procedure. The radiation pattern of array beam steering ($\theta = 20^\circ$ and $\phi = 40^\circ$) can be seen in Figure C.3.

5.6 CPAD-II : 64-Elements Cylindrical Array Antenna

The average directivities of AEPs were $10.50dB$ and $10.46dB$ at $3.1GHz$ for H and V channel respectively. The probe model was the same as the model used for planar array measurements. The azimuth range was $[-90^\circ, +90^\circ]$ and the elevation range was $[-32^\circ, +32^\circ]$. An 8×8 array with 3.32λ radius array was measured using near-field scanning. The co-polarization and cross-polarization of active elements (4,1), (4,2), (4,3), and (4,4) are shown in figure C.2(a), C.2(b), C.2(c), and C.2(d) respectively. The cross-polarization level was around $25dB$ below the maximum of co-polarization level. The AEPs in this measurement were slightly more directive than the planar array measurements of AEPs. As in the case of planar array, the radiation pattern of the faceted-cylindrical array can be generated using AEPs (shown in Figure 5.9). The radiation pattern of array beam steering ($\theta = 20^\circ$ and $\phi = 40^\circ$) can be seen in Figure C.4.

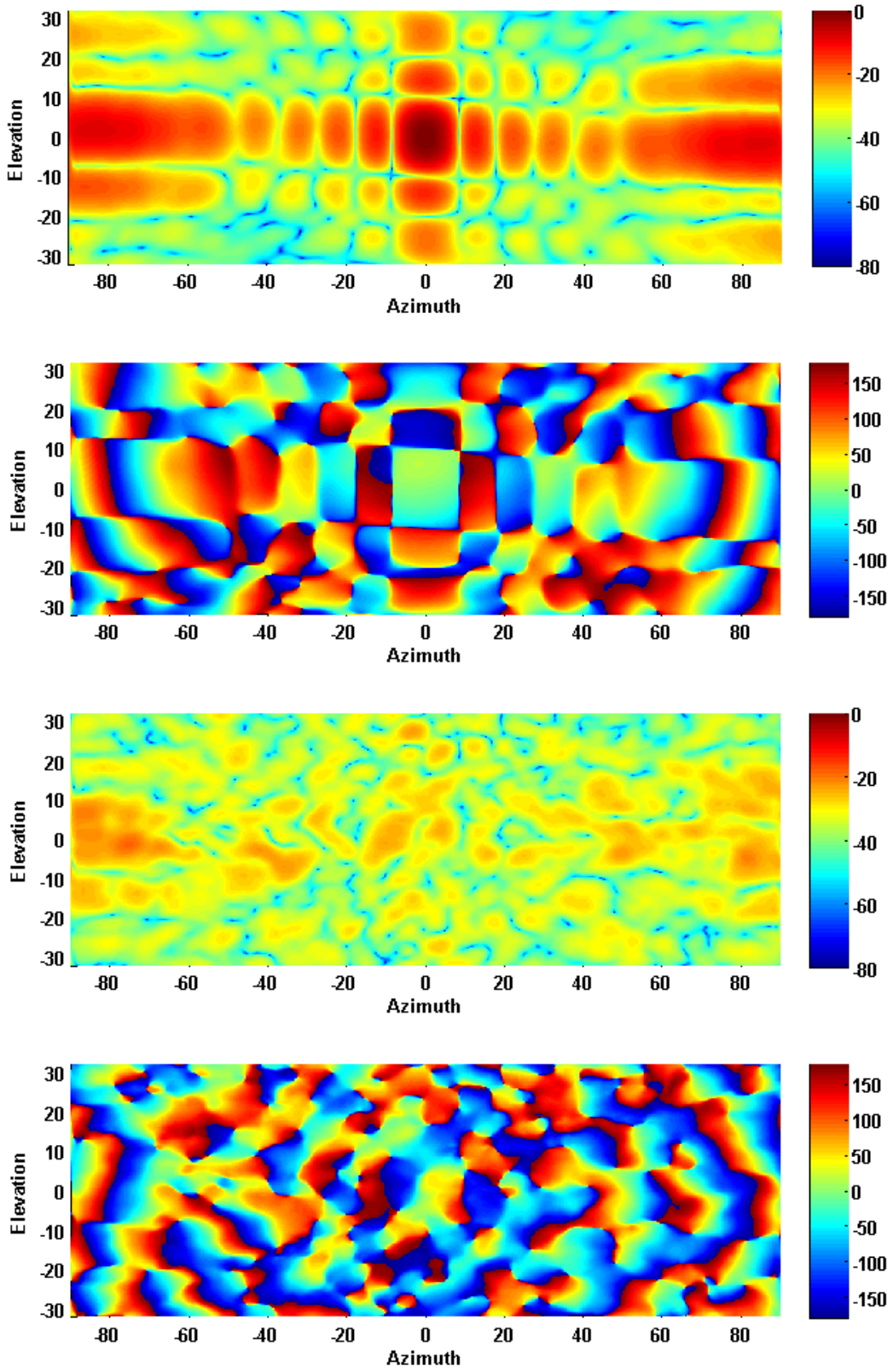

FIGURE 5.9: CPAD-II Cylindrical Antenna Measurement - Radiation Patterns

Chapter 6

Scalable Finite Array Antenna Simulation and Validation

The element-by-element approach [111] and infinite periodic structure approach [112] are the oldest methods that were used to analyze finite arrays. In element-by-element method, mutual impedance or admittance at each couple of elements is calculated. That mutual coupling information can be used to construct a matrix equation. Element currents of each element can be computed for any excitation by solving this matrix equation. In the 1960s, array pattern based on an electromagnetic characterization of one element in the infinite array had been considered an accurate analysis of any element in a large array. Therefore in infinite periodic structure approach, one element with periodic boundary was analyzed and calculated the finite array pattern by multiplying it with array factor. The study of infinite arrays was done by researchers based on a model theory by Farrell, Kuhn, Knittel, Hessel, and Oliner [113, 114]. But today, this kind of analysis will be acceptable at the level of preliminary designing. The real world arrays have a finite number of elements, and the final designing should be based on the proper analysis and simulation of a finite array. Numerous research works have been published on the investigations of computationally efficient methods for making a reasonably accurate prediction to an electromagnetic characterization of the massive finite

phased array antennas.

The Fourier windowing method [115] was used by Ishimaru, Coe, Miller, Green, Skrivervik, Mosig, Roscoe, and Perrott in their investigation of finite periodic structures [116] and finite phased array antennas [117, 118]. This method is based on Poissons sum formula (or Greens function) and spatial Fourier transform. This method can include reasonable effects of a finite array such as edge current. In addition to that, the analyzing issues of non-uniform array element spacing can be addressed using this method. The amount of required computational power is independent of the size of the array being analyzed using this method. The assumption of infinite periodic structure approach is still used in this method. Hansen investigated finite array scan impedance using Gibbsian Model [119, 120]. In this method, standing waves which were similar to Gibbsian oscillations were used to approximate the oscillations in scan impedance of each radiating element of a finite array antenna. Tomasic [121] analyzed a finite array using the approximate solution to a Fredholm integral equation, which was derived by assuming global array concept. The approximation solution to this single Fredholm-type integral equation of the second kind was generated using equivalent infinite array scattering parameters and mutual admittances. The radiation patterns of a finite array were obtained using a method based on Floquet Modal by Bhattacharyya [122, 123]. The electric and magnetic fields on the surface of all the apertures of array elements were produced by Floquet Modal when an element of the array was excited. Then Surface Equivalence Theorem can be used to compute the AEP of an element excited. Array Decomposition Method (ADM) [124, 125] which is based on the Fast Multipole Method (FMM) [126] were proposed to analyze finite array antenna by using Toeplitz property of the Green's function. The multipole expansion can reduce the storage required in the simulation. Mutual impedance between array elements was analyzed using Floquet Model [127] for a finite array with arbitrary amplitude and phase distributions.

This is the summarization of well-known algorithms and procedures proposed in

the literature. FDTD method with PBC can be used to model a good simulator to simulate AEP and S-parameters of an infinite array. Then the well known traditional methods for pattern prediction for small array (element-by-element method) and large array (infinite array method) can be simulated to obtain the preliminary solution. Very large array analysis, which uses only infinite array methods will neglect the edge currents. Then low side-lobe designing will not be done using only FDTD method with PBC. In this chapter, two novel approaches are presented to compute the far-field power pattern of an arbitrarily large array with the consumption of same computational resources. Both schemes are based on the FDTD method and PBC. Both methods are validated with measurement and simulation (HFSS).

6.1 Goals and Requirements

According to the literature review of finite array analysis, the method developed so far is based on element-by-element approach and infinite periodic structure approach. The infinite periodic structure approach has many variances by using techniques to predict the electromagnetic characterization of edge elements using an infinite array element. These are approximated analyzing methods, which may not necessarily be the same as the actual behaviors of the edge elements. The goal in the proposed new model is to model the more accurate electromagnetic effect of edge elements on the finite array. The model should be able to simulate on reasonably high performing computers.

6.2 The Basic Theory and Technique

In addition to the FDTD method and periodic boundary condition, the new finite array method employed few other theories and models. The maximum reactive near-field region of a very large array is discussed as it will determine the computer

memory storage and processing time. Surface Equivalence Theorem is used to convert the problem into a simple equivalent problem, then transformation of near-field to far-field will be carried out to calculate the far-field electric and magnetic field components.

6.2.1 Far-Field, Radiating Near-Field, and Reactive Near-Field Regions

All the electromagnetic problems discussed so far in this dissertation are radiation of electromagnetic waves at far-field. The far-field can be roughly defined as a very large distance relative to $\frac{\lambda}{2\pi}$ [128]. More appropriate discrimination of far-field, radiating near-field and reactive near-field regions for large arrays are defined with simple inequalities as given below. These inequalities are valid for antennas with aperture (D) larger than 2.5λ [128–130].

$$\text{Reactive Near-Field } \Rightarrow \ 0 < r < 0.62\sqrt{\frac{D^3}{\lambda}} \tag{6.1a}$$

$$\text{Radiating Near-Field } \Rightarrow \ 0.62\sqrt{\frac{D^3}{\lambda}} < r < \frac{2D^2}{\lambda} \tag{6.1b}$$

$$\text{Far-Field } \Rightarrow \ \frac{2D^2}{\lambda} < r < \infty \tag{6.1c}$$

6.2.2 Surface Equivalence Theorem

Surface Equivalence Theorem [131] or a more rigorous form Huygenss principle [132] is the fundamental physical theory of the near-field to far-field transformation, which will be discussed in section 6.2.3. The fundamental idea of this theorem is to replace the complex geometrical details and excitations in a closed surface with fictitious electric and magnetic current elements on the closed surface. These surface current densities can be used to determine the far-field component. So this method will reduce the complexity of the original problem and equivalent problem saves memory and CPU time substantially. There are four forms of equivalent

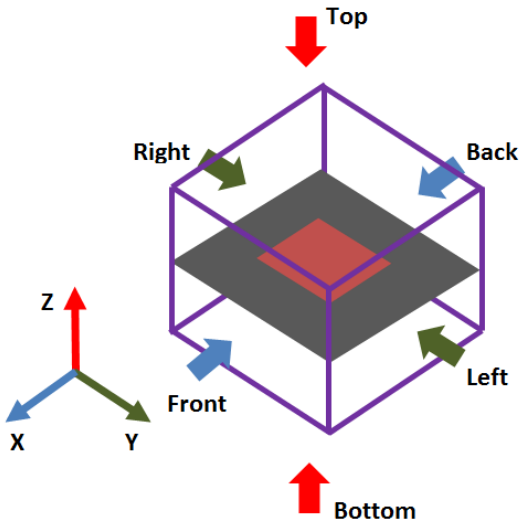

FIGURE 6.1: An imaginary surface enclosing the patch antennas

problem exist depending on the nature of the current densities on the surface and the field inside the close surface [129]. In near-field to far-field transformation, electric and magnetic current densities are calculated and electric and magnetic field components inside the close surface are zero. Surface Equivalence Theorem with this particulate equivalent problem called *Love's theorem*. The surface current components on each surface of the imaginary box can be calculated as in equation 6.2 as presented in [53].

$$\text{Top} \Rightarrow J_x\hat{x} + J_y\hat{y} = -H_y\hat{x} + H_x\hat{y} \text{ and } M_x\hat{x} + M_y\hat{y} = E_y\hat{x} - E_x\hat{y} \tag{6.2a}$$

$$\text{Bottem} \Rightarrow J_x\hat{x} + J_y\hat{y} = H_y\hat{x} - H_x\hat{y} \text{ and } M_x\hat{x} + M_y\hat{y} = -E_y\hat{x} + E_x\hat{y} \tag{6.2b}$$

$$\text{Left} \Rightarrow J_x\hat{x} + J_z\hat{z} = -H_z\hat{x} + H_x\hat{z} \text{ and } M_x\hat{x} + M_z\hat{z} = E_z\hat{x} - E_x\hat{z} \tag{6.2c}$$

$$\text{Right} \Rightarrow J_x\hat{x} + J_z\hat{z} = H_z\hat{x} - H_x\hat{z} \text{ and } M_x\hat{x} + M_z\hat{z} = -E_z\hat{x} + E_x\hat{z} \tag{6.2d}$$

$$\text{Front} \Rightarrow J_y\hat{y} + J_z\hat{z} = -H_z\hat{y} + H_y\hat{z} \text{ and } M_y\hat{y} + M_z\hat{z} = E_z\hat{y} - E_y\hat{z} \tag{6.2e}$$

$$\text{Back} \Rightarrow J_y\hat{y} + J_z\hat{z} = H_z\hat{y} - H_y\hat{z} \text{ and } M_y\hat{y} + M_z\hat{z} = -E_z\hat{y} + E_y\hat{z} \tag{6.2f}$$

J_x, J_y, and J_z are the electric current densities and M_x, M_y, and M_z are the magnetic current densities on the surface top, bottom, left, right, front, and back of

the imaginary surfaces in figure 6.1. The current components, which are tangent to the surface exist. Those current densities converted from time domain to frequency domain in the time-marching-loop using discrete Fourier transform.

6.2.3 Frequency Domain Near-Field to Far-Field Transformation

The directivity equations if an antenna in far-field region can be found given with auxiliary functions N_θ, N_ϕ, L_θ, L_ϕ as in equation 6.3. More exclusive discrimination of the far-field theories and radiation equations for E_θ, E_ϕ, H_θ, and H_ϕ can be found in [129]. These are the equations used in FDTD computation to do the near-field to far-field transformations [80, 133, 134].

$$D_\theta = \left(\frac{k^2}{8\pi\eta_0 P_{rad}}\right)|L_\phi + N_\theta\eta_0|^2 \tag{6.3a}$$

$$D_\phi = \left(\frac{k^2}{8\pi\eta_0 P_{rad}}\right)|L_\phi - N_\theta\eta_0|^2 \tag{6.3b}$$

The auxiliary functions and total radiated power can be calculated using equation 6.4 and 6.5 for the problem-spaces with rectangular and cylindrical grids respectively. ψ is the angle between the position vector of far-field observation point and the position vector of the location of considered current density component ($\vec{r'}$). $\vec{r'}$ can be written as $x'\hat{x} + x'\hat{y} + x'\hat{z}$ in the rectangular grid and $\rho'\hat{\rho} + \phi'\hat{\phi} + z'\hat{z}$ in the cylindrical grid.

Near-Field to Far-Field Transformation in Rectangular Grid :

$$\text{Total radiated power } \Rightarrow\ P_{rad} = \frac{1}{2}\Re\left(\sum_S |\vec{J^*} \times \vec{M}|\right) \tag{6.4a}$$

$$\text{Where : } \vec{J} = J_x\vec{x} + J_y\vec{y} + J_z\vec{z}$$

$$\text{and } \vec{M} = M_x\vec{x} + M_y\vec{y} + M_z\vec{z}$$

$$N_\theta = \sum_S \left(J_x \cos\theta \cos\phi + J_y \cos\theta \sin\phi - J_z \sin\theta\right) e^{-jk|\vec{r'}|\cos\psi} \tag{6.4b}$$

$$N_\phi = \sum_S \left(-J_x \sin\phi + J_y \cos\phi\right) e^{-jk|\vec{r'}|\cos\psi} \tag{6.4c}$$

$$L_\theta = \sum_S \left(M_x \cos\theta \cos\phi + M_y \cos\theta \sin\phi - M_z \sin\theta\right) e^{-jk|\vec{r'}|\cos\psi} \tag{6.4d}$$

$$L_\phi = \sum_S \left(-M_x \sin\phi + M_y \cos\phi\right) e^{-jk|\vec{r'}|\cos\psi} \tag{6.4e}$$

Near-Field to Far-Field Transformation in Cylindrical Grid :

$$\text{Total radiated power } \Rightarrow \; P_{rad} = \frac{1}{2}\Re\left(\sum_S |\vec{J}^* \times \vec{M}|\right) \tag{6.5a}$$

$$\text{Where : } \vec{J} = J_\rho\vec{\rho} + J_\phi\vec{\phi} + J_z\vec{z}$$

$$\text{and } \vec{M} = M_\rho\vec{\rho} + M_\phi\vec{\phi} + M_z\vec{z}$$

$$N_\theta = \sum_S \left(J_\rho \cos\theta \cos(\phi - \phi') + J_\phi \cos\theta \sin(\phi - \phi') - J_z \sin\theta\right) e^{-jk|\vec{r'}|\cos\psi} \tag{6.5b}$$

$$N_\phi = \sum_S \left(-J_\rho \sin(\phi - \phi') + J_\phi \cos(\phi - \phi')\right) e^{-jk|\vec{r'}|\cos\psi} \tag{6.5c}$$

$$L_\theta = \sum_S \left(M_\rho \cos\theta \cos(\phi - \phi') + M_\phi \cos\theta \sin(\phi - \phi') - M_z \sin\theta\right) e^{-jk|\vec{r'}|\cos\psi} \tag{6.5d}$$

$$L_\phi = \sum_S \left(-M_\rho \sin(\phi - \phi') + M_\phi \cos(\phi - \phi')\right) e^{-jk|\vec{r'}|\cos\psi} \tag{6.5e}$$

Near-field to far-field transformation for the nonorthogonal unstructured grid which is presented in Section 3.3 can be derived using equations 6.4, 3.49d, 3.49e, 3.49f, 3.50d, 3.50e and 3.50f.

6.3 Large Finite Array Simulation

Inside the time-marching-loop, three main functionalities will be accomplished iteratively in each time steps. They are updating electric field, updating magnetic field, updating field components from sources, and collecting data from probes

There is a large probe enclosing the whole structure which is utilized as the imaginary near-field surface to collect all the electric and magnetic current information in each time step. Then the current densities are originally collected in time domain. But they were converted to frequency domain within the time-marching-loop. In these proposed methods, this near-field current density data of various patch array and antenna element are merged into the current densities of arbitrarily large array antennas. Then the near-field to far-field transformation will be carried out on this constructed current density data.

6.3.1 First Proposed Scheme to Simulate Large Finite Array Antennas

6.3.1.1 Algorithm

In this scheme, finite-by-finite, infinite-by-finite, finite-by-infinite, and infinite-by-infinite arrays are simulated in separate time matching loops. The radiating element of all four arrays can have any design. In this section, we use simple patch antenna's specification (Figure 5.7). Even though the finite sizes of the particulate arrays can have any number, the simulation presented is based on 20-by-infinity, infinity-by-20, and 8-by-8 arrays. The arrays annotated as (a), (b), (c), and (d) of Figure 6.3 are illustrating for arrays being simulated (infinite-by-infinite array with periodicities in both $\hat{x}$ and $\hat{y}$ directions, 20-by-infinite array with the periodicity in $\hat{y}$ direction, infinite-by-20 array with the periodicity in $\hat{x}$ direction, and finite 4-by-4 array respectively). These four simulations can be done simultaneously using four cores of a computer as they are simulated in separate time-marching-loops. The current densities are collected at strategic locations in each of the simulation. The current densities on the imaginary surfaces, above and below of the middle elements of the large array are recorded from the imaginary surfaces on the top and bottom ($+\hat{z}$ and $-\hat{z}$) of infinite-by-infinite array simulations (a). The current densities of top left, top right, bottom left, and bottom right corners of the large

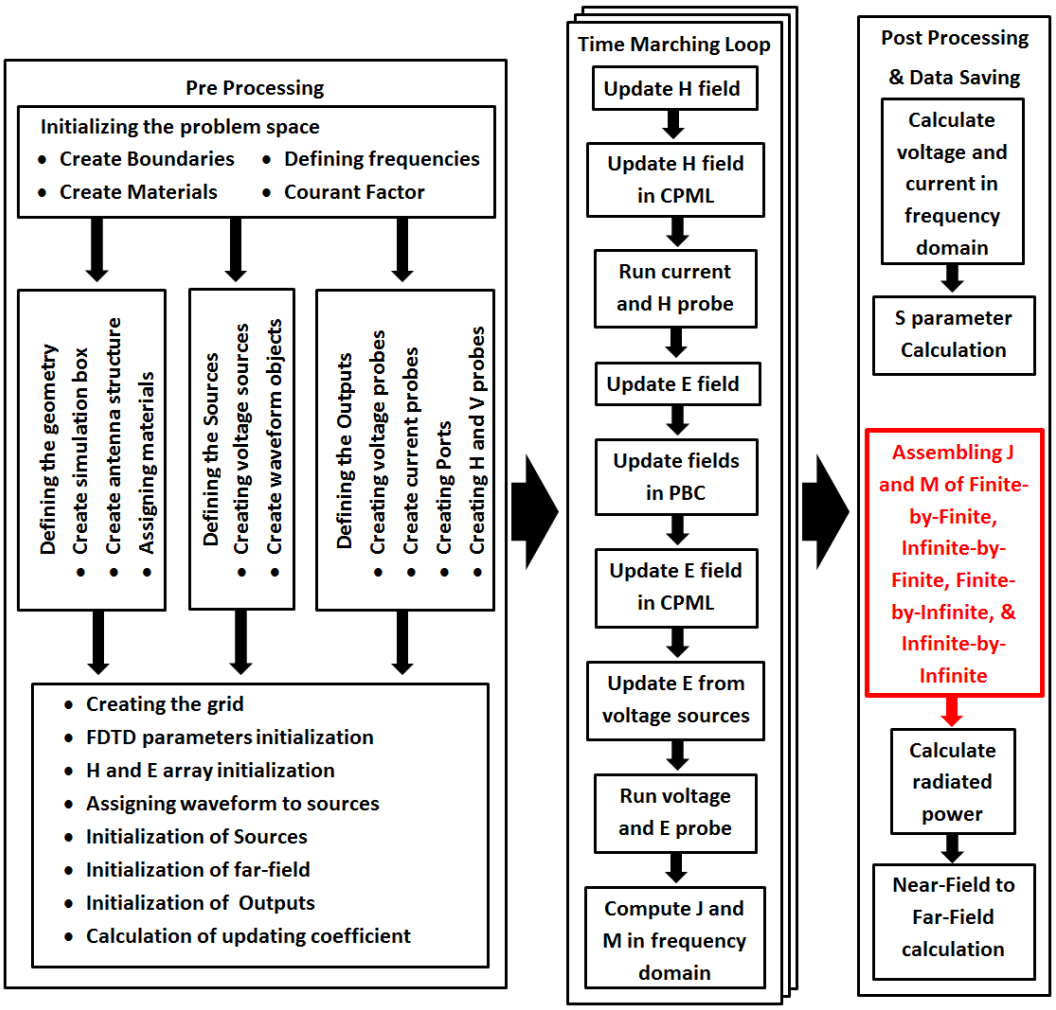

FIGURE 6.2: Abstract Functional Illustration of *PASim* for simulating finite array using first scheme

array are recorded from corner 2-by-2 subdivided arrays of the 4-by-4 finite array. In addition to the current densities on the imaginary surfaces in $+\hat{z}$ and $-\hat{z}$ direction, current densities in the surfaces in $+\hat{x}$, $-\hat{x}$, $+\hat{y}$, and $-\hat{y}$ will be recorded. The current densities of top, bottom, left, and right edge elements are collected using two elements at the infinite edges of semi-infinite arrays (first two and last two elements of both arrays). Basically, the current distributions on the surfaces next to the periodic boundaries are discarded, and the current distributions on the surfaces next to the CPML may be used to construct the current densities of a large array. All the current densities are taken in the frequency domain and the conversion from time to frequency domain is performed in the time-marching-loop.

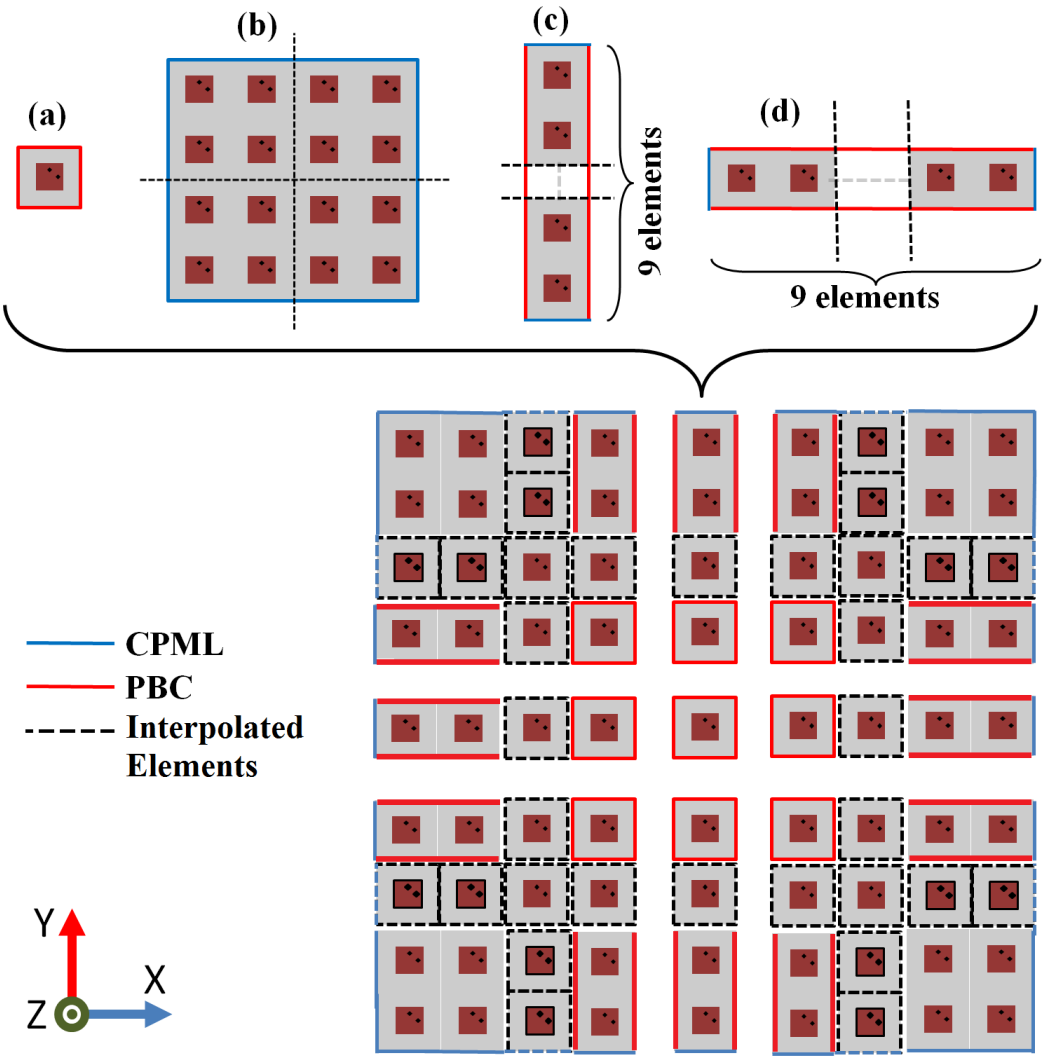

FIGURE 6.3: Large finite phased array antenna - Scheme I

There will be discontinuities at the cut-off lines (black dashed lines) and periodic boundaries (red lines). Interpolated element currents are facilitating a smooth transition from periodic boundaries to cut-off lines. These current densities are used to *merge and combine* the near-field samples (current density components) of a large finite array. This frequency domain interpolated current densities (*building blocks*) are utilized for the near-field to far-field transformation calculations. The array annotated as (e) in Figure 6.3 shows the assembly of all the near-field current densities in the frequency domain for a planar array. The elements indicated with dashed lines represent surfaces with interpolated current densities using adjacent elements, which ensure a smooth transition from one element to the next

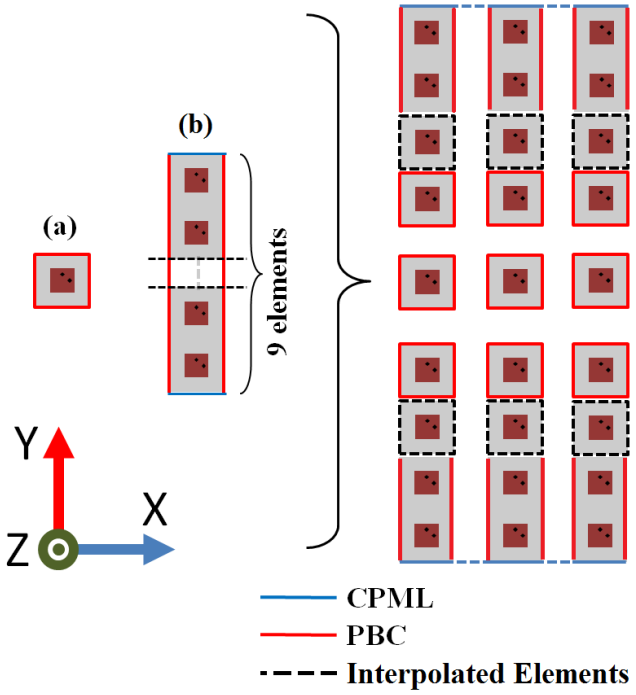

FIGURE 6.4: Large cylindrical phased array antenna - Scheme I

throughout the array. Subsequent to this assembly, the process of near-field to far-field transformation is computed to simulate the far-field radiation pattern of an arbitrarily large finite-by-finite array.

Figure 6.4 illustrates the proposed scheme for cylindrical array. The scheme is much simpler than planar finite-by-finite array since the cylindrical array can be considered as a semi-infinite array. The only issue, which has not been addressed in this dissertation is that the boundary between excited and unexcited array elements has not been correctly modeled in this scheme. Hence more work has to be done to introduce a new model for current densities on the surfaces in $+\phi$ and $-\phi$ directions. As mentioned previously faceted-cylindrical array can be modeled for the infinite-by-infinite array only. Thereupon this scheme of the second scheme discussed in section 6.3.2 can not be implemented for a faceted-cylindrical array.

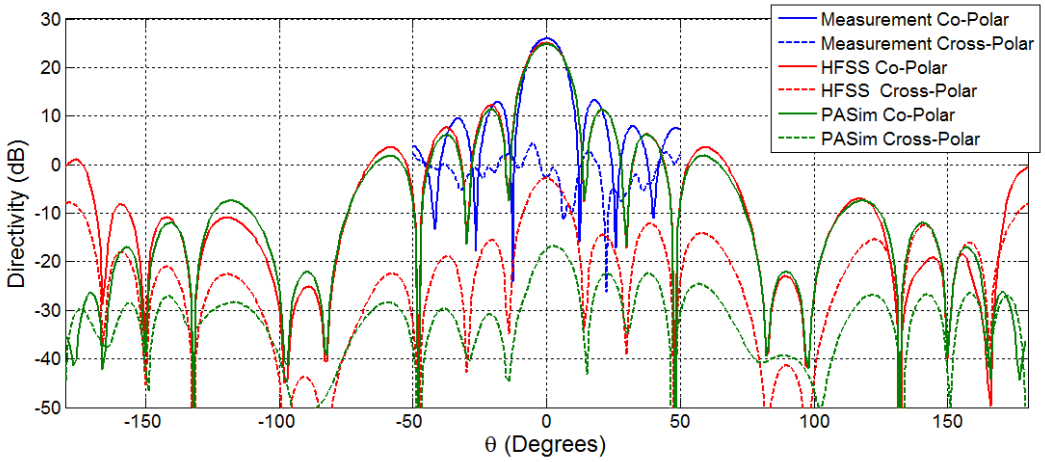

(a) Horizontal principal plane cut

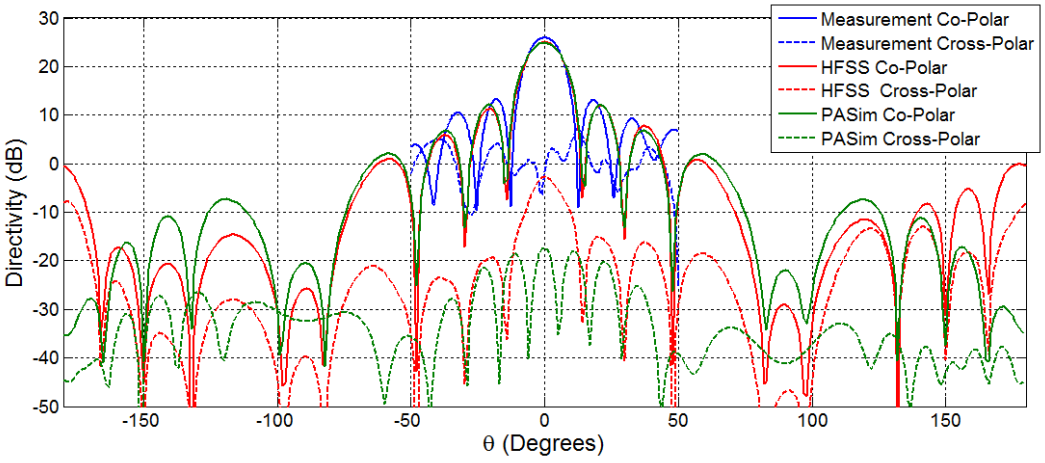

(b) Vertical principal plane cut

FIGURE 6.5: Principal plane cuts of 8×8 array simulations and measurements.

6.3.1.2 Simulation

The first scheme can be used to simulate any finite planar array simulation with an arbitrary number of elements. One of the benefits in using this algorithm and the algorithm discussed in section 6.3.2 is the ability to store the current information and reuse them in a new simulation of an array with same element designing and a different number of elements. In this section, simulation results of two arrays are presented with 64 and 1024 elements. The 8-by-8 array is the same planar array measured in this research. In consequence, the compassion of measurements, HFSS simulations, and *PASim* simulations are presented in this

	number of variables	simulation time (min)
8-by-8 array	$\sim 4.32 \times 10^8$	453
32-by-32 array	$\sim 4.38 \times 10^8$	521

TABLE 6.1: Benchmark of the simulation with the first scheme

subsection. The figure 6.5(a) and 6.5(b) are the horizontal and vertical principal plane cut of the 8x8 array. Both HFSS and *PASim* simulation of Co-polarization are having an excellent agreement. Due to imperfect model in both HFSS and *PASim*, the directivity of measurement is 1.2dB high than simulations. The cross-polarization level has a larger disagreement between measurement and simulations. The disagreement between HFSS and *PASim* simulations (15dB) can be minimized using the correct grid for modeling the problem space.

The number of variables, that have been solved in both simulations are given in Table 6.1. The number of variables is almost similar for both 8-by-8 array and 32-by-32 array. If the 8-by-8 array and 32-by-32 array simulations are not using the proposed scheme, the number of variables will be 5.62×10^8 and 98.23×10^8 respectively. A substantial reduction of unknown variables can be achieved by utilizing this scheme.

6.3.2 Second Proposed Scheme to Simulate Large Finite Array Antennas

6.3.2.1 Algorithm

For the convenience, the elements are annotated according to the location of current densities, which will be filled in the large array. Hence current densities of N (North) element will be filled in the upper edge of the large array, current densities of NE (Northeast) will be filled in the upper-right corner of the large array, and etc. Subsequently the nine elements are labeled as NH (North), SH (South), WT (West), ET (East), NW (Northwest), NE (Northeast), SW (Southwest), SE (Southeast), and IN (Inside). The sizes of NH, SH, ET, and WT are n-by-1,

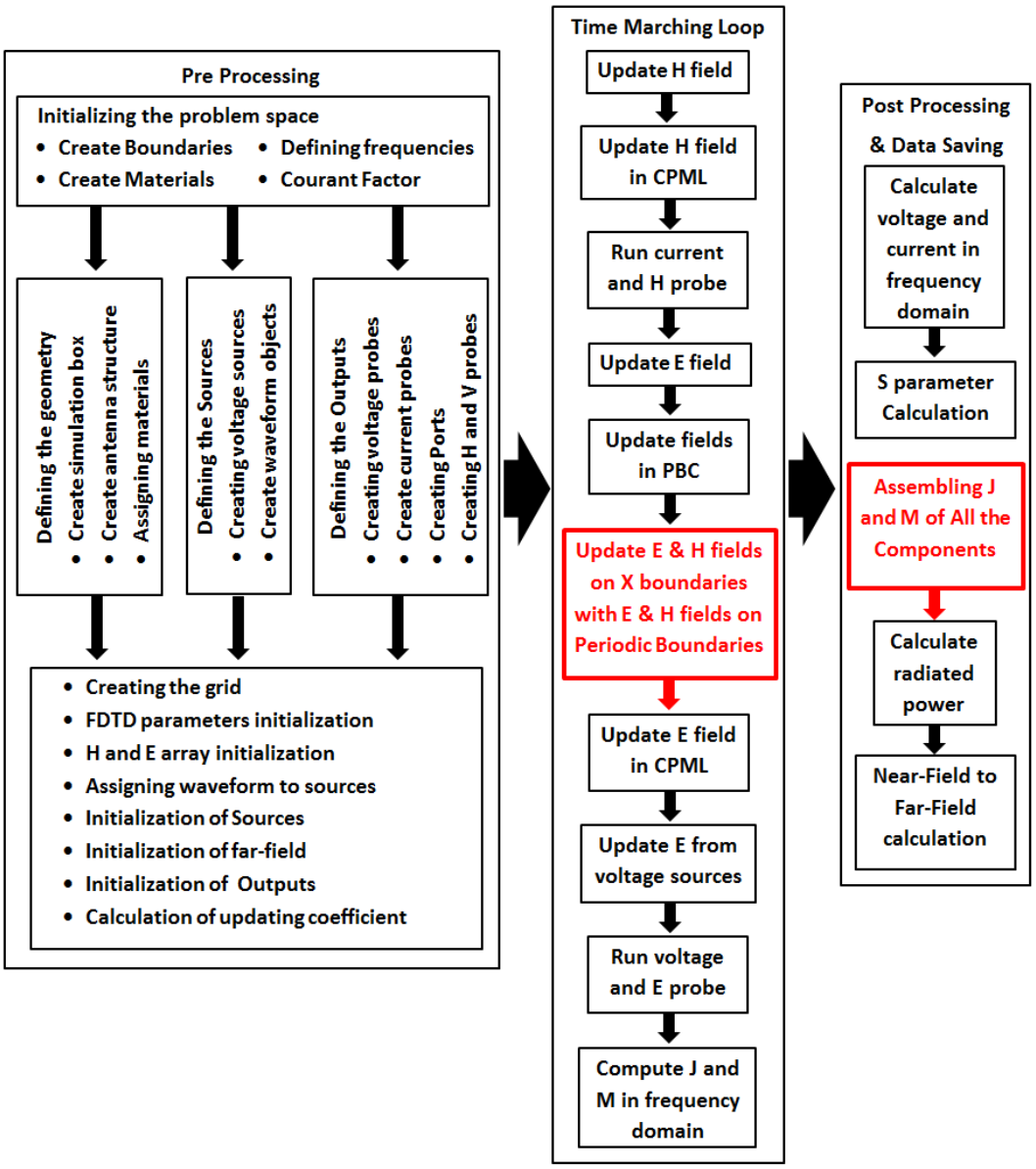

FIGURE 6.6: Abstract Functional Illustration of *PASim* for simulating finite array using the second scheme

NE, NS, SE, and SW are n-by-n, and IN is an active element. The simulations performed and presented in this dissertation are using n=2.

The NH element has CPML in $+\hat{z}$, $-\hat{z}$, and $+\hat{y}$ directions, periodic boundary in $+\hat{x}$ and $-\hat{x}$ directions, and so called X boundary in $-\hat{y}$ direction. The X boundary in $-\hat{y}$ are updated using equations 6.14a and 6.14b. All the boundary information of 9 arrays can be found in Table 6.2.

In the time-marching-loop, electric field component in IN element, which is the

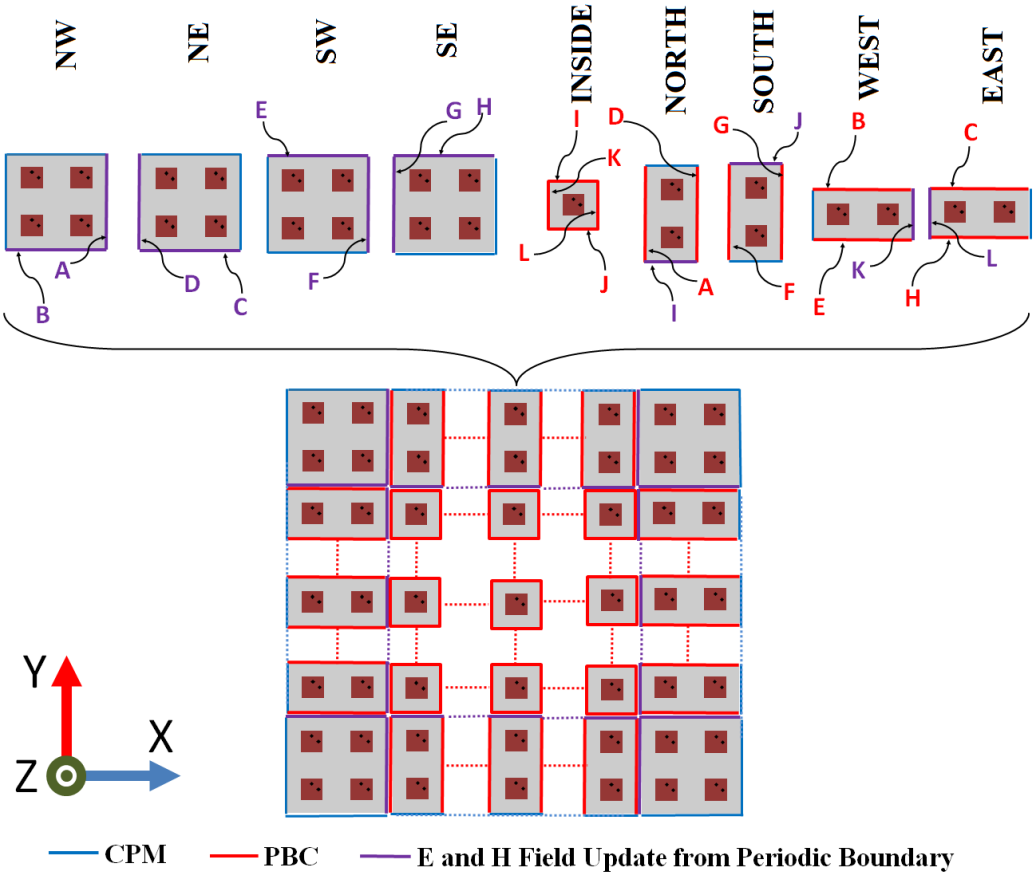

FIGURE 6.7: Large finite phased array antenna - Scheme II

independent element (no X boundaries) will be updated as the first priority task. The second is updating electric field components of NH, SH, ET, and WT, which have one X boundary. The relevant X boundaries are updated using equations 6.14a, 6.14b, 6.15a, 6.15b, 6.16a, 6.16b, 6.17a, and 6.17b. The final task is updating electric field components of NW, NE, SW, and SE. These arrays are having two X boundaries, which are updated using equation 6.6a, 6.6b, 6.7a, 6.7b, 6.8a, 6.8b, 6.9a, 6.9b, 6.10a, 6.10b, 6.11a, 6.11b, 6.12a, 6.12b, 6.13a, 6.13b. The updating process of magnetic fields and voltage sources, which are independent can be performed in any order. The near-field current probes are also independent processes.

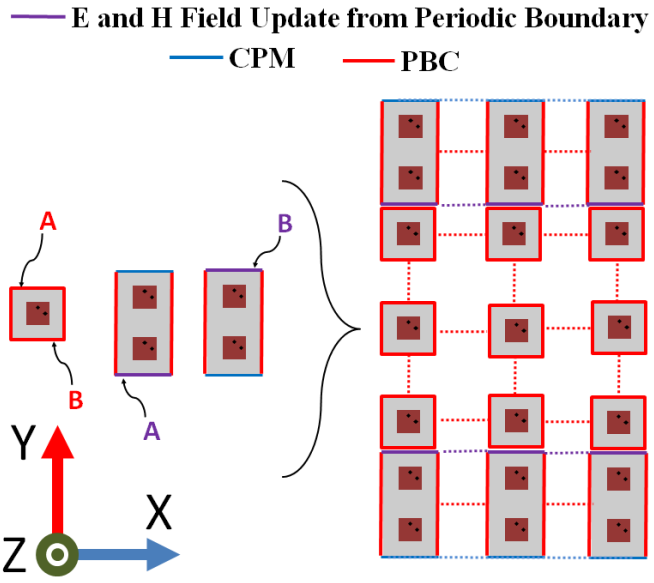

FIGURE 6.8: Large cylindrical phased array antenna - Scheme II

Element	CPML surfaces	PBC surfaces	X boundary surfaces
NH	$+\hat{z}$, $-\hat{z}$, and $+\hat{y}$	$+\hat{x}$ and $-\hat{x}$	$-\hat{y}$
SH	$+\hat{z}$, $-\hat{z}$, and $-\hat{y}$	$+\hat{x}$ and $-\hat{x}$	$+\hat{y}$
ET	$+\hat{z}$, $-\hat{z}$, and $+\hat{x}$	$+\hat{y}$ and $-\hat{y}$	$-\hat{x}$
WT	$+\hat{z}$, $-\hat{z}$, and $-\hat{x}$	$+\hat{y}$ and $-\hat{y}$	$+\hat{x}$
NW	$+\hat{z}$, $-\hat{z}$, $-\hat{x}$, and $+\hat{y}$	None	$+\hat{x}$ and $-\hat{y}$
NE	$+\hat{z}$, $-\hat{z}$, $+\hat{x}$, and $+\hat{y}$	None	$-\hat{x}$ and $-\hat{y}$
SW	$+\hat{z}$, $-\hat{z}$, $-\hat{x}$, and $-\hat{y}$	None	$+\hat{x}$ and $+\hat{y}$
SE	$+\hat{z}$, $-\hat{z}$, $+\hat{x}$, and $-\hat{y}$	None	$-\hat{x}$ and $+\hat{y}$
IN	$+\hat{z}$ and $-\hat{z}$	$+\hat{x}$, $+\hat{y}$, $-\hat{x}$, and $-\hat{y}$	None

TABLE 6.2: Boundary conditions of all the building-block arrays (Unit vectors are perpendicular to the surfaces)

6.3.2.2 Updating X Boundary

Updating A Boundary : Electric field components in $\hat{y}$ and $\hat{z}$ direction at **purple** color **A** boundary of the Northwest element can be updated with the electric field components in $\hat{y}$ and $\hat{z}$ direction at **red** color **A** boundary of the West element.

$$E_y^{n+1}(N_x^{NW}+1, i_y, i_z)|^{NW} = E_y^{n+1}(1, i_y, i_z)|^{NH} \tag{6.6a}$$

$$E_z^{n+1}(N_x^{NW}+1, i_y, i_z)|^{NW} = E_z^{n+1}(1, i_y, i_z)|^{NH} \tag{6.6b}$$

Updating B Boundary : Electric field components in $\hat{x}$ and $\hat{z}$ direction at **purple** color **B** boundary of the Northwest element can be updated with the electric field components in $\hat{x}$ and $\hat{z}$ direction at **red** color **B** boundary of the West element.

$$E_x^{n+1}(i_x, 1, i_z)|^{NW} = E_x^{n+1}(i_x, N_y^{WT} + 1, i_z)|^{WT} \tag{6.7a}$$

$$E_z^{n+1}(i_x, 1, i_z)|^{NW} = E_z^{n+1}(i_x, N_y^{WT} + 1, i_z)|^{WT} \tag{6.7b}$$

Updating C Boundary : Electric field components in $\hat{x}$ and $\hat{z}$ direction at **purple** color **C** boundary of the **NE** element can be updated with the electric field components in $\hat{x}$ and $\hat{z}$ direction at **red** color **C** boundary of the **ET** element.

$$E_x^{n+1}(i_x, 1, i_z)|^{NE} = E_x^{n+1}(i_x, N_y^{ET} + 1, i_z)|^{ET} \tag{6.8a}$$

$$E_z^{n+1}(i_x, 1, i_z)|^{NE} = E_z^{n+1}(i_x, N_y^{ET} + 1, i_z)|^{ET} \tag{6.8b}$$

Updating D Boundary : Electric field components in $\hat{y}$ and $\hat{z}$ direction at **purple** color **D** boundary of the **NE** element can be updated with the electric field components in $\hat{y}$ and $\hat{z}$ direction at **red** color **D** boundary of the **NH** element.

$$E_y^{n+1}(1, i_y, i_z)|^{NE} = E_y^{n+1}(N_x^{NH} + 1, i_y, i_z)|^{NH} \tag{6.9a}$$

$$E_z^{n+1}(1, i_y, i_z)|^{NE} = E_z^{n+1}(N_x^{NH} + 1, i_y, i_z)|^{NH} \tag{6.9b}$$

Updating E Boundary : Electric field components in $\hat{x}$ and $\hat{z}$ direction at **purple** color **E** boundary of the **SW** element can be updated with the electric field components in $\hat{x}$ and $\hat{z}$ direction at **red** color **E** boundary of the **WT** element.

$$E_x^{n+1}(i_x, N_y^{SW} + 1, i_z)|^{SW} = E_x^{n+1}(i_x, 1, i_z)|^{WT} \tag{6.10a}$$

$$E_z^{n+1}(i_x, N_y^{SW} + 1, i_z)|^{SW} = E_z^{n+1}(i_x, 1, i_z)|^{WT} \tag{6.10b}$$

Updating F Boundary : Electric field components in $\hat{y}$ and $\hat{z}$ direction at **purple** color **F** boundary of the **SW** element can be updated with the electric field components in $\hat{y}$ and $\hat{z}$ direction at **red** color **F** boundary of the **SH** element.

$$E_y^{n+1}(N_x^{SW}+1, i_y, i_z)|^{SW} = E_y^{n+1}(1, i_y, i_z)|^{SH} \tag{6.11a}$$

$$E_z^{n+1}(N_x^{SW}+1, i_y, i_z)|^{SW} = E_z^{n+1}(1, i_y, i_z)|^{SH} \tag{6.11b}$$

Updating G Boundary : Electric field components in $\hat{y}$ and $\hat{z}$ direction at **purple** color **G** boundary of the **SE** element can be updated with the electric field components in $\hat{y}$ and $\hat{z}$ direction at **red** color **G** boundary of the **SH** element.

$$E_y^{n+1}(1, i_y, i_z)|^{SE} = E_y^{n+1}(N_x^{SH}+1, i_y, i_z)|^{SH} \tag{6.12a}$$

$$E_z^{n+1}(1, i_y, i_z)|^{SE} = E_z^{n+1}(N_x^{SH}+1, i_y, i_z)|^{SH} \tag{6.12b}$$

Updating H Boundary : Electric field components in $\hat{x}$ and $\hat{z}$ direction at **purple** color **H** boundary of the **SE** element can be updated with the electric field components in $\hat{x}$ and $\hat{z}$ direction at **red** color **H** boundary of the **ET** element.

$$E_x^{n+1}(i_x, N_y^{SE}+1, i_z)|^{SE} = E_x^{n+1}(i_x, 1, i_z)|^{ET} \tag{6.13a}$$

$$E_z^{n+1}(i_x, N_y^{SE}+1, i_z)|^{SE} = E_z^{n+1}(i_x, 1, i_z)|^{ET} \tag{6.13b}$$

Updating I Boundary : Electric field components in $\hat{x}$ and $\hat{z}$ direction at **purple** color **I** boundary of the **NH** element can be updated with the electric field components in $\hat{x}$ and $\hat{z}$ direction at **red** color **I** boundary of the **IN** element.

$$E_x^{n+1}(i_x, 1, i_z)|^{NH} = E_x^{n+1}(i_x, N_y^{IN}+1, i_z)|^{IN} \tag{6.14a}$$

$$E_z^{n+1}(i_x, 1, i_z)|^{NH} = E_z^{n+1}(i_x, N_y^{IN}+1, i_z)|^{IN} \tag{6.14b}$$

Updating J Boundary : Electric field components in $\hat{x}$ and $\hat{z}$ direction at **purple** color **J** boundary of the **SH** element can be updated with the electric field components in $\hat{x}$ and $\hat{z}$ direction at **red** color **J** boundary of the **IN** element.

$$E_x^{n+1}(i_x, N_y^{SH}+1, i_z)|^{SH} = E_x^{n+1}(i_x, 1, i_z)|^{IN} \tag{6.15a}$$

$$E_z^{n+1}(i_x, N_y^{SH}+1, i_z)|^{SH} = E_z^{n+1}(i_x, 1, i_z)|^{IN} \tag{6.15b}$$

Updating K Boundary : Electric field components in $\hat{y}$ and $\hat{z}$ direction at **purple** color **K** boundary of the **WT** element can be updated with the electric field components in $\hat{x}$ and $\hat{z}$ direction at **red** color **A** boundary of the **IN** element.

$$E_y^{n+1}(N_x^{WT}+1, i_y, i_z)|^{WT} = E_y^{n+1}(1, i_y, i_z)|^{IN} \tag{6.16a}$$

$$E_z^{n+1}(N_x^{WT}+1, i_y, i_z)|^{WT} = E_z^{n+1}(1, i_y, i_z)|^{IN} \tag{6.16b}$$

Updating L Boundary : Electric field components in $\hat{y}$ and $\hat{z}$ direction at **purple** color **L** boundary of the **ET** element can be updated with the electric field components in $\hat{y}$ and $\hat{z}$ direction at **red** color **L** boundary of the **IN** element.

$$E_y^{n+1}(1, i_y, i_z)|^{ET} = E_y^{n+1}(N_x^{IN}+1, i_y, i_z)|^{IN} \tag{6.17a}$$

$$E_z^{n+1}(1, i_y, i_z)|^{ET} = E_z^{n+1}(N_x^{IN}+1, i_y, i_z)|^{IN} \tag{6.17b}$$

6.3.2.3 Simulation

The second scheme shares the same capability of simulating any finite planar array with an arbitrary number of elements. Array with 64 elements and 1024 elements will be simulated using the scheme introduced in this section. As in the subsection 6.3.1.2, the compassion of measurements, HFSS simulations, and *PASim* simulations are plotted for 64 element array. The figure 6.9(a) and 6.9(b)

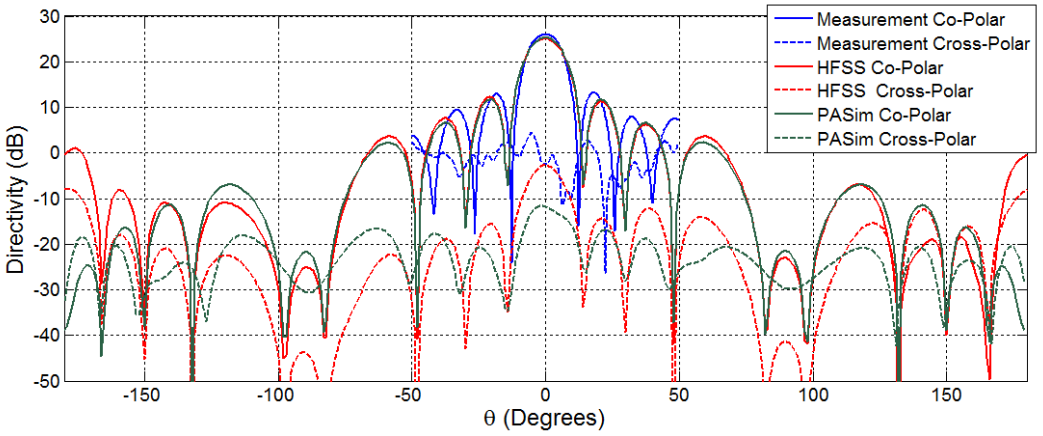

(a) Horizontal principal plane cut

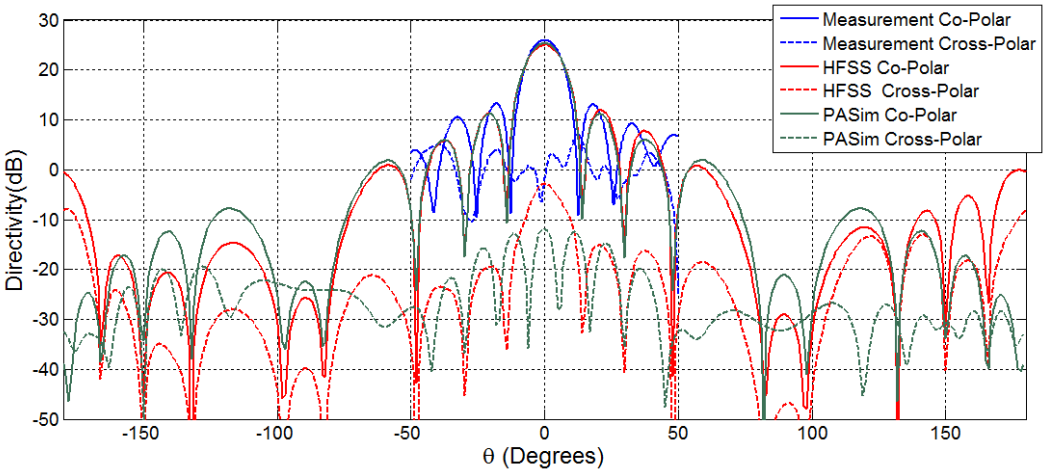

(b) Vertical principal plane cut

FIGURE 6.9: Principal plane cuts of 8×8 array simulations and measurements.

	number of variables	simulation time (min)
8-by-8 array	$\sim 1.96 \times 10^8$	242
32-by-32 array	$\sim 2.01 \times 10^8$	304

TABLE 6.3: Benchmark of the simulation with the Second scheme

are the horizontal and vertical principal plane cut of the 64-element array. Co-polarizations produced from both first and second methods are almost the same. In average 0.02dB are reduced between co-polarizations from the simulations of first and second methods. The maximum disagreement between cross-polarization levels from HFSS and *PASim* simulations is 10dB.

The number of unknown variables been solved and elapsed for completing both

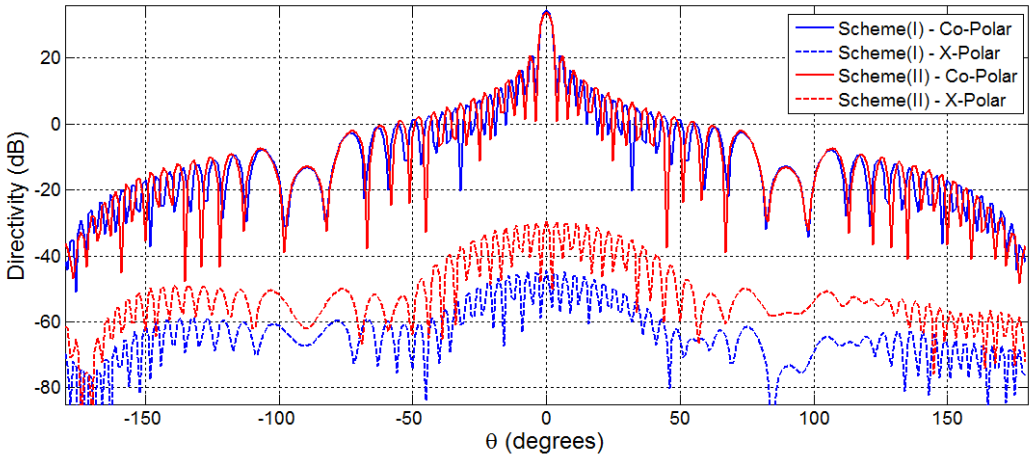

(a) Horizontal principal plane cut

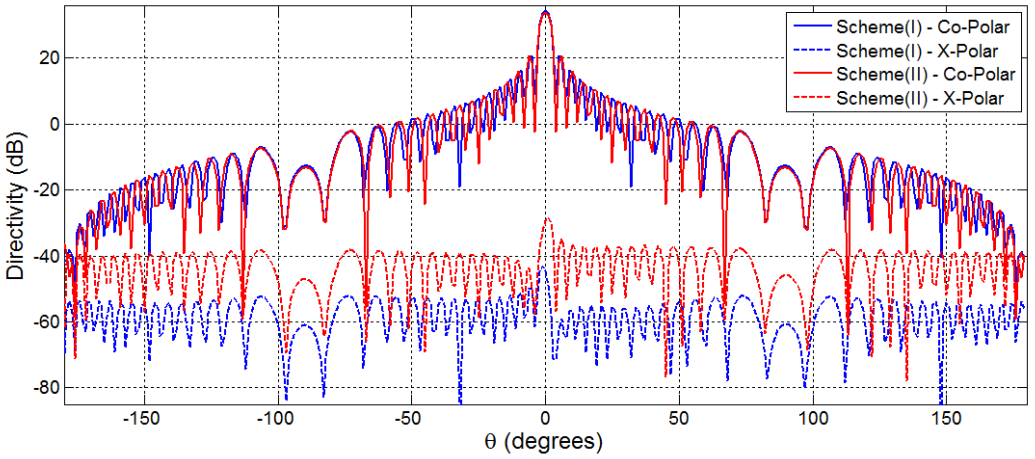

(b) Vertical principal plane cut

FIGURE 6.10: Principal plane cut of 32 × 32 array simulation using *PASim* program.

simulations is presented in Table 6.3. Although the number of variables is almost same for both 64-element array and 1024-element array, there is a huge deduction in both unknown variables to solve and elapsed time to complete simulation. The 64-element array and 1024-element array simulations using the second scheme exhibit reduction of the number of unknown variables significantly (so elapsed time). The method is more elegant than the first method since it simulates the minimum number of variables and still manages to produce improved simulation results.

The Figure 6.10 presents the compassion of 32×32 array antennas simulation by

both proposed schemes. The co-polarization patterns are having very good agreement and cross-polarization prediction from the second scheme is higher than the prediction from the first scheme.

Note: The reason for considering only two elements at the edges and corners in both schemes can be explained using the simulations of AEP of 17-by-infinity array as shown in Figure 6.11. The co-polarization and cross-polarization patterns of Element (1) and Element (2) are drastically different. But patterns of Element (3),Element (4), and Element (5) are slightly different. It is not required to limit the number of element to be two at the edges and corners. One can use high number of elements and gain nearly the same results after huge consumption of computational resources for the simulation.

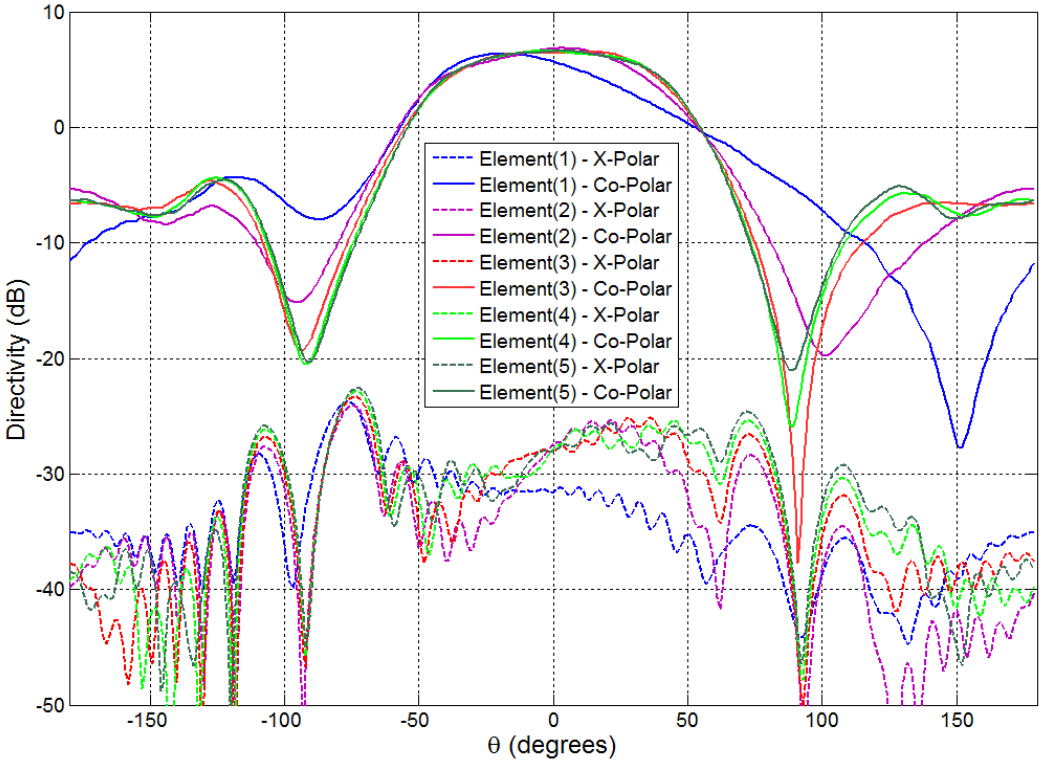

FIGURE 6.11: Active element pattern of 17-By-Infinite array simulated by *PASim*

Chapter 7

Conclusions and Future Work

7.1 Conclusions of The Dissertation

This research has been involved with both measurements and simulation of phased array antennas. The measurements of CPAD-I were taken in the old far-field chamber and the measurements of CPAD-II were taken in the new near-field chamber. The nine achievements of this research are listed below:

1. Derivation of the FDTD equations for anisotropic media in cylindrical coordinate system (Section 3.2.1).

2. Adaptation of *constant horizontal wavenumber approach* in periodic boundaries of $\hat{\phi}$ and $\hat{z}$ in cylindrical coordinate system (Section 3.2.3).

3. Derivation of the FDTD equations for isotropic media in nonorthogonal unstructured coordinate system (Section 3.3.1).

4. Adaptation of *constant horizontal wavenumber approach* in periodic boundaries of $\hat{\beta}$ and $\hat{\gamma}$ in nonorthogonal unstructured coordinate system (Section 3.3.3).

5. Successful implementation of PBC FDTD in rectangular, cylindrical, and nonorthogonal unstructured grids for simulating active elements of planar, cylindrical and faceted-cylindrical array antennas (Section 3.4).

6. Successful implementation of a simulation model (scheme 1) for radiation pattern prediction of large finite array based on finite, semi-finite, and infinite arrays (Section 6.3.1).

7. Successful implementation of a simulation model (scheme 2) for radiation pattern prediction of large finite array based on infinite array and small chunk of arrays with so called X-Boundary (Section 6.3.2).

8. Comparison of simulated data with measurements taken from configurable array systems (CPAR)(Section 6.3.1 and Section 6.3.2).

9. Integration of genetic algorithm with the *PASim* program to optimized the array antenna elements.

All the source code of *PASim* program can be found on GitHub (`https://github.com/sudanthaperera/PASim.git`).

7.2 Proposed Further Improvements of *PASim*

The *PASim* program developed in this work is in the prototype stage and can be further improved to become an open source software supported by a community of developers. Different from other existing FDTD tools, the simulator is more specifically for phased array antenna designing, which will be more useful in very demanding future applications. Four specific areas of improvements for *PASim* are further described in the following sections.

7.2.1 Parallel Computing Capability

Full parallel computing capability can be enabled in future *PASim* program in three important steps. The first step is switching from Java to C++ implementations. The second step is using both CPU and GPU. The program will be optimized for hardware resource usage after the accomplishment of the second step. If the *PASim* should be targeted to run on a cluster of computers, the third step must be implemented, which is enabling the functionality of distributed memory usage.

7.2.1.1 *PASim* in C++ Programming Language

The *PASim* was originally written in C programming language. The GNU GCC is used to compile the C code written in ANCI C99, and GNU Linux system was the targeted system to run the compiled executable code. Debugging the code after introducing a new feature or functionality was time-consuming. Then the program was rewritten in Java programming language (SE8). Although that was 3 times slower than the program written in C and JVM is a memory hog, the debugging and developing time was shorter. Then Java was used as the choice of prototyping programming language. Since most of the scientific computing libraries and parallel computing libraries are written in C++ programming language, and most of the professional scientific programmers in the field of computational electromagnetic prefer to use C++, the choice of the language will have to be switched from Java to C++. Additionally, C++ has operator overloading, complex arithmetic, tiny objects [135] and many other features that can create layers of abstractions and allow the writing of codes in different programming styles. An even more important benefit will appear in introducing the parallel computing capabilities in new *PASim* versions.

7.2.1.2 Utilization of Graphics Processing Units Acceleration

Even though central processing unit (CPU) is the proceeding unit used traditionally for many computational tasks, other hardware acceleration units such as graphics processing units (GUPs) and field programmable gate arrays (FPGAs) are increasingly used in the field of scientific computing. Since special-purpose FPGA hardware acceleration will need more attention on hardware designing and implementation, GPU is more suitable for *PASim* targeted to run on mass-produced hardware. GPUs are built with many processing units with low computational speed and main memories. On the other hand, memory bandwidth and memory widths are larger in most of the excellent GPUs available today. GPUs are also more optimized for parallel or stream processing with large memory bandwidth. There are few options available to use as the framework for CPU and GPU processing. The Open Computing Language (OpenCL) is the option with OpenCL specification license. ATI Close-To-Metal (CTM) is an another specialized language for GPU programming. Brook programming language is an extension of ANSI C developed by Stanford University Graphics Lab. Unlike other GPU programming frameworks, Brook is not vendor-specific. Nvidia CUDA C is a freeware (proprietary), which is more popular in GPU programming. CUDA C is essentially C programming language with a few extensions. Parallel computing with CUDA C programming is easier than the other options. CUDA C will be a possible option for building fast FDTD co-processor using GPU.

7.2.1.3 Enabling to Run on Systems with Shared and Distributed Memory

Message Passing Interface (MPI) can be considered to utilize in the future development of this project, if *PASim* is aiming to run on a cluster or distributed system where the distributed memory is available. MPI will provide good portability and efficiency to the *PASim* program. There are many incarnations of MPI

[136]. Open Multi-Processing (OpenMP) is another option that can be used in small scientific computing programs running on shared-memory machines. The parallelization of *PASim* program can be more effective using a combination of MPI and OpenMP.

7.2.2 Introducing Advanced Algorithm

7.2.2.1 Subgridding Technique

The method to make the grid in this work is good for evaluating the new algorithm introduced in Chapter 6 and benchmark problems. Real world phased array antennas have more complicated geometrical details, such as feed port and manufacturing imperfections. Even though those minor geometrical details might not significantly affect the simulation, implementing a space lattices conform to the boundary of complicated structures will give more accurate results. The rectangular, cylindrical, nonorthogonal, unstructured, nonuniform, locally conformal curvilinear, and irregular grids have to be used in the antenna elements of some proposed phased array systems. Therefore, a more sophisticated algorithm will need to be implemented for making a better simulation program for designing phased array with an arbitrary geometry of radiating elements.

7.2.2.2 An Adaptive Stopping Criterion

Current *PASim* will run for a given time specified by the number of steps or converge to a given value of electric field or magnetic field. These two may not be the only options available and are definitely not the accurate and efficient way to terminate the time-marching-loop. The vector fitting algorithm [137, 138] can be implemented in time-marching-loop to terminate the loop properly. This method had been very accurate and robust in applications.

7.2.3 User Friendly Interface

The *PASim* developed in this work has no user interface. If there is a new model of antenna, which needs to be simulated, the source code has to be changed. An implementation of proper graphical user interface (GUI) or module for high-level scripting language are valid ways to avoid changing and compiling source code before every time the simulation has to be run.

7.2.4 Build a Community of Developers

After achieving above objectives, this program can be published or released under proper OpenSource or Free software license. Accordingly, a community of developers can be created for this open source FDTD, electromagnetic solver. There will be mutual benefits for each and every developer, including original developers, by making it an open source project. Since the software is being peer-reviewed by the community, the reliability of the software will be increased gradually without much burden to its original developers.

Bibliography

[1] F Braun. Electrical oscillations and wireless telegraphy. nobel lecture, 11 december 1909, 2012.

[2] G Marconi. Directive antenna. In *Proc. Royal Soc*, volume 77, 1906.

[3] HT Friis. A new directional receiving system. *Proceedings of the Institute of Radio Engineers*, 13(6):685–707, 1925.

[4] HT Friis, CB Feldman, and WM Sharpless. The determination of the direction of arrival of short radio waves. *Proceedings of the Institute of Radio Engineers*, 22(1):47–78, 1934.

[5] Harald T Friis and Carl B Feldman. A multiple unit steerable antenna for short-wave reception. *Proceedings of the Institute of Radio Engineers*, 25(7): 841–917, 1937.

[6] WW Hansen and LM Hollingsworth. Design of" flat-shooting" antenna arrays. *Proceedings of the IRE*, 27(2):137–143, 1939.

[7] WWUJR Woodyard Hansen and JR Woodyard. A new principle in directional antenna design. *Radio Engineers, Proceedings of the Institute of*, 26 (3):333–345, 1938.

[8] E Bruce. Developments in short-wave directive antennas*. *Bell System Technical Journal*, 10(4):656–683, 1931.

[9] PS Carter. Circuit relations in radiating systems and applications to antenna problems. *Radio Engineers, Proceedings of the Institute of*, 20(6):1004–1041, 1932.

[10] Sergei Alexander Schelkunoff. A mathematical theory of linear arrays. *Bell System Technical Journal*, 22(1):80–107, 1943.

[11] GC Southworth. Certain factors affecting the gain of directive antennas. *Radio Engineers, Proceedings of the Institute of*, 18(9):1502–1536, 1930.

[12] CL Dolph. A current distribution for broadside arrays which optimizes the relationship between beam width and side-lobe level. *Proceedings of the IRE*, 34(6):335–348, 1946.

[13] Thomas Tallott Taylor. Design of line-source antennas for narrow beamwidth and low side lobes. *Transactions of the IRE Professional Group on Antennas and Propagation*, 3(1):16–28, 1955.

[14] Benjamin Lax, Kenneth J Button, and Laura M Roth. Ferrite phase shifters in rectangular wave guide. *Journal of Applied Physics*, 25(11):1413–1421, 1954.

[15] Alan J Fenn, Donald H Temme, William P Delaney, and William E Courtney. The development of phased-array radar technology. *Lincoln Laboratory Journal*, 12(2):321–340, 2000.

[16] JF White. Review of semiconductor microwave phase shifters. *Proceedings of the IEEE*, 56(11):1924–1931, 1968.

[17] JF White. Origins of high-power diode switching. *IEEE Transactions on Microwave Theory and Techniques*, 32(9):1105–1105, 1984.

[18] WJ Ince and DH Temme. Phasers and time delay elements. *Advances in Microwaves*, 4:1–189, 1969.

[19] RH Hardin, EJ Downey, and J Munushian. Electronically-variable phase shifters utilizing variable capacitance diodes, 1960.

[20] Victor C Anderson. Digital array phasing. *The Journal of the Acoustical Society of America*, 32(7):867–870, 1960.

[21] TE Curtis and RJ Ward. Digital beam forming for sonar systems. *Communications, Radar and Signal Processing, IEE Proceedings F*, 127(4):257–265, 1980.

[22] John Litva and Titus K Lo. *Digital beamforming in wireless communications*. Artech House, Inc., 1996.

[23] P Barton. Digital beam forming for radar. *Communications, Radar and Signal Processing, IEE Proceedings F*, 127(4):266–277, 1980.

[24] Howells Paul W. Intermediate frequency side-lobe canceller, August 24 1965. US Patent 3,202,990.

[25] P Howells. Explorations in fixed and adaptive resolution at ge and surc. *IEEE Transactions on Antennas and Propagation*, 24(5):575–584, 1976.

[26] WILLIEW Ng, Andrew A Walston, Gregory L Tangonan, Jar Juch Lee, Irwin L Newberg, and Norman Bernstein. The first demonstration of an optically steered microwave phased array antenna using true-time-delay. *Journal of Lightwave Technology*, 9(9):1124–1131, 1991.

[27] Timothy J Peters. A conjugate gradient-based algorithm to minimize the sidelobe level of planar arrays with element failures. *IEEE Transactions on Antennas and Propagation*, 39(10):1497–1504, 1991.

[28] Vittorio Murino, Andrea Trucco, and Carlo S Regazzoni. Synthesis of unequally spaced arrays by simulated annealing. *IEEE Transactions on Signal Processing*, 44(1):119–122, 1996.

[29] Randy L Haupt. Genetic algorithm design of antenna arrays. In *Aerospace Applications Conference, 1996. Proceedings., 1996 IEEE*, volume 1, pages 103–109. IEEE, 1996.

[30] OM Bucci, G Franceschetti, G Mazzarella, and G Panariello. Intersection approach to array pattern synthesis. In *IEE Proceedings H-Microwaves, Antennas and Propagation*, volume 137, pages 349–357. IET, 1990.

[31] Majid M Khodier and Christos G Christodoulou. Linear array geometry synthesis with minimum sidelobe level and null control using particle swarm optimization. *IEEE Transactions on Antennas and Propagation*, 53(8):2674–2679, 2005.

[32] Eli Brookner. Phased-array and radar astounding breakthroughsan update. In *2008 IEEE Radar Conference*, pages 1–6. IEEE, 2008.

[33] Eli Brookner. Phased-array and radar breakthroughs. In *Radar Conference, 2007 IEEE*, pages 37–42. IEEE, 2007.

[34] Tapan K Sarkar, Robert Mailloux, Arthur A Oliner, Magdalena Salazar-Palma, and Dipak L Sengupta. *History of wireless*, volume 177. John Wiley & Sons, 2006.

[35] Eli Brookner. Phased arrays and radars-past, present and future. *Microwave Journal*, 49(1):24, 2006.

[36] Mark E Russell, Arthur Crain, Anthony Curran, Richard A Campbell, Clifford A Drubin, and William F Miccioli. Millimeter-wave radar sensor for automotive intelligent cruise control (icc). *IEEE Transactions on microwave theory and techniques*, 45(12):2444–2453, 1997.

[37] Bon-Hyun Ku, Paul Schmalenberg, Ozgur Inac, Ozan Dogan Gurbuz, Jae Seung Lee, Koji Shiozaki, and Gabriel M Rebeiz. A 77–81-ghz 16-element phased-array receiver with beam scanning for advanced automotive radars. *IEEE Transactions on Microwave Theory and Techniques*, 62(11):2823–2832, 2014.

[38] Joerg Schoebel, Thomas Buck, Mathias Reimann, Markus Ulm, Martin Schneider, Anne Jourdain, Geert J Carchon, and Harrie AC Tilmans. Design considerations and technology assessment of phased-array antenna systems with rf mems for automotive radar applications. *IEEE Transactions on Microwave Theory and Techniques*, 53(6):1968–1975, 2005.

[39] Ozgur Inac, Donghyup Shin, and Gabriel M Rebeiz. A phased array rfic with built-in self-test capabilities. *IEEE Transactions on Microwave Theory and Techniques*, 60(1):139–148, 2012.

[40] DS Zrnic, JF Kimpel, DE Forsyth, A Shapiro, G Crain, R Ferek, J Heimmer, W Benner, TJ McNellis, and RJ Vogt. Agile-beam phased array radar for weather observations. *Bulletin of the American Meteorological Society*, 88 (11):1753–1766, 2007.

[41] Guifu Zhang, Robert D Palmer, Dusan S Zmic, and Richard J Doviak. Cylindrical polarimetric phased array radar, March 24 2015. US Patent 8,988,274.

[42] Shaya Karimkashi, Guifu Zhang, Redmond Kelley, John Meier, Robert Palmer, Allen Zahrai, Richard J Doviak, and Dusan S Zrnic. Cylindrical polarimetric phased array radar demonstrator: Design and analysis of a frequency scanning antenna array. In *Phased Array Systems & Technology, 2013 IEEE International Symposium on*, pages 477–480. IEEE, 2013.

[43] Shaya Karimkashi and Guifu Zhang. An optimal design of a cylindrical polarimetric phased array radar for weather sensing. *Radio Science*, 47(2), 2012.

[44] Guifu Zhang, Richard J Doviak, Dusan S Zrnic, Robert Palmer, Lei Lei, and Yasser Al-Rashid. Polarimetric phased-array radar for weather measurement: A planar or cylindrical configuration? *Journal of Atmospheric and Oceanic Technology*, 28(1):63–73, 2011.

[45] J Herd, D Carlson, S Duffy, M Weber, G Brigham, M Rachlin, D Cursio, C Liss, and C Weigand. Multifunction phased array radar (mpar) for aircraft and weather surveillance. In *2010 IEEE Radar Conference*, pages 945–948. IEEE, 2010.

[46] Mark E Weber, John YN Cho, Jeffrey S Herd, James M Flavin, William E Benner, and Garth S Torok. The next-generation multimission us surveillance radar network. *Bulletin of the American Meteorological Society*, 88 (11):1739, 2007.

[47] Gabriel M Rebeiz, Sang-Young Kim, Ozgur Inac, Woorim Shin, Ozan Gurbuz, Yu-Chin Ou, Fatih Golcuk, Tumay Kanar, and Bon-Hyun Ku. Millimeter-wave large-scale phased-arrays for 5g systems. In *2015 IEEE MTT-S International Microwave Symposium*, pages 1–3. IEEE, 2015.

[48] Eli Brookner. Mimo radar demystified. In *Microwave Journal*, January 15, 2013.

[49] Eli Brookner. Mimo radar demystified and where it makes sense to use. In *2014 International Radar Conference*, pages 1–6. IEEE, 2014.

[50] J Herd, S Duffy, M Weber, G Brigham, C Weigand, and D Cursio. Advanced architecture for a low cost multifunction phased array radar. In *Proceedings of 2010 IEEE MTT-S International Symposium*, pages 676–679, 2010.

[51] Mark Weber, John Cho, James Flavin, Jeffrey Herd, and Michael Vai. Multifunction phased array radar for us civil-sector surveillance needs. In *32nd Conf. on Radar Meteorology, Albuquerque, New Mex., 24–29 Oct*, 2005.

[52] WE Benner, G Torok, M Weber, M Emanuel, J Stailey, J Cho, and R Blasewitz. Progress of multifunction phased array radar (mpar) program. In *Preprints, 25th Conf. on Interactive Information and Processing Systems for Meteorology, Oceanography, and Hydrology, Phoenix, AZ, Amer. Meteor. Soc. B*, volume 8, 2009.

[53] Atef Z Elsherbeni and Veysel Demir. The finite-difference time-domain method for electromagnetics with matlab simulations. 2009.

[54] James Clerk Maxwell. *A Treatise on Electricity and Magnetism: By James Clerk Maxwell*. Dover, 1954.

[55] Kane S Yee et al. Numerical solution of initial boundary value problems involving maxwells equations in isotropic media. *IEEE Trans. Antennas Propag*, 14(3):302–307, 1966.

[56] Alexander Hrennikoff. Solution of problems of elasticity by the framework method. *Journal of applied mechanics*, 8(4):169–175, 1941.

[57] D McHenry. A lattice analogy for the solution of plane stress problems. *Journal of Institution of Civil Engineers*, 21:59–82, 1943.

[58] Richard Courant et al. Variational methods for the solution of problems of equilibrium and vibrations. *Bull. Amer. Math. Soc*, 49(1):1–23, 1943.

[59] P Silvester. Finite element solution of homogeneous waveguide problems. *Alta Frequenza*, 38:313–317, 1969.

[60] Jian-Ming Jin. *Theory and computation of electromagnetic fields*. John Wiley & Sons, 2011.

[61] Jian-Ming Jin. *The finite element method in electromagnetics*. John Wiley & Sons, 2014.

[62] K Mei and J Van Bladel. Scattering by perfectly-conducting rectangular cylinders. *IEEE transactions on Antennas and Propagation*, 11(2):185–192, 1963.

[63] M Andreasen. Scattering from parallel metallic cylinders with arbitrary cross sections. *IEEE transactions on Antennas and Propagation*, 12(6):746–754, 1964.

[64] FK Oshiro and CW Su. Source distribution technique for the solution of general electromagnetic scattering problems. In *Proc. First GISAT Symposium*, volume 1, 1965.

[65] Jack Richmond. Scattering by a dielectric cylinder of arbitrary cross section shape. *IEEE Transactions on Antennas and Propagation*, 13(3):334–341, 1965.

[66] Roger F Harrington and Jan L Harrington. *Field computation by moment methods*. Oxford University Press, 1996.

[67] Morris Kline. Electromagnetic theory and geometrical optics. Technical report, DTIC Document, 1962.

[68] Joseph B Keller. Diffraction by an aperture. *Journal of Applied Physics*, 28 (4):426–444, 1957.

[69] Joseph B Keller. Geometrical theory of diffraction. *JOSA*, 52(2):116–130, 1962.

[70] Graeme L James. *Geometrical theory of diffraction for electromagnetic waves*. Number 1. IET, 1986.

[71] Robert G Kouyoumjian and Prabhakar H Pathak. A uniform geometrical theory of diffraction for an edge in a perfectly conducting surface. *Proceedings of the IEEE*, 62(11):1448–1461, 1974.

[72] Prabhaker H Pathak and Robert G Kouyoumjian. An analysis of the radiation from apertures in curved surfaces by the geometrical theory of diffraction. *Proceedings of the IEEE*, 62(11):1438–1447, 1974.

[73] DS Ahluwalia, RM Lewis, and J Boersma. Uniform asymptotic theory of diffraction by a plane screen. *SIAM Journal on applied mathematics*, 16(4): 783–807, 1968.

[74] Shung-Wu Lee and G Deschamps. A uniform asymptotic theory of electromagnetic diffraction by a curved wedge. *IEEE transactions on antennas and propagation*, 24(1):25–34, 1976.

[75] R Mittra, Y Rahmat-Samii, and WL Ko. Spectral theory of diffraction. *Applied physics*, 10(1):1–13, 1976.

[76] Daniel P Bouche, Frederic A Molinet, and RAJ Mittra. Asymptotic and hybrid techniques for electromagnetic scattering. *Proceedings of the IEEE*, 81(12):1658–1684, 1993.

[77] David B Davidson. *Computational electromagnetics for RF and microwave engineering*. Cambridge University Press, 2005.

[78] Björn Thors, Hans Steyskal, and Henrik Holter. Broad-band fragmented aperture phased array element design using genetic algorithms. *IEEE Transactions on Antennas and Propagation*, 53(10):3280–3287, 2005.

[79] James G Maloney, Bradford N Baker, James J Acree, John W Schultz, John A Little, and Daniel D Reuster. Fragmented aperture antenna design of miniaturized gps crpa: model and measurements. In *2007 IEEE Antennas and Propagation Society International Symposium*, 2007.

[80] A Taflove and SC Hagness. Computational electrodynamics artech house. *Inc., MA*, 2000.

[81] Khaled ElMahgoub, Fan Yang, Atef Z Elsherbeni, Veysel Demir, and Ji Chen. Fdtd analysis of periodic structures with arbitrary skewed grid. *IEEE Transactions on Antennas and Propagation*, 58(8):2649–2657, 2010.

[82] Gregory Turner and C Christodoulou. Broadband periodic boundary condition for fdtd analysis of phased array antennas. In *Antennas and Propagation Society International Symposium, 1998. IEEE*, volume 2, pages 1020–1023. IEEE, 1998.

[83] Gregory M Turner and Christos Christodoulou. Fdtd analysis of phased array antennas. *IEEE Transactions on Antennas and Propagation*, 47(4): 661–667, 1999.

[84] Fan Yang, Ji Chen, Rui Qiang, and Atef Elsherbeni. A simple and efficient fdtd/pbc algorithm for scattering analysis of periodic structures. *Radio Science*, 42(4), 2007.

[85] Fan Yang, Atef Elsherbeni, and Ji Chen. A hybrid spectral-fdtd/arma method for periodic structure analysis. In *2007 IEEE Antennas and Propagation Society International Symposium*, pages 3720–3723. IEEE, 2007.

[86] Fan Yang, Ji Chen, Rui Qiang, and Atef Elsherbeni. Fdtd analysis of periodic structures at arbitrary incidence angles: a simple and efficient implementation of the periodic boundary conditions. In *IEEE Antennas and Propagation Society Intl. Symp*, pages 2715–2718, 2006.

[87] N Dib, T Weller, and Max Scardelletti. Analysis of 3-d cylindrical structures using the finite difference time domain method. In *Microwave Symposium Digest, 1998 IEEE MTT-S International*, volume 2, pages 925–928. IEEE, 1998.

[88] Chenghao Yuan and Zhizhang Chen. A three-dimensional unconditionally stable adi-fdtd method in the cylindrical coordinate system. *IEEE transactions on microwave theory and techniques*, 50(10):2401–2405, 2002.

[89] Yiwang Chen, Yawen Liu, Bin Chen, and Pin Zhang. A cylindrical higher-order fdtd algorithm with pml and quasi-pml. *IEEE Transactions on Antennas and Propagation*, 61(9):4695–4704, 2013.

[90] Jiang-Qi He and Qing Huo Liu. A nonuniform cylindrical fdtd algorithm with improved pml and quasi-pml absorbing boundary conditions. *IEEE transactions on geoscience and remote sensing*, 37(2):1066–1072, 1999.

[91] Yawen Liu, Yiwang Chen, Bin Chen, and Xin Xu. A cylindrical mrtd algorithm with pml and quasi-pml. *IEEE Transactions on Microwave Theory and Techniques*, 61(3):1006–1017, 2013.

[92] FL Teixeira and WC Chew. Pml-fdtd in cylindrical and spherical grids. *IEEE microwave and guided wave letters*, 7(9):285–287, 1997.

[93] Palandech Jin-fa Lee, R, and R Mittra. Modeling three-dimensional discontinuities in waveguides using nonorthogonal fdtd algorithm. *IEEE Transactions on Microwave Theory and Techniques*, 40(2):346–352, 1992.

[94] Clive Parini, Stuart Gregson, John McCormick, and Daniël Janse Van Rensburg. *Theory and Practice of Modern Antenna Range Measurements*. Institution of Engineering and Technology, 2014.

[95] Gregory F Masters and Stuart F Gregson. Coordinate system plotting for antenna measurements. In *AMTA Annual Meeting & Symposium*, 2007.

[96] Stuart Gregson, John McCormick, and Clive Parini. *Principles of planar near-field antenna measurements*, volume 53. IET, 2007.

[97] John Parr Snyder. *Map projections–A working manual*, volume 1395. US Government Printing Office, 1987.

[98] IEEE. 145-2013 - ieee standard for definitions of terms for antennas, 2013.

[99] Arthur Ludwig. The definition of cross polarization. *Antennas and Propagation, IEEE Transactions on*, 21(1):116–119, 1973.

[100] JE Roy and L Shafai. Generalization of the ludwig-3 definition for linear copolarization and cross polarization. *IEEE Transactions on Antennas and Propagation*, 49(6):1006–1010, 2001.

[101] David M Pozar. The active element pattern. *IEEE Transactions on Antennas and Propagation*, 42(8):1176–1178, 1994.

[102] David M Pozar. A relation between the active input impedance and the active element pattern of a phased array. *IEEE Transactions on Antennas and Propagation*, 51(9):2486–2489, 2003.

[103] Robert C Hansen. *Phased array antennas*, volume 213. John Wiley & Sons, 2009.

[104] RC Hansen. Evaluation of the large array method. In *IEE Proceedings H: Microwaves Antennas and Propagation*, volume 137, pages 94–98, 1990.

[105] Sudantha Perera, Yu Pan, Yan Zhang, Xining Yu, Dusan Zrnic, and Richard Doviak. A fully reconfigurable polarimetric phased array antenna testbed. *International Journal of Antennas and Propagation*, 2014, 2014.

[106] Sudantha Perera, Yu Pan, Qing Zhao, Yan Rockee Zhang, Dusan Zmic, and Richard J Doviak. A fully reconfigurable polarimetric phased array testbed: Antenna integration and initial measurements. In *Phased Array Systems & Technology, 2013 IEEE International Symposium on*, pages 799–806. IEEE, 2013.

[107] Yan Zhang, Yu Pan, Shang Wang, Qing Zhao, Dusan Zrnic, and Richard J Doviak. Reconfigurable and scalable array element design for polarimetric multifunctional par. In *Proceedings of the 2011 IEEE Radar Conference (RADAR)*, pages 175–179. IEEE, 2011.

[108] Y. Rahmat-Samii J. Robinson. Particle swarm optimization in electromagnetics. *IEEE Transactions on Antennas and Propagation*, 52(2):397–407, 2004.

[109] K Woelder and Johan Granholm. Cross-polarization and sidelobe suppression in dual linear polarization antenna arrays. *IEEE Transactions on Antennas and Propagation*, 45(12):1727–1740, 1997.

[110] Y Rahmat-Samil, Keerti S Kona, Majid Manteghi, Simon Yueh, William J Wilson, Steve Dinardo, and Don Hunter. A novel lightweight dual-frequency dual-polarized sixteen-element stacked patch microstrip array antenna for soil-moisture and sea-surface-salinity missions. *IEEE Antennas and Propagation Magazine*, 48(6):33–46, 2006.

[111] Robert S Elliot. *Antenna theory and design*. John Wiley & Sons, 2006.

[112] AA Oliner and RG Malech. Mutual coupling in infinite scanning arrays. *Microwave scanning antennas*, 2:195–335, 1966.

[113] G Farrell and D Kuhn. Mutual coupling in infinite planar arrays of rectangular waveguide horns. *IEEE Transactions on Antennas and Propagation*, 16(4):405–414, 1968.

[114] George H Knittel, Alexander Hessel, and Arthur A Oliner. Element pattern nulls in phased arrays and their relation to guided waves. *Proceedings of the IEEE*, 56(11):1822–1836, 1968.

[115] A Roederer. Etude des réseaux finis de guides rectangulaires à parois épaisses. *Londe Électrique*, 51:854–861, 1971.

[116] A Ishimaru, R Coe, G Miller, and W Geren. Finite periodic structure approach to large scanning array problems. *IEEE transactions on antennas and propagation*, 33(11):1213–1220, 1985.

[117] Anja K Skrivervik and Juan R Mosig. Analysis of finite phase arrays of microstrip patches. *IEEE transactions on antennas and propagation*, 41(8): 1105–1114, 1993.

[118] Andrew J Roscoe and Roger A Perrott. Large finite array analysis using infinite array data. *IEEE transactions on antennas and propagation*, 42(7): 983–992, 1994.

[119] Ben A Munk. *Finite antenna arrays and FSS*. John Wiley & Sons, 2003.

[120] RC Hansen. Finite array scan impedance gibbsian models. *Radio Science*, 31(6):1631–1637, 1996.

[121] Boris Tomasic and Alexander Hessel. Analysis of finite arrays-a new approach. *IEEE Transactions on Antennas and Propagation*, 47(3):555–565, 1999.

[122] Arun K Bhattacharyya. *Phased array antennas: Floquet analysis, synthesis, BFNs and active array systems*, volume 179. John Wiley & Sons, 2006.

[123] Arun K Bhattacharyya. An accurate model for finite array patterns based on floquet modal theory. *IEEE Transactions on Antennas and Propagation*, 63(3):1040–1047, 2015.

[124] Rick W Kindt, Kubilay Sertel, Erdem Topsakal, and John L Volakis. Array decomposition method for the accurate analysis of finite arrays. *IEEE Transactions on Antennas and Propagation*, 51(6):1364–1372, 2003.

[125] Rick W Kindt and John L Volakis. Array decomposition-fast multipole method for finite array analysis. *Radio Science*, 39(2), 2004.

[126] Ronald Coifman, Vladimir Rokhlin, and Stephen Wandzura. The fast multipole method for the wave equation: A pedestrian prescription. *IEEE Antennas and Propagation Magazine*, 35(3):7–12, 1993.

[127] AK Bhattacharyya. Floquet-modal-based analysis for mutual coupling between elements in an array environment. *IEE Proceedings-Microwaves, Antennas and Propagation*, 144(6):491–497, 1997.

[128] Warren L Stutzman and Gary A Thiele. *Antenna theory and design*. John Wiley & Sons, 2012.

[129] Constantine A Balanis. *Advanced engineering electromagnetics*. John Wiley & Sons, 2012.

[130] Constantine A Balanis. *Antenna theory: analysis and design*. John Wiley & Sons, 2016.

[131] SA Schelkunoff. Some equivalence theorems of electromagnetics and their application to radiation problems. *Bell System Technical Journal*, 15(1): 92–112, 1936.

[132] Christiaan Huygens. *Traité de la lumière: où sont expliquées les causes de ce qui luy arrive dans la reflexion, & dans la refraction, et particulierement dans l'etrange refraction du cistal d'Islande*. Chez Pierre vander Aa, 1885.

[133] Raymond J Luebbers, Karl S Kunz, Michael Schneider, and Forrest Hunsberger. A finite-difference time-domain near zone to far zone transformation [electromagnetic scattering]. *IEEE Transactions on Antennas and Propagation*, 39(4):429–433, 1991.

[134] Raymond Luebbers, Deirdre Ryan, and John Beggs. A two-dimensional time-domain near-zone to far-zone transformation. *IEEE transactions on antennas and propagation*, 40(7):848–851, 1992.

[135] Dave Hale. The java and cpp platforms for scientific computing.

[136] George Em Karniadakis and Robert M Kirby II. *Parallel scientific computing in C++ and MPI: a seamless approach to parallel algorithms and their implementation*. Cambridge University Press, 2003.

[137] Bjorn Gustavsen and Adam Semlyen. Rational approximation of frequency domain responses by vector fitting. *IEEE Transactions on power delivery*, 14(3):1052–1061, 1999.

[138] Dirk Deschrijver, Davy Pissoort, and Tom Dhaene. Adaptive stopping criterion for fast time domain characterization of microwave components. *IEEE Microwave and Wireless Components Letters*, 19(12):765–767, 2009.

Appendix A

FDTD Updating Equations for an-isotropic media in Rectangular Coordinate System

All the FDTD equation in rectangular coordinate system are in the same format as them in cylindrical coordinate system. The electric (magnetic) field component on the left hand side is the future value to be predicted from the past value of electric (magnetic) field component, past electric (magnetic) current density component, and past magnetic (electric) field components which are perpendicular to electric (magnetic) field and surrounded by electric (magnetic) field.
$E_x^{n+1}(i_x, i_y, i_z)$ can be computed using equation A.1.

$$\begin{aligned} E_x^{n+1}(i_x, i_y, i_z) &= C_{exe}(i_x, i_y, i_z) \times E_x^n(i_x, i_y, i_z) \\ &+ C_{exhz}(i_x, i_y, i_z) \times \left(H_z^{n+\frac{1}{2}}(i_x, i_y, i_z) - H_z^{n+\frac{1}{2}}(i_x, i_y - 1, i_z) \right) \\ &+ C_{exhy}(i_x, i_y, i_z) \times \left(H_y^{n+\frac{1}{2}}(i_x, i_y, i_z) - H_y^{n+\frac{1}{2}}(i_x, i_y, i_z - 1) \right) \\ &+ C_{exj}(i_x, i_y, i_z) \times J_x^{n+\frac{1}{2}}(i_x, i_y, i_z) \end{aligned} \tag{A.1}$$

The updating coefficients $C_{exe}(i_x, i_y, i_z)$, $C_{exhz}(i_x, i_y, i_z)$, $C_{exhy}(i_x, i_y, i_z)$, and $C_{exj}(i_x, i_y, i_z)$ of the equation (A.1) can be computed as in equations (A.2a),

(A.2b), (A.2c), and (A.2d).

$$C_{exe}(i_x, i_y, i_z) = \left(\frac{2\epsilon_x(i_x, i_y, i_z) - \sigma^e{}_x(i_x, i_y, i_z)\Delta_t}{2\epsilon_x(i_x, i_y, i_z) + \sigma^e{}_x(i_x, i_y, i_z)\Delta_t} \right) \tag{A.2a}$$

$$C_{exhz}(i_x, i_y, i_z) = \left(\frac{2\Delta_t}{\Delta_y \left(2\epsilon_x(i_x, i_y, i_z) + \sigma^e{}_x(i_x, i_y, i_z)\Delta_t\right)} \right) \tag{A.2b}$$

$$C_{exhy}(i_x, i_y, i_z) = \left(\frac{-2\Delta_t}{\Delta_z \left(2\epsilon_x(i_x, i_y, i_z) + \sigma^e{}_x(i_x, i_y, i_z)\Delta_t\right)} \right) \tag{A.2c}$$

$$C_{exj}(i_x, i_y, i_z) = \left(\frac{-2\Delta_t}{2\epsilon_x(i_x, i_y, i_z) + \sigma^e{}_x(i_x, i_y, i_z)\Delta_t} \right) \tag{A.2d}$$

$E_y^{n+1}(i_x, i_y, i_z)$ can be computed using equation A.3.

$$\begin{aligned} E_y^{n+1}(i_x, i_y, i_z) &= C_{eye}(i_x, i_y, i_z) \times E_y^n(i_x, i_y, i_z) \\ &+ C_{eyhx}(i_x, i_y, i_z) \times \left(H_x^{n+\frac{1}{2}}(i_x, i_y, i_z) - H_x^{n+\frac{1}{2}}(i_x, i_y, i_z - 1) \right) \\ &- C_{eyhz}(i_x, i_y, i_z) \times \left(H_z^{n+\frac{1}{2}}(i_x, i_y, i_z) - H_z^{n+\frac{1}{2}}(i_x - 1, i_y, i_z) \right) \\ &+ C_{eyj}(i_x, i_y, i_z) \times J_y^{n+\frac{1}{2}}(i_x, i_y, i_z) \end{aligned} \tag{A.3}$$

The updating coefficients $C_{eye}(i_x, i_y, i_z)$, $C_{eyhx}(i_x, i_y, i_z)$, and $C_{eyhz}(i_x, i_y, i_z)$ of the equation (A.3) can be computed as in equations (A.4a), (A.4b), (A.4c), and (A.4d).

$$C_{eye}(i_x, i_y, i_z) = \left(\frac{2\epsilon_y(i_x, i_y, i_z) - \sigma^e{}_y(i_x, i_y, i_z)\Delta_t}{2\epsilon_y(i_x, i_y, i_z) + \sigma^e{}_y(i_x, i_y, i_z)\Delta_t} \right) \tag{A.4a}$$

$$C_{eyhx}(i_x, i_y, i_z) = \left(\frac{2\Delta_t}{\Delta_z \left(2\epsilon_y(i_x, i_y, i_z) + \sigma^e{}_y(i_x, i_y, i_z)\Delta_t\right)} \right) \tag{A.4b}$$

$$C_{eyhz}(i_x, i_y, i_z) = \left(\frac{-2\Delta_t}{\Delta_x \left(2\epsilon_y(i_x, i_y, i_z) + \sigma^e{}_y(i_x, i_y, i_z)\Delta_t\right)} \right) \tag{A.4c}$$

$$C_{eyj}(i_x, i_y, i_z) = \left(\frac{-2\Delta_t}{2\epsilon_y(i_x, i_y, i_z) + \sigma^e{}_y(i_x, i_y, i_z)\Delta_t} \right) \tag{A.4d}$$

$E_z^{n+1}(i_x, i_y, i_z)$ can be computed using equation A.5.

$$\begin{aligned} E_z^{n+1}(i_x, i_y, i_z) &= C_{eze}(i_x, i_y, i_z) \times E_z^n(i_x, i_y, i_z) \\ &+ C_{ezhy}(i_x, i_y, i_z) \times \left(H_y^{n+\frac{1}{2}}(i_x, i_y, i_z) - H_y^{n+\frac{1}{2}}(i_x - 1, i_y, i_z) \right) \\ &- C_{ezhx}(i_x, i_y, i_z) \times \left(H_x^{n+\frac{1}{2}}(i_x, i_y, i_z) - H_x^{n+\frac{1}{2}}(i_x, i_y - 1, i_z) \right) \\ &+ C_{ezj}(i_x, i_y, i_z) \times J_z^{n+\frac{1}{2}}(i_x, i_y, i_z) \end{aligned} \tag{A.5}$$

The updating coefficients $C_{eze}(i_x, i_y, i_z)$, $C_{ezhy}(i_x, i_y, i_z)$, $C_{ezhx}(i_x, i_y, i_z)$, and $C_{ezj}(i_x, i_y, i_z)$ of the equation (A.5) can be computed as in equations (A.6a), (A.6b), (A.6c), and (A.6d).

$$C_{eze}(i_x, i_y, i_z) = \left(\frac{2\epsilon_z(i_x, i_y, i_z) - \sigma^e{}_z(i_x, i_y, i_z)\Delta_t}{2\epsilon_z(i_x, i_y, i_z) + \sigma^e{}_z(i_x, i_y, i_z)\Delta_t} \right) \tag{A.6a}$$

$$C_{ezhy}(i_x, i_y, i_z) = \left(\frac{2\Delta_t}{\Delta_z \left(2\epsilon_z(i_x, i_y, i_z) + \sigma^e{}_z(i_x, i_y, i_z)\Delta_t\right)} \right) \tag{A.6b}$$

$$C_{ezhx}(i_x, i_y, i_z) = \left(\frac{-2\Delta_t}{\Delta_y \left(2\epsilon_z(i_x, i_y, i_z) + \sigma^e{}_z(i_x, i_y, i_z)\Delta_t\right)} \right) \tag{A.6c}$$

$$C_{ezj}(i_x, i_y, i_z) = \left(\frac{-2\Delta_t}{2\epsilon_z(i_x, i_y, i_z) + \sigma^e{}_z(i_x, i_y, i_z)\Delta_t} \right) \tag{A.6d}$$

$H_x^{n+\frac{1}{2}}(i_x, i_y, i_z)$ can be computed using equation A.7.

$$\begin{aligned} H_x^{n+\frac{1}{2}}(i_x, i_y, i_z) &= C_{hxh}(i_x, i_y, i_z) \times H_x^{n-\frac{1}{2}}(i_x, i_y, i_z) \\ &+ C_{hxez}(i_x, i_y, i_z) \times (E_z^n(i_x, i_y + 1, i_z) - E_z^n(i_x, i_y, i_z)) \\ &+ C_{hxey}(i_x, i_y, i_z) \times \left(E_y^n(i_x, i_y, i_z + 1) - E_y^n(i_x, i_y, i_z)\right) \\ &+ C_{hxm}(i_x, i_y, i_z) \times M_x^n(i_x, i_y, i_z) \end{aligned} \tag{A.7}$$

The updating coefficients $C_{eye}(i_x, i_y, i_z)$, $C_{eyhx}(i_x, i_y, i_z)$, $C_{eyhz}(i_x, i_y, i_z)$ and $C_{hxm}(i_x, i_y, i_z)$ of the equation (A.7) can be computed as in equations (A.8a),

(A.8b), (A.8c), and (A.8d).

$$C_{hxh}(i_x, i_y, i_z) = \left(\frac{2\mu_x(i_x, i_y, i_z) - \sigma^m{}_x(i_x, i_y, i_z)\Delta_t}{2\mu_x(i_x, i_y, i_z) + \sigma^m{}_x(i_x, i_y, i_z)\Delta_t} \right) \tag{A.8a}$$

$$C_{hxez}(i_x, i_y, i_z) = \left(\frac{-2\Delta_t}{\Delta_y \left(2\mu_x(i_x, i_y, i_z) + \sigma^m{}_x(i_x, i_y, i_z)\Delta_t\right)} \right) \tag{A.8b}$$

$$C_{hxey}(i_x, i_y, i_z) = \left(\frac{2\Delta_t}{\Delta_z \left(2\mu_x(i_x, i_y, i_z) + \sigma^m{}_x(i_x, i_y, i_z)\Delta_t\right)} \right) \tag{A.8c}$$

$$C_{hxm}(i_x, i_y, i_z) = \left(\frac{-2\Delta_t}{2\mu_x(i_x, i_y, i_z) + \sigma^m{}_x(i_x, i_y, i_z)\Delta_t} \right) \tag{A.8d}$$

$H_y^{n+\frac{1}{2}}(i_x, i_y, i_z)$ can be computed using equation A.9.

$$\begin{aligned} H_y^{n+\frac{1}{2}}(i_x, i_y, i_z) &= C_{hyh}(i_x, i_y, i_z) \times H_y^{n-\frac{1}{2}}(i_x, i_y, i_z) \\ &+ C_{hyez}(i_x, i_y, i_z) \times (E_z^n(i_x + 1, i_y, i_z) - E_z^n(i_x, i_y, i_z)) \\ &+ C_{hyex}(i_x, i_y, i_z) \times (E_x^n(i_x, i_y, i_z + 1) - E_x^n(i_x, i_y, i_z)) \\ &+ C_{hym}(i_x, i_y, i_z) \times M_y^n(i_x, i_y, i_z) \end{aligned} \tag{A.9}$$

The updating coefficients $C_{eye}(i_x, i_y, i_z)$, $C_{eyhx}(i_x, i_y, i_z)$, $C_{eyhz}(i_x, i_y, i_z)$, and $C_{hym}(i_x, i_y, i_z)$ of the equation (A.9) can be computed as in equations (3.28a), (3.28b), (A.10c), and (3.28d).

$$C_{hyh}(i_x, i_y, i_z) = \left(\frac{2\mu_y(i_x, i_y, i_z) - \sigma^m{}_y(i_x, i_y, i_z)\Delta_t}{2\mu_y(i_x, i_y, i_z) + \sigma^m{}_y(i_x, i_y, i_z)\Delta_t} \right) \tag{A.10a}$$

$$C_{hyez}(i_x, i_y, i_z) = \left(\frac{2\Delta_t}{\Delta_x \left(2\mu_y(i_x, i_y, i_z) + \sigma^m{}_y(i_x, i_y, i_z)\Delta_t\right)} \right) \tag{A.10b}$$

$$C_{hyex}(i_x, i_y, i_z) = \left(\frac{-2\Delta_t}{\Delta_z \left(2\mu_y(i_x, i_y, i_z) + \sigma^m{}_y(i_x, i_y, i_z)\Delta_t\right)} \right) \tag{A.10c}$$

$$C_{hym}(i_x, i_y, i_z) = \left(\frac{-2\Delta_t}{2\mu_y(i_x, i_y, i_z) + \sigma^m{}_y(i_x, i_y, i_z)\Delta_t} \right) \tag{A.10d}$$

$H_z^{n+\frac{1}{2}}(i_x, i_y, i_z)$ can be computed using equation A.11.

$$\begin{aligned} H_z^{n+\frac{1}{2}}(i_x, i_y, i_z) &= C_{hzh}(i_x, i_y, i_z) \times H_z^{n-\frac{1}{2}}(i_x, i_y, i_z) \\ &+ C_{hzex}(i_x, i_y, i_z) \times (E_x^n(i_x, i_y + 1, i_z) - E_x^n(i_x, i_y, i_z)) \\ &+ C_{hzey}(i_x, i_y, i_z) \times \left(E_y^n(i_x + 1, i_y, i_z) - E_y^n(i_x, i_y, i_z)\right) \\ &+ C_{hzm}(i_x, i_y, i_z) \times M_z^n(i_x, i_y, i_z) \end{aligned} \tag{A.11}$$

The updating coefficients $C_{hzh}(i_x, i_y, i_z)$, $C_{hzex}(i_x, i_y, i_z)$, $C_{hzey}(i_x, i_y, i_z)$, and $C_{hzm}(i_x, i_y, i_z)$ of the equation (A.11) can be computed as in equations (A.12a), (A.12b), (A.12c), and (A.12d).

$$C_{hzh}(i_x, i_y, i_z) = \left(\frac{2\mu_z(i_x, i_y, i_z) - \sigma^m{}_z(i_x, i_y, i_z)\Delta_t}{2\mu_z(i_x, i_y, i_z) + \sigma^m{}_z(i_x, i_y, i_z)\Delta_t}\right) \tag{A.12a}$$

$$C_{hzex}(i_x, i_y, i_z) = \left(\frac{2\Delta_t}{\Delta_y\left(2\mu_z(i_x, i_y, i_z) + \sigma^m{}_z(i_x, i_y, i_z)\Delta_t\right)}\right) \tag{A.12b}$$

$$C_{hzey}(i_x, i_y, i_z) = \left(\frac{-2\Delta_t}{\Delta_x\left(2\mu_z(i_x, i_y, i_z) + \sigma^m{}_z(i_x, i_y, i_z)\Delta_t\right)}\right) \tag{A.12c}$$

$$C_{hzm}(i_x, i_y, i_z) = \left(\frac{-2\Delta_t}{2\mu_z(i_x, i_y, i_z) + \sigma^m{}_z(i_x, i_y, i_z)\Delta_t}\right) \tag{A.12d}$$

Appendix B

Mathematical Equations

B.1 Vector Calculus

The curl of a vector in cylindrical coordinate system:

$$\begin{aligned}\nabla \times \vec{A} &= \begin{vmatrix} \hat{r}\frac{1}{r} & \hat{\phi} & \hat{z}\frac{1}{r} \\ \frac{\partial}{\partial r} & \frac{\partial}{\partial \phi} & \frac{\partial}{\partial z} \\ A_r & rA_\phi & A_z \end{vmatrix} \\ &= \left(\frac{1}{r}\frac{\partial A_z}{\partial \phi} - \frac{\partial A_\phi}{\partial z}\right)\hat{r} + \left(\frac{\partial A_r}{\partial z} - \frac{\partial A_z}{\partial r}\right)\hat{\phi} + \frac{1}{r}\left(\frac{\partial r A_\phi}{\partial r} - \frac{\partial A_r}{\partial \phi}\right)\hat{z}\end{aligned} \tag{B.1}$$

B.2 The Finite Difference Equations

first order accurate finite difference equations are used to discretized electric and magnetic field derivations with respect to space and time.

B.2.1 The finite differences equations for the time and space derivation of electric field components

Equations B.2, B.3, B.4 and B.5 are the finite difference equations for evaluating the approximation to partial differentiations of $E_r^n(r, \phi, z)$ with respect to the

spatial and temporal variables. Similar equation can be given for partial differentiations of $E_{\phi}^{n}(r,\phi,z)$ and $E_{z}^{n}(r,\phi,z)$ with respect to the spatial and temporal variables. *Forward difference* formulas are used for derivations of electric field components.

$$\frac{\partial E_{r}^{n}(r,\phi,z)}{\partial r} = \frac{E_{r}^{n}(r+\Delta_{r},\phi,z) - E_{r}^{n}(r,\phi,z)}{\Delta_{r}} \tag{B.2}$$

$$\frac{\partial E_{r}^{n}(r,\phi,z)}{\partial \phi} = \frac{E_{r}^{n}(r,\phi+\Delta_{\phi},z) - E_{r}^{n}(r,\phi,z)}{\Delta_{\phi}} \tag{B.3}$$

$$\frac{\partial E_{r}^{n}(r,\phi,z)}{\partial z} = \frac{E_{r}^{n}(r,\phi,z+\Delta_{z}) - E_{r}^{n}(r,\phi,z)}{\Delta_{z}} \tag{B.4}$$

$$\frac{\partial E_{r}^{n}(r,\phi,z)}{\partial t} = \frac{E_{\phi}^{n+1}(r,\phi,z) - E_{\phi}^{n}(r,\phi,z)}{\Delta_{t}} \tag{B.5}$$

B.2.2 The finite differences equations for the time and space derivation of magnetic field components

Equations B.6, B.7, B.8 and B.9 are the finite difference equations for for evaluating the approximation to partial differentiations of $H_{r}^{n+\frac{1}{2}}(r,\phi,z)$ with respect to the spatial and temporal variables. Similar equation can be derived for partial differentiations of $H_{\phi}^{n+\frac{1}{2}}(r,\phi,z)$ and $H_{z}^{n+\frac{1}{2}}(r,\phi,z)$ with respect to the spatial and temporal variables. *Backward difference* formulas are used for the space derivations of magnetic field components and *central difference* formulas are used for the time derivations of magnetic field components.

$$\frac{\partial H_{r}^{n+\frac{1}{2}}(r,\phi,z)}{\partial r} = \frac{H_{r}^{n+\frac{1}{2}}(r,\phi,z) - H_{r}^{n+\frac{1}{2}}(r-\Delta_{r},\phi,z)}{\Delta_{r}} \tag{B.6}$$

$$\frac{\partial H_{r}^{n+\frac{1}{2}}(r,\phi,z)}{\partial \phi} = \frac{H_{r}^{n+\frac{1}{2}}(r,\phi,z) - H_{r}^{n+\frac{1}{2}}(r,\phi-\Delta_{\phi},z)}{\Delta_{\phi}} \tag{B.7}$$

$$\frac{\partial H_r^{n+\frac{1}{2}}(r,\phi,z)}{\partial z} = \frac{H_r^{n+\frac{1}{2}}(r,\phi,z) - H_r^{n+\frac{1}{2}}(r,\phi,z-\Delta_z)}{\Delta_z} \tag{B.8}$$

$$\frac{\partial H_r^{n+\frac{1}{2}}(r,\phi,z)}{\partial t} = \frac{H_r^{n+\frac{1}{2}}(r,\phi,z) - H_r^{n-\frac{1}{2}}(r,\phi,z)}{\Delta_t} \tag{B.9}$$

B.2.3 Average of the field components

This averaging equation is useful to express the field components at the time $n+\frac{1}{2}$ in field components at the time n and $n+1$.

$$E_\phi^{n+\frac{1}{2}}(r,\phi,z) = \frac{E_\phi^{n+1}(r,\phi,z) + E_\phi^{n}(r,\phi,z)}{2} \tag{B.10}$$

Appendix C

Supplementary Plots

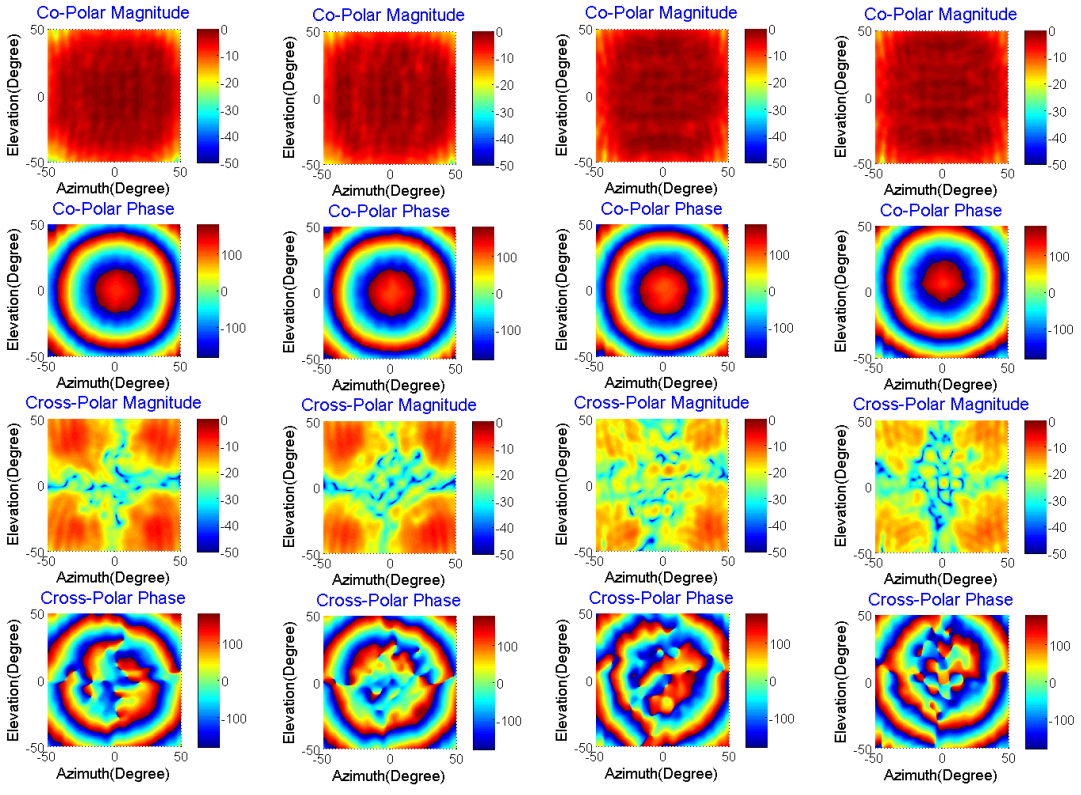

(a) Element at (4,1) (b) Element at (4,2) (c) Element at (4,3) (d) Element at (4,4)

FIGURE C.1: Measured AEP of (5,1) and (5,5) element in the 8×8 Cylindrical Phased array antenna - co-polar (top) and cross-polar (bottom).

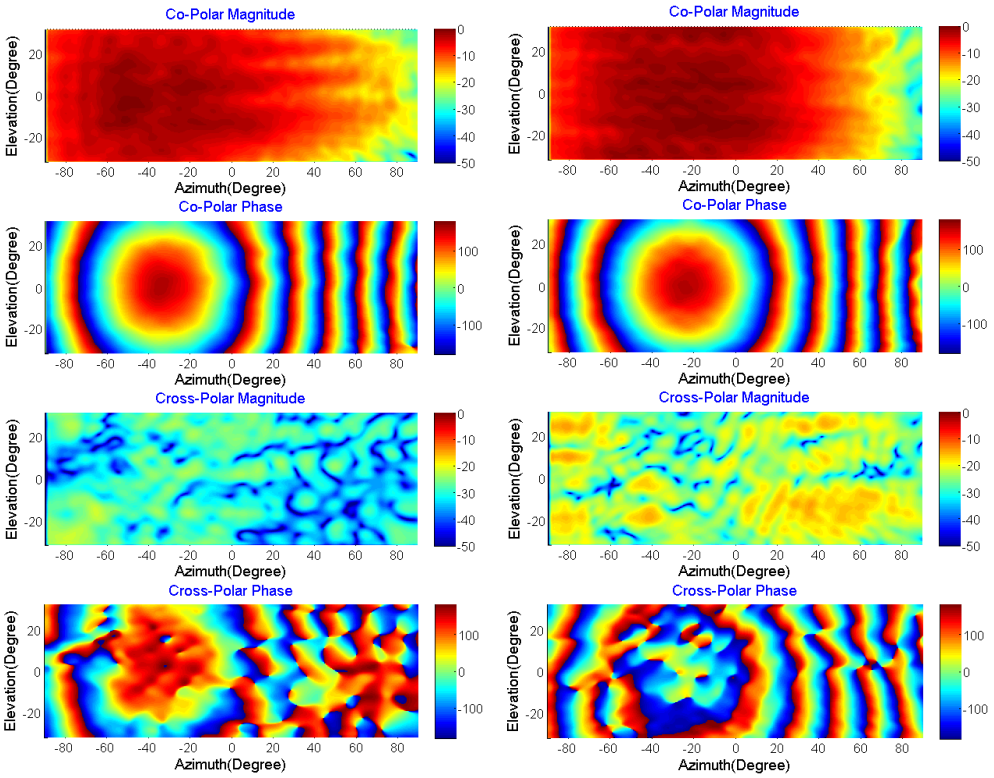

(a) Element at (4,1)

(b) Element at (4,2)

(c) Element at (4,3)

(d) Element at (4,5)

FIGURE C.2: Measured AEP of (5,1) and (5,5) element in the 8×8 Cylindrical Phased array antenna - co-polar (top) and cross-polar (bottom).

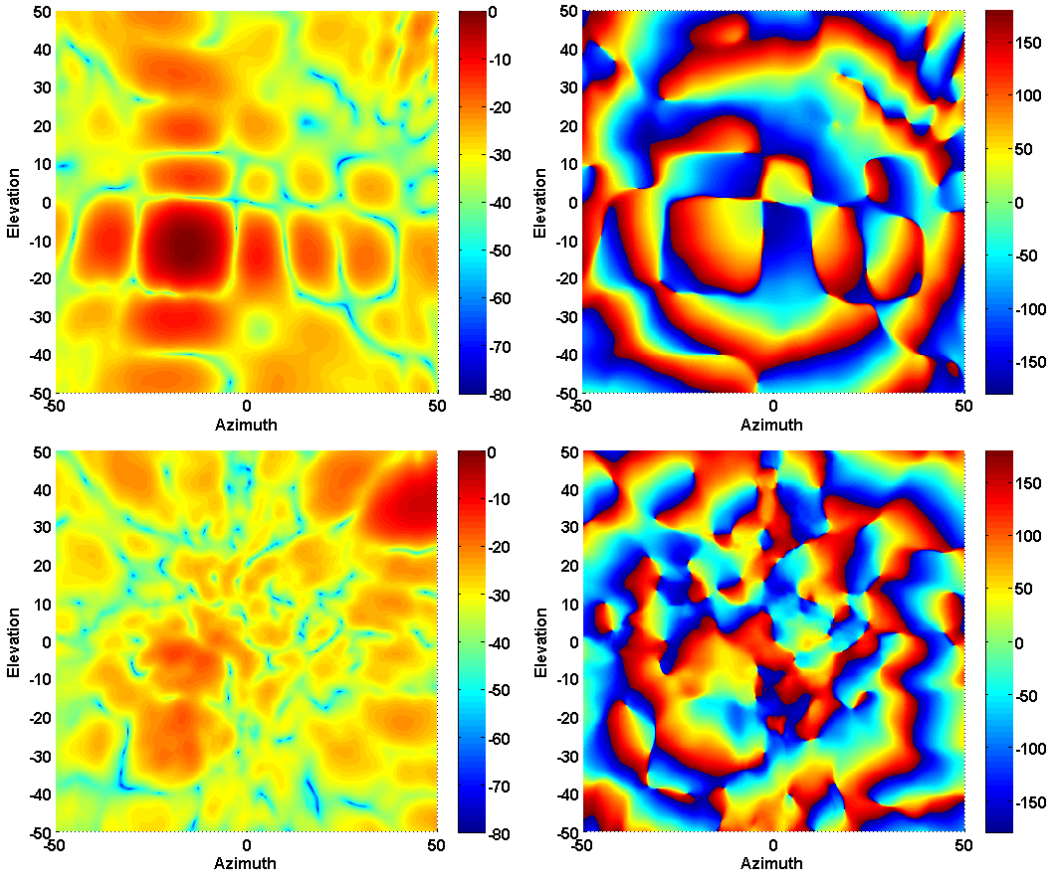

FIGURE C.3: CPAD-II Planar Antenna Measurement - Radiation Patterns With $\theta = 20^\circ$ and $\phi = 40^\circ$ Beam Steering

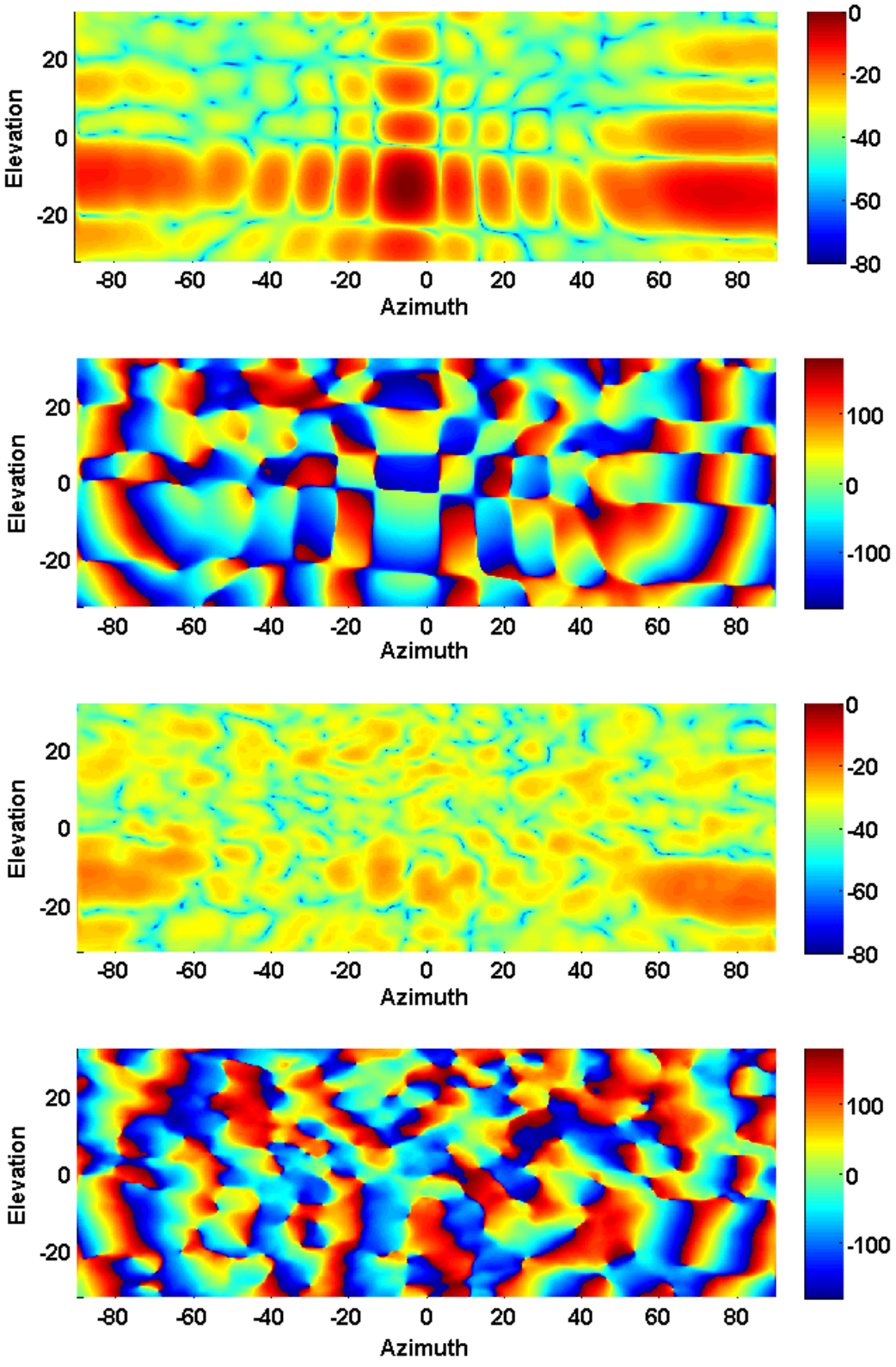

FIGURE C.4: CPAD-II Cylindrical Antenna Measurement - Radiation Patterns With $\theta = 20°$ and $\phi = 40°$ Beam Steering

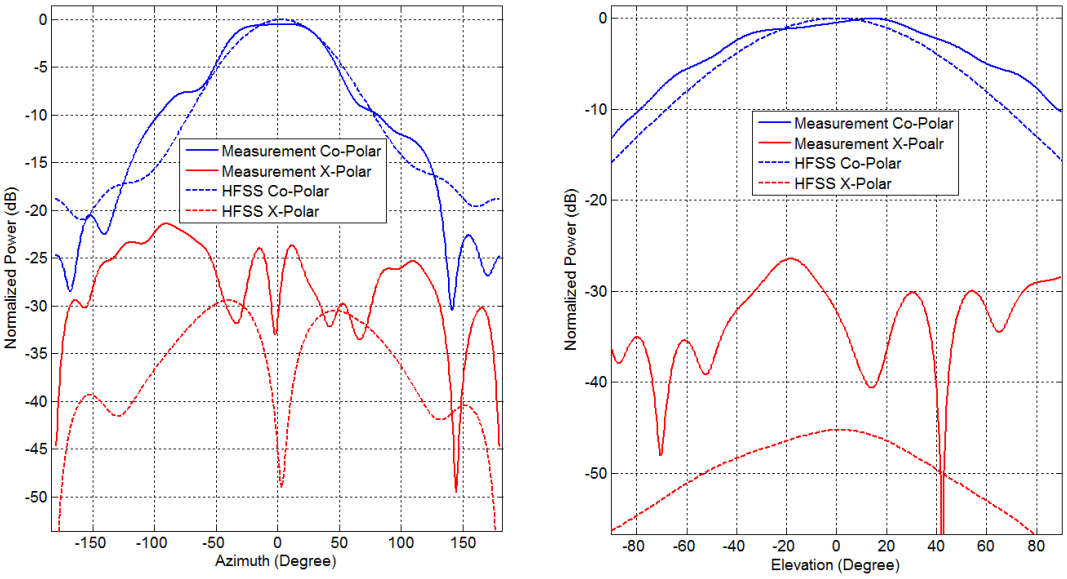

(a) Azimuth Principal Cut

(b) Elevation Principal Cut

FIGURE C.5: Azimuth and Elevation Principal Cut of the patch antenna with slots (HFSS simulation data and Measurements)